TOWARD REGIONAL CHARACTERIZATIONS OF THE OCEANIC INTERNAL WAVEFIELD

K. L. Polzin[1] and Y. V. Lvov[2]

Received 31 January 2010; revised 5 May 2011; accepted 2 June 2011; published 10 November 2011.

[1] Many major oceanographic internal wave observational programs of the last 4 decades are reanalyzed in order to characterize variability of the deep ocean internal wavefield. The observations are discussed in the context of the universal spectral model proposed by C. J. R. Garrett and W. H. Munk. The Garrett and Munk model is a good description of wintertime conditions at Site D on the continental rise north of the Gulf Stream. Elsewhere and at other times, significant deviations in terms of amplitude, separability of the 2-D vertical wavenumber-frequency spectrum, and departure from the model's functional form are reported. Specifically, the Garrett and Munk model overestimates annual average frequency domain spectral levels both at Site D and in general. The bias at Site D is associated with the Garrett and Munk model being a fit to wintertime data from Site D and the presence of an annual cycle in high-frequency energy in the western subtropical North Atlantic having a maximum in winter. The wave spectrum is generally nonseparable, with near-inertial waves typically having greater bandwidth (occupying smaller vertical scales) than continuum frequency waves. Separability is a better approximation for more energetic states, such as wintertime conditions at Site D. Subtle geographic differences from the high-frequency and high vertical wavenumber power laws of the Garrett and Munk spectrum are apparent. Such deviations tend to covary: whiter frequency spectra are partnered with redder vertical wavenumber spectra. We review a general theoretical framework of statistical radiative balance equations and interpret the observed variability in terms of the interplay between generation, propagation, and nonlinearity. First, nonlinearity is a fundamental organizing principle in this work. The observed power laws lie close to the induced diffusion stationary states of the resonant kinetic equation describing the lowest-order nonlinear transfers. Second, eddy variability and by implication wave mean interactions are also an organizing principle. Observations from regions of low eddy variability tend to be outliers in terms of their parametric spectral representation; other data tend to cluster in two regions of parameter space. More tentatively, the seasonal cycle of high-frequency energy is in phase with the near-inertial seasonal cycle in regions of significant eddy variability. In regions of low eddy variability, the seasonal cycle in high-frequency energy lags that of near-inertial energy. The induced diffusion stationary states are approximate analytic solutions to the resonant kinetic equation, and the Garrett and Munk spectrum represents one such analytic solution. We present numerical solutions of the resonant kinetic equation, however, that are inconsistent with the Garrett and Munk model representing a stationary state, either alone or in combination with other physical mechanisms. We believe this to be the case for other regional characterizations as well. We argue that nonstationarity of the numerical solutions is related to local transfers in horizontal wavenumber, whereas the analytic induced diffusion stationary states consider only nonlocal transfers in vertical wavenumber. Consequences for understanding the pathways by which energy is transferred from sources to sinks are considered. Further progress likely requires self-consistent solutions to a broadened kinetic equation.

Citation: Polzin, K. L., and Y. V. Lvov (2011), Toward regional characterizations of the oceanic internal wavefield, *Rev. Geophys.*, *49*, RG4003, doi:10.1029/2010RG000329.

1. INTRODUCTION

[2] Internal waves are ubiquitous features of geophysical fluids, contain a significant fraction of the total variance, and constitute an effective mechanism for transferring energy and momentum across large distances and across different scales. In particular, the drag associated with internal wave breaking needs to be included in order to obtain accurate simulations of the atmospheric jet stream [*Fritts and Alexander*, 2003], and it has been argued that the ocean's Meridional Overturning Circulation [*Wunsch and Ferrari*, 2004] is forced by the diffusion of mass [*Ledwell et al.*, 2000] associated with internal wave breaking [*Polzin et al.*, 1997] rather than by the convective production of cold,

[1]Department of Physical Oceanography, Woods Hole Oceanographic Institution, Woods Hole, Massachusetts, USA.
[2]Department of Mathematical Sciences, Rensselaer Polytechnic Institute, Troy, New York, USA.

8755-1209/11/2010RG000329
Paper number 2010RG000329

dense water at high latitudes. Both circulations represent fundamental pieces of the Earth's climate system.

[3] The oceanic internal wavefield is "complex." It spans a vast range of scales: in the time domain, periods range from about 1 day for inertial waves to a few minutes for buoyancy frequency waves in the pycnocline. Horizontal wavelengths range from a few meters to hundreds of kilometers. The internal wave field's complexity arises not just from its extended range of scales but also from a multiplicity of possible sources at the surface (atmospheric forcing associated with wind stress and buoyancy fluxes) and bottom (tides and mean currents impinging upon nonuniform topography), the potential for scale transformations (reflection and scattering from topography) and dissipation at the bottom boundary, and interior transfers of energy and momentum through wave mean flow interactions. A significant sink is wave breaking, which is believed to be the product of nonlinearity resulting in downscale transfers of energy.

[4] Despite, or perhaps because of, this complexity, a universal character is usually ascribed to the oceanic internal wave energy spectrum. In a classic work, *Garrett and Munk* [1972] demonstrated how observations from various sensor types could be synthesized into a combined wavenumber-frequency spectrum, now called the Garrett and Munk (GM) spectrum of internal waves. Consistent only with linear internal wave kinematics, the GM spectrum was developed as an empirical curve fit to available data. Deviations have been noted near boundaries [*Wunsch and Webb*, 1979; *Polzin*, 2004b] and at the equator [*Eriksen*, 1985a]. However, our notion of what constitutes the background wavefield has remained static since the last significant model revision provided by *Cairns and Williams* [1976].

[5] The authors' sentiments are captured by *Briscoe* [1975a, p. 592]:

> The single paper motivating the most comments, experiments, and disquiet in a lot of readers was *Garrett and Munk* [1972], now called familiarly GM72. (The updated version is *Garrett and Munk* [1975], called GM75.) The paper is a virtuoso orchestration of synthesis, approximation, boldness, normalization, and implication. Starting from the observation that the wavenumber-frequency ($\omega - \kappa$) spectrum of a multimodal dispersive system is not uniquely determined by pure wavenumber and pure frequency spectra, the paper goes onto construct from linear dynamics and WKBJ methods an $\omega - \kappa$ spectrum that is astonishingly consistent with many kinds of data from all kinds of instruments. *Wunsch* [1975] iconoclastically discusses the pitfalls of such an approach and correctly emphasizes the fact that the dynamically important trait is the inconsistency of various data sets with some base state model.

With immense inspiration provided by C. J. R. Garrett and W. H. Munk, we take up, after 35 years, the difficult task posed by C. Wunsch. We document variability of the oceanic internal wavefield and then review the field to assess the dynamical underpinnings of that variability. While heavily referenced, this work does not attempt to be a literature review.

[6] In previous work [*Lvov et al.*, 2004] we noted that deviations of frequency and vertical wavenumber power laws from the universal model tend to covary: whiter frequency spectra are partnered with redder vertical wavenumber spectra. Here we provide a more systematic study of such deviations. We define spatial and temporal patterns of spectral parameters (amplitude, power laws, bandwidth, and separability) in a review of many observational programs of the last 4 decades. Having documented variability in the background wavefield, we interpret the spatial patterns in terms of generation, nonlinearity, wave mean interactions, and dissipation.

[7] Nonlinearity plays a key role. In a companion piece [*Lvov et al.*, 2010] we discuss the application of wave turbulence formalisms to this problem and rigorously demonstrate the validity of conventional wisdom regarding a truncated analytic approximation to nonlinear spectral transfers described by *McComas and Müller* [1981a, 1981b]. The observed power law combinations in frequency and vertical wavenumber documented here are largely consistent with the stationary states associated with the truncated analytic approximations. While this appears to be a stunning affirmation of this approximation to the wave turbulence transfer integral, it comes with caveats, disclaimers, and possible contradictions. First, the theory is not formally valid at high wavenumber for realistic wave amplitudes. Second, the identification of GM76 being a stationary state is only true after integration over the frequency domain and invocation of dissipation. Finally, numerical evaluations of the nonlinear transfers are inconsistent with the high-frequency, high vertical wavenumber domain of GM76 being a stationary state. This tension also applies to other stationary states identified by the truncated analytic theory having power law combinations associated with energy transfers from larger to smaller vertical scales and from higher to lower frequencies. Such stationary states require an energy source at high frequencies. But our review of the remaining generation and spectral transport mechanisms does not yet reveal what this mechanism might be.

[8] The article is organized as follows: In section 2 we summarize the development of the GM model through its various incarnations. We then review and reanalyze data obtained by major internal wave observational programs of the last 4 decades in section 3. These data clearly demonstrate that deviations from the GM spectrum are not random but rather form a distinct pattern, which we summarize in section 4. We discuss the theoretical framework which may be used to interpret these observations in section 5 and conclude in section 6. Metadata are tabulated in Appendix A, Appendix B contains additional useful information relating to instrument response issues, and processing methods are summarized in Appendix C. A regional spectrum for the Sargasso Sea is presented in Appendix D.

2. BACKGROUND

2.1. Kinematic Structure

2.1.1. Dispersion Relation

[9] Internal waves arise through the restoring force of gravity in a stably stratified fluid. In a rotating system they comprise a "fast" mode of oscillation with frequencies between inertial f and buoyancy N frequencies. In terms of

an Eulerian description with velocity vector $\mathbf{u} = (u, v, w)$, the linearized equations of motions are

$$u_t - fv = -\pi_x,$$

$$v_t + fu = -\pi_y,$$

$$w_t = -\pi_z - b,$$

$$\rho_t + w\overline{\rho}_z = 0,$$

$$u_x + v_y + w_z = 0,$$

in which kinematic pressure $\pi = p/\rho_o$ and buoyancy $b = -g\rho/\rho_o$ are perturbations from a hydrostatically balanced equilibrium state, $\overline{\pi}_z = -\overline{b}$, g is gravity, and the fluid is assumed to be incompressible ($\nabla \cdot \mathbf{u} = 0$). We use $\mathbf{r} = (x, y, z)$ as a position vector. An overbar ($\overline{\phi}$) indicates a mean on time scales much longer than a wave period. The constant ρ_o is the mean density and arises from assuming density to be constant in computing momentum changes associated with accelerations but taking density changes into account when they give rise to buoyancy forces (the Boussinesq approximation). The buoyancy gradient relates to oscillations of frequency $N = \sqrt{\overline{b}_z} = \sqrt{-g\overline{\rho}_z/\rho_o}$ corresponding to periods of minutes in the upper ocean to hours in the abyss. This work is concerned almost exclusively with horizontal scales small enough that the Earth's rate of rotation about the local vertical, $f = 2\Omega$ sin(latitude), can be considered as constant (the f plane approximation). The rate of rotation of the Earth about its axis is Ω. The Coriolis frequency f thus corresponds to periods of 1/2 day at the poles to several days in the tropics and vanishes at the equator. The foundation for interpreting observations lies in linear polarization relations (section 2.1.2) obtained from these equations of motion.

[10] The equations of motion can be manipulated to obtain a wave equation in vertical velocity [e.g., *Gill*, 1982]:

$$\left(\partial_t^2 + f^2\right)\partial_z^2 w + \left[N^2(z) + \partial_t^2\right]\left(\partial_x^2 + \partial_y^2\right)w = 0 \qquad (1)$$

for arbitrary stratification profile $N^2(z)$. Assuming that the background stratification is constant, plane wave solutions $w = w_o\, e^{i[\mathbf{r}\cdot\mathbf{p} - \sigma t]}$ with three-dimensional wave vector $\mathbf{p} = (k, l, m)$ having vertical component m and horizontal magnitude $k_h = |\mathbf{k}|$ return

$$\sigma_{\mathbf{p}} = \pm\sqrt{\frac{m^2 f^2 + N^2 k_h^2}{m^2 + k_h^2}}, \qquad (2)$$

which can be rewritten as

$$\frac{\sigma^2 - f^2}{N^2 - \sigma^2} = \frac{k_h^2}{m^2}.$$

[11] Many of the important properties of internal waves are immediately available:

[12] 1. Incompressibility ($\nabla \cdot \mathbf{u} = 0$) and a plane wave solution imply that particle velocities are normal to the wave vector, $\mathbf{p} \cdot \mathbf{u} = 0$.

[13] 2. Freely propagating waves, for which $\mathbf{p}$ is real, require $f < |\sigma| < N$.

[14] 3. Wave frequency solely determines the angle of the wave vector $\mathbf{p}$ relative to the vertical and, since $\mathbf{p} \cdot \mathbf{u} = 0$, the ratio of horizontal to vertical velocity.

[15] 4. The group velocity $\mathbf{C_g} = \nabla_{\mathbf{p}}\sigma$ (= [$\sigma\, k/k_h^2$, $\sigma l/k_h^2$, $-\sigma/m$] if $f^2 \ll \sigma^2 \ll N^2$) has the "odd" property that crests and troughs (i.e., lines of constant phase) propagate in the same direction as a wave packet (group) in the horizontal but the signs of phase and group velocity differ in the vertical coordinate. Upward phase propagation implies downward energy propagation.

2.1.2. Polarization Relations

[16] A suite of diagnostic relations can be obtained by assuming constant stratification rate, plane wave solutions in which all variables are proportional to $e^{i(\mathbf{p}\cdot\mathbf{r} - \sigma t)}$ and expressing the dependent variables in terms of wave amplitude a:

$$u = \left[\frac{k_h^2}{m^2|\mathbf{p}|^2}\right]^{1/2} \frac{m^2(k - ifl/\sigma)}{k_h^2} a e^{i(\mathbf{p}\cdot\mathbf{r} - \sigma t)}, \qquad (3)$$

$$v = \left[\frac{k_h^2}{m^2|\mathbf{p}|^2}\right]^{1/2} \frac{m^2(l + ifk/\sigma)}{k_h^2} a e^{i(\mathbf{p}\cdot\mathbf{r} - \sigma t)}, \qquad (4)$$

$$w = \left[\frac{k_h^2}{m^2|\mathbf{p}|^2}\right]^{1/2} - ma e^{i(\mathbf{p}\cdot\mathbf{r} - \sigma t)}, \qquad (5)$$

$$b = \left[\frac{k_h^2}{m^2|\mathbf{p}|^2}\right]^{1/2} - \frac{imN^2}{\sigma} a e^{i(\mathbf{p}\cdot\mathbf{r} - \sigma t)}, \qquad (6)$$

$$\pi = \left[\frac{k_h^2}{m^2|\mathbf{p}|^2}\right]^{1/2} - \frac{(N^2 - \sigma^2)}{\sigma} a e^{i(\mathbf{p}\cdot\mathbf{r} - \sigma t)}. \qquad (7)$$

The prefactor in these polarization relations is such that the wave amplitude a is normalized to represent the total energy:

$$E_k + E_v + E_p = aa^*. \qquad (8)$$

The total energy is the sum of horizontal kinetic E_k, vertical kinetic E_v, and potential $E_p = (1/2)\, N^2\eta^2$ energy in which η represents the vertical displacement.

[17] Two important diagnostics utilized here are the following:

[18] First, assuming constant stratification, the ratio of horizontal kinetic to potential energy for a single internal wave is

$$\frac{E_k}{E_p} = \frac{uu^* + vv^*}{bb^* N^{-2}} = \frac{\sigma^2 + f^2}{\sigma^2 - f^2}\frac{N^2 - \sigma^2}{N^2}. \qquad (9)$$

Second, the horizontal velocity trace for high-frequency internal waves is rectilinearly polarized. Rotation alters this so that the velocity trace at inertial frequency inscribes a circle with time. With depth, the near-inertial velocity vector traces out an elliptical helix in which the ratio of velocity

variance in the clockwise (E_{cw}) and counterclockwise (E_{ccw}) rotating components is given by

$$\frac{E_{cw}}{E_{ccw}} = \frac{(u-iv)(u-iv)^*}{(u+iv)(u+iv)^*} = \frac{(\sigma+f)^2}{(\sigma-f)^2}, \tag{10}$$

with the sign convention that positive frequency $f < \sigma < N$ implies upward phase propagation (and hence downward energy propagation) in the Northern Hemisphere.

2.1.3. Weak Spatial Inhomogeneities

[19] If the stratification profile varies much more slowly than the wave phase, a WKB approximation for vertically propagating waves provides the approximate solution to (1):

$$w \propto N(z)^{-1/2} e^{\frac{\pm i k_h}{\sqrt{\sigma^2 - f^2}} \int N(z) \mathrm{d}z}, \tag{11}$$

and so the effects of a variable buoyancy profile can be accounted for by stretching the depth coordinate by N. This amounts to scaling the vertical wavenumber by N/N_o, in which N_o is a reference stratification. The value N_o = 3 cph is often used. The buoyancy scaling of other dependent variables follows from polarization relations (3)–(7). The use of the WKB approximation requires $\sigma^2 \ll N^2$. If this relation is not satisfied, solutions can be found by treating (1) as an eigenvalue problem with appropriate boundary conditions. If $\sigma^2 \ll N^2$ but the wave phase is not slowly varying, the boundary conditions are that $w = 0$ at the top ($z = H$) and bottom ($z = 0$), which then implies that the horizontal velocities $[u(z), v(z)]$ are proportional to

$$N(z)^{1/2} \cos\left(n\pi \int_0^z N(z')dz' \Big/ \int_0^H N(z')dz' \right) \tag{12}$$

for integer values of n.

[20] Similarly, one can investigate interactions of the internal wavefield with a mean velocity field by assuming that the internal wavefield has small amplitude and small spatial scales relative to a time-independent geostrophically balanced flow (section 5.2). This problem is amenable to WKB and ray tracing techniques. In this slowly varying limit, the linear polarization relations reported here are modified by replacing the Eulerian frequency σ with the intrinsic frequency $\omega = \sigma - \mathbf{p} \cdot \overline{\mathbf{u}}$.

2.1.4. Slow Oscillations

[21] Internal waves are to be distinguished from a "slow" mode consisting of, at lowest order, the steady geostrophic balance.

$$fv = \pi_x,$$

$$fu = -\pi_y,$$

$$0 = -\pi_z - b,$$

$$w\overline{\rho}_z = 0,$$

$$u_x + v_y = 0.$$

Higher-order contributions are time dependence, nonlinearity, and the effects of a variable rate of planetary rotation (f). Substitution of a plane wave solution into the geostrophic balance returns primarily the information that small aspect ratio fluctuations ($k_h/m \ll f/N$) have E_k/E_p ratios of less than 1.

[22] There are two main paradigms for considering these slow motions vis-á-vis the fast internal wavefield. The first, already alluded to, is the limit that geostrophic velocities are larger and have significantly larger spatial scales. The second paradigm comes about as the two share similar spatial scales. In this instance the slow motions have typically smaller amplitudes and hence appear as a "contamination" to the wavefield. Beyond the issue of aspect ratio, the consistency relations for this nonpropagating mode have little diagnostic utility, and this "contamination field" has the character of uncorrelated noise, which is the content of several diagnostic studies [*D'Asaro and Morehead*, 1991; *Kunze and Sanford*, 1993]. The characterization of this slow mode as "noise" should not be surprising. The dynamics in this limit are those of stratified rotating turbulence in which motions at different isopycnals are uncoupled at scales larger than those over which shear instabilities can develop [*Riley and Lelong*, 2000].

[23] While diagnostic models of the slow mode usually assume an incoherent field [*Müller et al.*, 1978], the interaction of the internal wavefield with quasi-permanent density fine structure can be exploited by assuming the wavefield buoyancy scales on the density fine structure [*Polzin et al.*, 2003]. This buoyancy scaling (11) results in a correlation between internal wave shear and quasi-permanent density gradients when such a correlation is inconsistent with fields composed of either pure waves or pure fine structure. This enables an estimate of the quasi-permanent spectrum [*Polzin et al.*, 2003] (section 3.3.4).

[24] One fine structure consistency relation has great conceptual importance. The plane wave solutions of internal waves have no Ertel potential vorticity signature, whereas the nonwaves have nonzero Ertel potential vorticity [*Müller et al.*, 1986]. The distinction is important for issues of isopycnal dispersion [*Polzin and Ferrari*, 2004] and for dynamics [*Müller*, 1995].

[25] Reliance upon the plane wave solutions of $ae^{i[\mathbf{r}\cdot\mathbf{p}-\sigma t]}$, however, has its limitations. While internal waves and slow modes can be distinguished in terms of Ertel potential vorticity content, this distinction disappears when one considers a slowly varying wave packet with spatial structure in both horizontal directions, i.e., solutions of the form

$$a \rightarrow a(x,y)e^{i[\mathbf{r}\cdot\mathbf{p}-\sigma t]}.$$

See *Bühler and McIntyre* [2005] and *Polzin* [2008] for further details.

2.2. Parametric Spectral Representations

[26] Much of the original *Garrett and Munk* [1972] paper is a demonstration of how observations from various sensor types could be synthesized into a combined wavenumber-frequency spectrum consistent with linear internal wave

kinematics. The toolbox contains (1) a linear internal wave dispersion relation (equation (2)) to transfer from one domain to another, e.g.,

$$E(k_h)dk_h = E(m)dm,$$

in which dk_h/dm follows from equation (2); (2) diagnostic relations (section 2.1.2) to test consistency with linear wave kinematics; and (3) the choice of a vertical spectral rather than modal representation, which implies the invocation of an "equivalent continuum" in which the waves are assumed to be vertically propagating (boundary conditions and turning points are neglected; see *Garrett and Munk* [1972] for a discussion of modal properties). Assuming that the buoyancy profile varies much more slowly than the wave phase implies that the total energy E, obtained as an integral of the energy density over the spectral domain,

$$E = \int E(\mathbf{k},\sigma)d\mathbf{k}d\sigma = \int E(m,\sigma)dmd\sigma, \tag{13}$$

varies as

$$E = E_o\frac{N}{N_o}; \tag{14}$$

that is, E/N is an adiabatic invariant. The energy spectrum is denoted as E with following arguments (e.g., $E(\sigma)$). The variable E without following arguments represents total energy. The factors E_o and N_o represent reference values for the total energy of the internal wavefield and stratification.

[27] Garrett and Munk proposed that the spectral energy density can be represented as a separable function, i.e., the product of a function A of vertical wavenumber only and function B of wave frequency only:

$$E(\sigma,m) = EA\left(\frac{m}{m_*}\right)B(\sigma), \tag{15}$$

where m_* is a fixed reference wavenumber. This reference wavenumber is conveniently expressed as

$$m_* = \pi j_*/b, \tag{16}$$

in which the variable j represents the mode number of an ocean with an exponential buoyancy frequency profile having a scale height of b (b = 1300 m in the GM model). Separability in vertical wavenumber and frequency was invoked as the simplest representation not inconsistent with available data. The spectral amplitude was regarded as being independent of spatial coordinates apart from the dictates of buoyancy scaling. Use of nonseparable and anisotropic parametric spectral representations is described by *Müller et al.* [1978].

[28] It is convenient to normalize functions $A(x = m/m_*)$ and $B(\sigma)$ to unity, so that the integrals

$$\int_{m_1/2m_*}^{m_c/m_*} A(x)\mathrm{d}x \cong \int_0^\infty A(x)\mathrm{d}x = 1$$

and

$$\int_f^N B(\sigma)\mathrm{d}\sigma \cong \int_f^\infty B(\sigma)\mathrm{d}\sigma = 1$$

are dimensionless, and in practice, the limits of integration (m_1 represents vertical mode 1, and m_c is a high-wavenumber cutoff of approximately 0.1 cpm) are approximated for analytic convenience. The high-wavenumber cutoff, defined by

$$\int_0^{m_c} 2m^2E_k(m)dm = \frac{2\pi}{10}N^2, \tag{17}$$

represents an observed transition to steeper spectral slopes and likely signifies a dynamical transition to a more strongly nonlinear, yet not turbulent, regime.

[29] The GM model evolved over time, resulting in three major versions, denoted GM72, GM75, and GM76:

GM72

$$A\left(\frac{m}{m_*}\right) = \begin{cases} m_*^{-1}, & \text{if } m < m_* \\ 0, & \text{if } m < m_* \end{cases}$$

GM75 and GM76 (18)

$$A\left(\frac{m}{m_*}\right) = \frac{s\Gamma\left(\frac{t}{s}\right)}{\Gamma\left(\frac{1}{s}\right)\Gamma\left(\frac{t-1}{s}\right)}\frac{m_*^{-1}}{\left[1+\left(m/m_*\right)^s\right]^{-t/s}}$$

with

$$\left(s,t,j_*\right) = \begin{cases} (1,2.5,6) & \text{GM75} \\ (2,2,3) & \text{GM76} \end{cases}$$

and

$$B(\sigma) \propto \sigma^{-r+2q}\left(\sigma^2-f^2\right)^{-q}. \tag{19}$$

The gamma function (Γ) appears in the normalization for the vertical spectrum. All versions of GM utilize r = 1 and q = 1/2, so that

$$B(\sigma; r=1, q=1/2) = \frac{2f}{\pi}\frac{1}{\sigma\sqrt{\sigma^2-f^2}}.$$

Both functions $A(x = m/m_*)$ and $B(\sigma)$ behave as power laws at high wavenumber and frequency; B has an integrable singularity at the inertial frequency f (which constrains $q < 1$), and A has a plateau for small value of its argument. As explained below, these features were found to be representative of the oceanic internal wave field.

[30] The total energy in the model,

$$E_o^{\mathrm{GM}} = 30\times10^{-4}\,\mathrm{m^2s^{-2}}, \tag{20}$$

is based upon fits to observed high-frequency spectra rather than estimates of total observed internal wave band energy. Consistency between a total energy of 30×10^{-4} m^2 s^{-2}, cutoff wavenumber (17), and parameteric values $(s, t) = (2, 2)$ requires $j_* = 4$ rather than $j_* = 3$ when using $(s, t) = (1, 2)$.

2.3. The GM Model's Three Incarnations

[31] The GM model evolved over time as more and better data became available. This section documents reasons behind the choice of specific parameters.

2.3.1. Frequency Domain

[32] While *Garrett and Munk* [1972] noted variability in the tidal peak, the tides are not part of the GM model. The specific shape of the inertial peak was simply chosen out of analytic convenience. Variability in the frequency domain power law was apparent even then, with a noted alternative being $\sigma^{-5/3}$ [*Webster*, 1969]. With many possible "noise" sources such as mooring motion and fine structure contamination serving to whiten the frequency spectrum, the judicious choice for a model of the background spectrum is a redder σ^{-2} (section 3.3.1). This choice remains stable throughout the various model versions.

2.3.2. Vertical Wavenumber Domain

[33] The spatial domain information available in the late 1960s was limited to stationary current meters and horizontally towed thermistor chains. The direct information available from current meters was through spatial lag coherences. Estimates of vertical bandwidth j_* can be obtained by assuming a parametric spectral representation and fitting lagged coherence estimates to the inverse Fourier transform of the spectrum [*Garrett and Munk*, 1972; *Cairns*, 1975; *Müller et al.*, 1978]. This technique can be found in many textbooks as the Wiener-Khinchine relation. The towed data return both a direct estimate of the horizontal spectrum and vertical lag coherence information. These data supported only a crude representation of the vertical wavenumber spectrum as a top hat model with about 20 equivalent modes excited ($j_* = 20$ in GM72).

[34] The quality of the information improved dramatically in the early 1970s with the introduction of near-continuous vertically profiling instrumentation such as the Neil Brown conductivity-temperature-depth (CTD) profiler [*Brown*, 1974] and Tom Sanford's electric field sensing device [*Sanford*, 1975]. The choice of which data to rely upon, though, is quite subjective, and the perception is that fine structure contamination of the density field is more problematic than contamination of the velocity field [e.g., *Polzin et al.*, 2003]. Extant temperature gradient spectra tended to be white at an intermediate range of vertical wavenumbers (roughly $0.01 \le m \le 0.2$ cpm) and roll off thereafter. GM75, however, relied upon even higher wavenumber CTD data from *Millard* [1972], ignored possible inconsistencies with CTD data given by *Hayes* [1975], and heavily weighted the velocity profile data given by *Sanford* [1975] to argue for a high-wavenumber slope $t = 5/2$. See section 3.3.2 for a discussion of the *Sanford* [1975] data set. Estimates of isotherm fluctuations from a vertically profiling float [*Cairns*, 1975] suggested a much lower bandwidth ($j_* = 6$) than in the GM72 model.

[35] GM75 was soon replaced by a more refined model. Further analysis of float data by *Cairns and Williams* [1976] suggested revision of the high-wavenumber power law to m^{-2} and a change to the functional form $1/(m_*^2 + m^2)$. The rationale given for choosing such a functional form is its analytic convenience: $1/(m_*^2 + m^2)$ has a simple cosine transform [see also *Desaubies*, 1976]. *Munk* [1981] follows suit. This revision is labeled GM76. The distinction between $1/(m_* + m)^2$ and $1/(m_*^2 + m^2)$ is in the rapidity of the roll-off from the low-wavenumber plateau region to the high-wavenumber asymptote. GM76 has a more rapid transition than GM75 for equivalent power laws.

3. OBSERVATIONS OF INTERNAL WAVE SPECTRA

3.1. Observational Framework and Preliminary Notes

[36] Observations of the oceanic internal wave field are analyzed in this section in order to define the extent to which the deep ocean internal wavefield is indeed universal. We follow the lead of GM by characterizing observed spectra with the parametric power law representations (18) and (19) and also allow for variable spectral levels with the focus upon identifying spatial and temporal variability of the spectral parameters.

[37] Variability in the frequency domain is quantified by fitting

$$E(\sigma) = EB(\sigma; r, q = 1/2) \propto e_o \sigma^{-r+1} \left(\sigma^2 - f^2\right)^{-1/2} \qquad (21)$$

to the high-frequency portion of the observed spectra. "High" frequency refers to periods less than 10 h, thereby eliminating the inertial peak and semidiurnal tides from consideration. The amplitude e_o is reported as a fraction of the energy associated with the GM spectrum:

$$e_o = \frac{\int_f^N EB(\sigma; r, q = 1/2) d\sigma}{E_o^{GM} N / N_o}. \qquad (22)$$

[38] An additional reported statistic is the total internal wave band energy in the observed spectrum. Internal wave band energy is estimated by integrating the observed frequency spectra over frequencies greater than approximately $0.7f$, thereby including broadening of the inertial cusp.

[39] Variability in the vertical wavenumber domain is quantified by fitting variants of (18) to the observed spectra. The resulting statistics are less satisfactory than those in the frequency domain as low wavenumbers are not well resolved in most instances.

3.2. Some Words of Caution

[40] Power laws are an attractive and simple way to describe complex systems in general and internal waves in particular. Some details of the observed spectra may defy this simple approach. Our view is to treat the parametric representation as a general tendency to help summarize and interpret otherwise complicated data. With that caveat, there is no shortage of reasons for the observed variability: nonlinearity, instrumentation, the buoyancy profile, low-frequency flows, tides, bathymetry, horizontal inhomogeneity, vertical asymmetry, and contamination by either quasi-permanent fine structure or self advection (Doppler shifting) within the internal wavefield:

[41] 1. How you look at the ocean matters. Instrument response and processing methods may affect the interpre-

tation. Appendices B and C contain remarks to aid the reader in negotiating this maze.

[42] 2. All that wiggles is not necessarily an internal wave. Internal waves typically dominate the small-scale variability, and geostrophically balanced motions dominate the largest scales. But quasi-permanent fine structure has been identified as making an increasing contribution to the total spectrum at high wavenumber [e.g., *Müller et al.*, 1978; *Polzin et al.*, 2003] (section 2.1.4).

[43] 3. In many cases, the quoted spectral power laws are derived from one-dimensional (vertical wavenumber and frequency) spectra. Thus, there is an implicit assumption that the spectra are separable (equation (15)). Since both 1-D spectra are red, frequency spectra are typically dominated by low vertical wavenumber motions, and vertical wavenumber spectra are dominated by low frequencies. The one-dimensional power laws are not identical to the 2-D power laws if the spectra are nonseparable.

[44] 4. The sampling strategy matters. Vertical wavenumber-frequency domain information is seldom obtained from a single instrument, nor are the measurements taken instantaneously. Vertical profile data obtained as a spatial survey can be used to define a spatial mean and residuals, and the internal wave contribution can be identified as the residual field. However, this will alias some low-frequency variability into the residual fields. Vertical profile data obtained as a time series can effectively separate the internal wave variability from lower-frequency motions. But the resulting residuals may not be representative of the background wavefield: that background may be temporarily distorted, for example, by wave mean interactions.

[45] 5. Anisotropic propagation in a region of variable stratification or into or away from a critical layer can imply significant transport of energy in the vertical wavenumber domain and thereby can create apparent structure unrelated to nonlinearity.

[46] 6. The results presented here are primarily from analyses in depth or pressure coordinates, rather than in an isopycnal coordinate system. High-frequency Eulerian spectra are prone to Doppler shift contamination at high vertical wavenumber. Use of an isopycnal coordinate system limits the Doppler shift contamination [*Sherman and Pinkel*, 1991].

[47] Despite these limitations, we believe that the patterns of spatial and temporal variability discussed below reflect physical reality and are not an artifact of processing or interpretation.

3.3. A Regional Catalog

[48] Variability of the oceanic internal wave spectrum will likely exist on multiple temporal and spatial scales, e.g., those scales associated with individual wave packets and isolated forcing events. In the present study we assume that differences in the background spectrum are a product of regional differences in forcing and boundary conditions averaged over the characteristic time scale to dissipate the energy resident in the internal wavefield (about 50 days) and averaged over the characteristic spatial scale that internal waves can propagate in that time span. The forcing mechanisms and propagation scales are, in general, not regionally well defined.

[49] Thus, multiple data sets from Site D (north of the Gulf Stream), the Sargasso Sea, and the California Current System are grouped together (Figure 1). In terms of low-frequency variability, Site D exhibits the largest eddy energy [e.g., *Wunsch*, 1997]. Eddy energies in the Sargasso Sea and California Current System exhibit spatial trends but are comparable to each other. Short narratives are used to document regional characterizations of eddy amplitudes, tides, and bottom topography.

3.3.1. Site D: $m^{-2.0}$ and $\sigma^{-2.0}$

[50] Site D was fourth of a series of stations on a section from Woods Hole to Bermuda. Historically, the technology for long-term current meter deployments was developed at Woods Hole, and Site D served as the test bed for much of that instrumentation. Much of the data in the original Garrett and Munk paper (GM72) came from Site D, if for no other reason than not much else was available. Site D is characterized by a relatively small amplitude tide and large low-frequency (predominantly topographic Rossby wave) activity [e.g., *Hogg*, 1981]. Site D is situated under the eastern seaboard storm track, resulting in an enhanced potential for the resonant coupling between wind stress and mixed layer at near-inertial frequencies [*D'Asaro*, 1985]. Site D may be relatively unique because of its geographic location.

[51] It is apparent that although many data were under consideration by *Garrett and Munk* [1972], the GM72 model is a curve fit to the original Site D data presented by *Foffonoff* [1969] in both amplitude and σ^{-2} power law (Figure 2). (Departures from a simple power law behavior are apparent in the thermocline data at high frequencies, and spectra from the deeper current meters do not roll off at frequencies exceeding the local N. Data from the very stable trimoored Internal Wave Experiment (IWEX) mooring roll off nicely (see below), and thus, *Briscoe* [1975b] suggests that the superbuoyancy extension is an artifact of mooring motion. On the other hand, this does not mean that the departures from a simple power law behavior apparent in the upper current meters are an artifact of mooring motion. See section B1 for further details.) The GM72 model is a good characterization of the spectral shape at Site D throughout the decades (Figure 3). However, variability is apparent in spectral amplitude.

[52] The original (1967) Site D data are characterized by larger spectral levels than the other, longer-term estimates. *Briscoe and Weller* [1984] document an annual cycle in high-frequency internal wave energy using data from the Long-Term Upper Ocean Study (LOTUS) region south of the Gulf Stream, with maximum values in winter. This annual cycle is also apparent in the Primer data from Site D (Figure 4). A seasonal cycle in near-inertial energy for this location is discussed in detail by *Silverthorne and Toole* [2009].

[53] With the GM spectrum being a curve fit to the early (1967) data and with those data being obtained in February–March, the GM model is essentially a description of the wintertime spectrum at Site D. The summertime spectrum

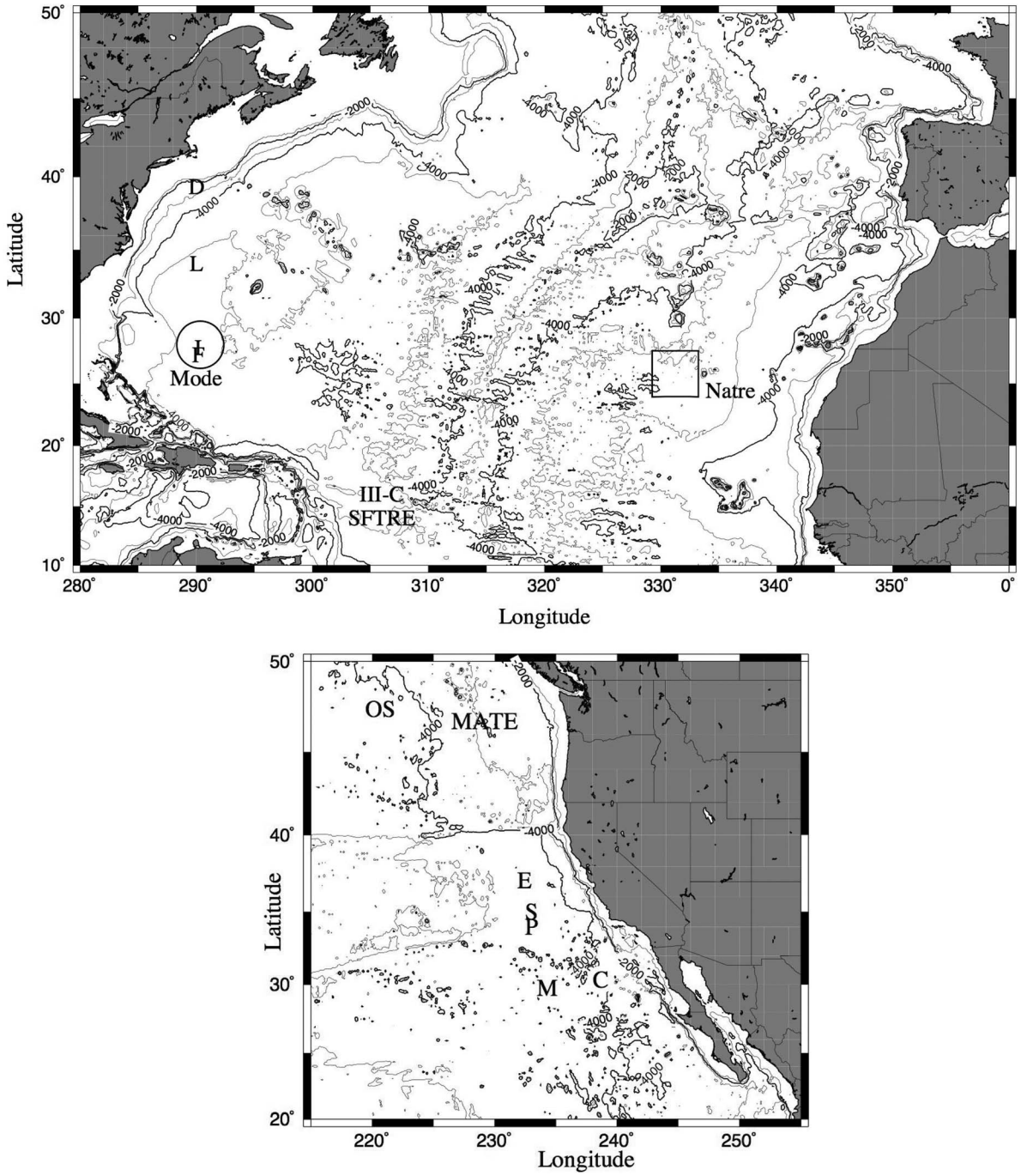

Figure 1. Geographic depictions of the data sets referred to in this study. Surveys for the Mid-Ocean Dynamics Experiment (MODE) and the North Atlantic Tracer Release Experiment (NATRE) are enclosed by the circle and square, respectively. This study uses current meter data from near the center of these survey regions. Abbreviations are as follows: D, Site D; I, Internal Wave Experiment; L, the Long-Term Upper Ocean Study; F, Frontal Air-Sea Interaction Experiment; III-C, PolyMode IIIc; SFTRE, the Salt Finger Tracer Release Experiment in the North Atlantic; S, SWAPP; P, PATCHEX; M, Misery 1 and 3 as referred to by *Cairns and Williams* [1976]; C, *Cairns* [1975]; E, the offshore array from the Eastern Boundary Currents field program [*Chereskin et al.*, 2000]; MATE, the Midocean Acoustic Transmission Experiment, [*Levine et al.*, 1986]; OS, Ocean Storms Experiment [*D'Asaro et al.*, 1995]. Bathymetric contours are every 1000 m, alternately bold and thin. The Gulf Stream lies shoreward of the 800 m isobath south of Cape Hatteras, cutting between Site D and the LOTUS region.

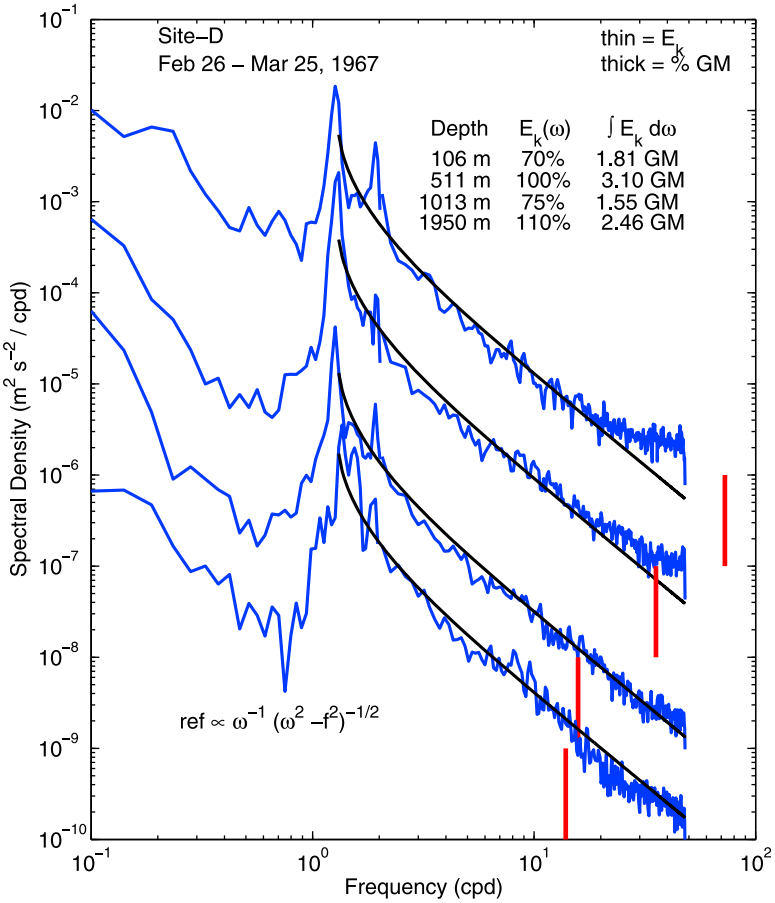

Figure 2. Site D frequency spectra of horizontal kinetic energy (blue lines). These are the Site D data that appeared in the original GM72 paper. Black curves represent fits of (21) with $r = 2$. The thick vertical lines represent the buoyancy frequency cutoff. The spectra have been offset by 1 decade for clarity.

has lower amplitude with little change in spectral slope at high frequency (Figure 5). We anticipate results presented below by stating here that annual average spectral levels at Site D tend to be larger than those at other places, and thus, being a fit to wintertime conditions, the Garrett and Munk model is a poor description of the background internal wavefield in much of the world ocean.

[54] Despite the vertical spectrum being defined using data obtained elsewhere, recent vertical profile data data from Site D are remarkably consistent with the GM76 model $(1/(m_*^2 + m^2))$ (Figure 6). Wintertime conditions exhibit both enhanced spectral levels (amplitude factors of 2.75 versus 1.75) and relatively more variance at low modes ($j_* = 4$–5 versus $j_* = 10$) than summertime data. Wintertime conditions also exhibit larger ratios of kinetic to potential energy at high wavenumber, implying an increased input of near-inertial energy during wintertime and relaxation to higher frequencies.

3.3.2. The Sargasso Sea

[55] A large number of experiments have been located in the Sargasso Sea over the Hatteras Abyssal Plain. On the southern side of the Gulf Stream, this region exhibits an energetic eddy field having significant north-south gradients. Eddy energy levels are typically less than noted at Site D. A tidal (M_2) peak is apparent in the temperature and velocity spectra. *Müller et al.* [1978] find that fluctuations at this frequency have larger characteristic vertical scales than the internal wave continuum, and there is evidence of similar features at the first several harmonics. From current meter data at 28°N, 70°W, *Noble* [1975] and *Hendry* [1977] estimate net fluxes at M_2 to be to the southeast and infer the source to be the Blake Escarpment, near the western boundary. *Alford and Zhao* [2007], on the other hand, document net semidiurnal fluxes to the north-northwest (at 31°N, 69° 30′W) and southwest (at 34°N, 70°W).

[56] The bottom near midbasin is well sedimented and smooth at 28°N, 70°W, the locus of the Mid-Ocean Dynamics Experiment and the Internal Wave Experiment. Rougher topography is noted to the east. (One also finds mud waves. Mud waves are sedimentary features of 1–10 km horizontal wavelength having amplitudes of tens to hundreds of meters. These horizontal scales are appropriate for the generation of freely propagating internal lee waves (with Eulerian frequency $\sigma = 0$) if the intrinsic frequency $\omega = \sigma - \mathbf{p} \cdot \overline{\mathbf{u}}$ lies between the Coriolis and buoyancy frequencies: $f \le \mathbf{p} \cdot \overline{\mathbf{u}} \le N$. Significant coupling between the "mean" and internal wavefield is anticipated at mean flow rates of 0.1–0.2 m s^{-1}. Sediment transport is an issue at such flow rates and the possibility exists that the lee wave velocity perturbations affect the deposition and erosion process so as to reinforce the mud waves [*Blumsack*, 1993]. But this gets

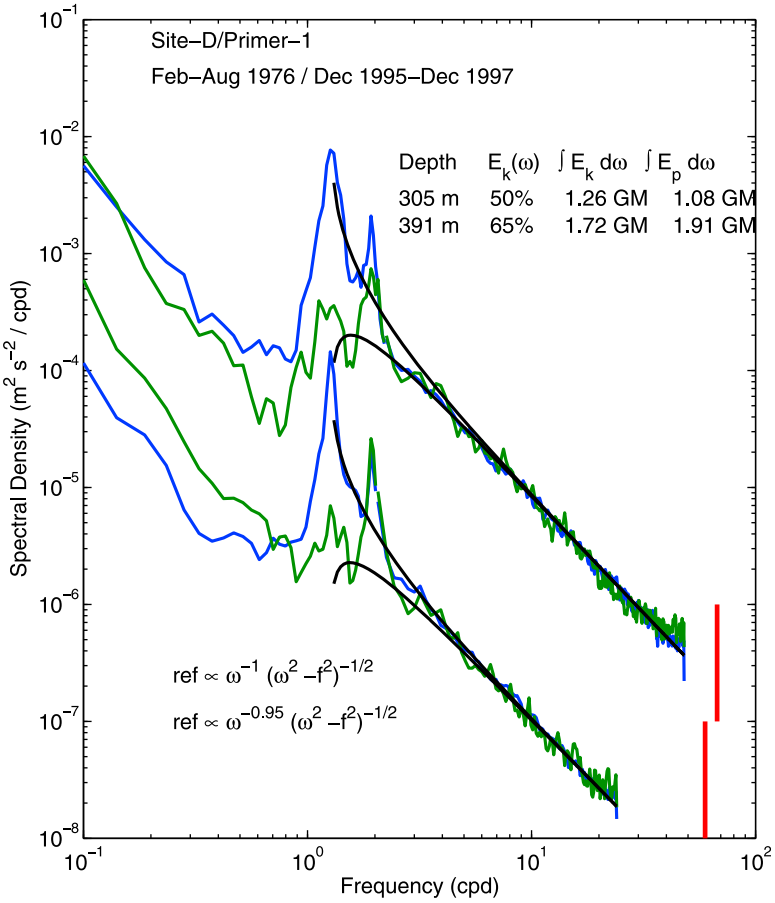

Figure 3. Frequency spectra of horizontal kinetic energy and potential energy (blue and green lines) from nearby Site D. Black curves represent fits of (21) with $r = 2$ and $r = 1.95$. Thick vertical lines represent the buoyancy frequency cutoff. The shape of the fit is stable throughout the 3 decades separating the data in the original GM72 work. Note that the spectral amplitude is somewhat lower than the GM model. The Primer-1 spectra have been offset by 1 decade for clarity.

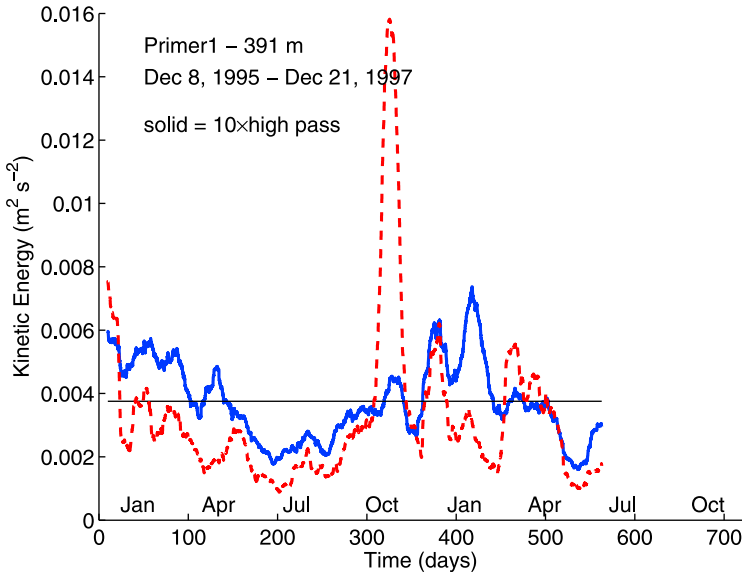

Figure 4. Site D time series of horizontal kinetic energy. The solid blue line represents 10 times the high-frequency energy. The dashed red line represents the entire internal wave band energy estimate. The last 150 days of this record were not included in this analysis as they were contaminated by biological fouling of the rotor.

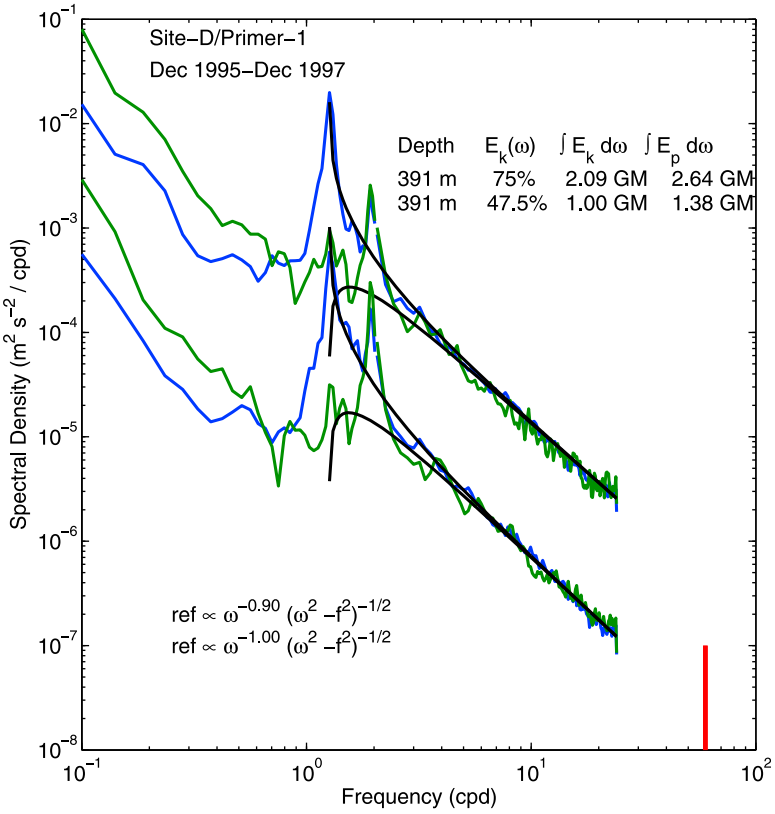

Figure 5. Frequency spectra of horizontal kinetic and potential energy (blue and green lines) from nearby Site D. The 2 year Primer data set has been divided into high- and low-amplitude states. The low-amplitude state has been offset 1 decade for clarity. Black curves represent fits of (21) with $r = 1.90$ (high-amplitude state) and $r = 2.00$ (low-amplitude state). The thick vertical line represents the buoyancy frequency cutoff.

us off the topic of the background internal wavefield.) The PolyMode Local Dynamics Experiment current meter array (at 31°N, 69° 30′W) is likely situated above relatively rough terrain. Bathymetry is relatively smooth at 34°N, 70°W, the locus of the Long-Term Upper Ocean Study.

[57] The buoyancy frequency profile has a relative minimum in $N(z)$ associated with the 18° water thermostad at about 300 m water depth. The main thermocline exhibits nearly constant stratification between 500 and 1000 m.

3.3.2.1. Mid-Ocean Dynamics Experiment

[58] Conducted during March–July 1973, the Mid-Ocean Dynamics Experiment (MODE) was one of the first concentrated studies of mesoscale ocean variability. The experiment featured arrays of moored current meters, neutrally buoyant floats, standard hydrographic station techniques, and the use of novel vertically profiling instrumentation. An extensive array of current meter moorings was deployed in a 300 km radius centered about (28°N, 69°40′W). Data return from the current meters was limited [*Mode-I Atlas Group*, 1977].

[59] While designed primarily to investigate low-frequency motions, the experiment returned a great deal of information about internal waves. Vertical profiles of horizontal velocity obtained during May and June with a free-falling instrument using a electric field sensing technique [*Sanford*, 1975] provided, for the first time, direct estimates of the high vertical wavenumber structure of the oceanic internal wavefield. These data are dominated by near-inertial frequencies, and a rotary decomposition in the vertical wavenumber domain [*Leaman and Sanford*, 1975] reveals a large excess of clockwise (cw) phase rotation with depth. Clockwise phase rotation with depth is a signature of downward energy propagation for near-inertial waves (10).

[60] Despite the evidence of excess downward energy propagation that was interpreted in terms of atmospheric generation [*Leaman*, 1976], these data were assumed to be representative of the background internal wavefield. A subset obtained as a time series of 4 1/2 days provided the basis for a revision to the isotropic Garrett and Munk spectral model, GM75, with high-wavenumber asymptote of $m^{-5/2}$.

[61] The MODE profile data were included in our original study [*Lvov et al.*, 2004] reporting the covariability of frequency-wavenumber power laws. Further investigation suggests that the characterization of these data as representing the background wavefield is problematic. Several coherent wave packets dominate the high-wavenumber energy content, and these packets can be interpreted as being strained by the mesoscale eddy field and propagating into a critical layer [*Polzin*, 2008]. Thus, wave mean interactions acting in conjunction with the downward propagating waves may be responsible for creating structure in the vertical wavenumber domain uncharacteristic of the background spectrum.

3.3.2.2. Internal Wave Experiment: $k^{-2.4\pm0.4}$ and $\sigma^{-1.75}$

[62] IWEX represents an early attempt to estimate a vector wavenumber-frequency spectrum with a minimum

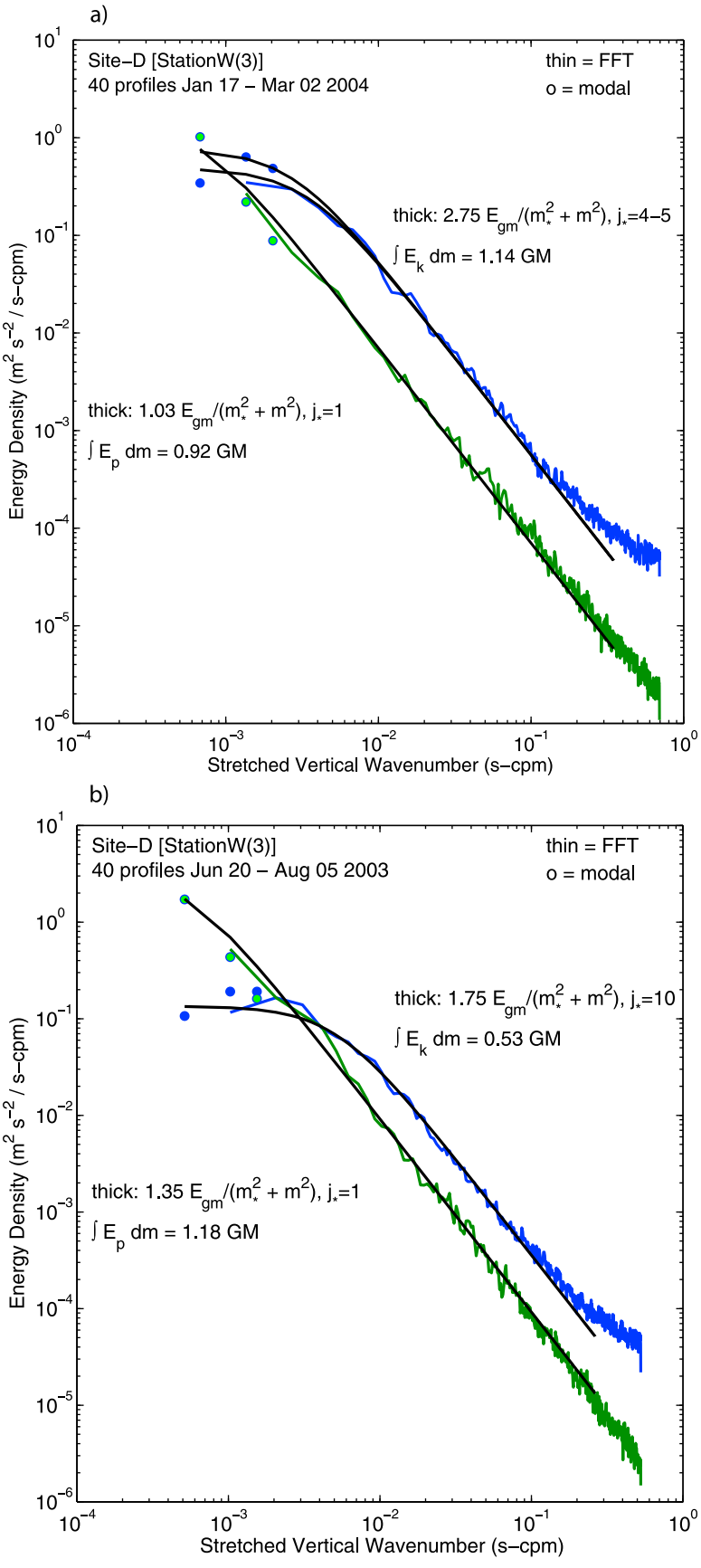
a)
Site–D [StationW(3)]
40 profiles Jan 17 – Mar 02 2004
thin = FFT
o = modal
thick: 2.75 E_gm/(m_*^2 + m^2), j_*=4–5
∫ E_k dm = 1.14 GM
thick: 1.03 E_gm/(m_*^2 + m^2), j_*=1
∫ E_p dm = 0.92 GM
Energy Density (m^2 s^-2 / s–cpm)
Stretched Vertical Wavenumber (s–cpm)
b)
Site–D [StationW(3)]
40 profiles Jun 20 – Aug 05 2003
thin = FFT
o = modal
thick: 1.75 E_gm/(m_*^2 + m^2), j_*=10
∫ E_k dm = 0.53 GM
thick: 1.35 E_gm/(m_*^2 + m^2), j_*=1
∫ E_p dm = 1.18 GM
Energy Density (m^2 s^-2 / s–cpm)
Stretched Vertical Wavenumber (s–cpm)

Figure 6

of assumptions. Current and temperature data were obtained with 17 vector-averaging current meters (VACMs) and three Geodyne 850 current meters from a taut, three-dimensional, trimoored array.

[63] *Müller et al.* [1978] assumed that the spectrum could be factorized as

$$E^{\pm}(k_h, \varphi, \sigma) = E^{\pm}(\sigma) A(k_h; \sigma) S(\varphi; \sigma),$$

with $E^{\pm}$ denoting the sign of vertical energy propagation, A denoting the normalized horizontal wavenumber (k_h) distribution, and S denoting a normalized azimuthal (φ) distribution. Their horizontal wavenumber distribution was assumed to have a parametric representation of

$$A(k_h; \sigma) \propto \left[1 + \left(\frac{k_h - k_p}{k_*}\right)^s\right]^{-t/s}$$

for $k_h > k_p$ and $A = 0$ otherwise. The parameters are horizontal wavenumber scale k_*, low-wavenumber cutoff k_p, shape factor s, and high-wavenumber slope t. An inverse analysis of the spatial lag cross spectra (the lag coherence is proportional to the Fourier transform of the energy spectrum) was performed to estimate the various parameters in their proposed spectrum. In particular, *Müller et al.* [1978] find that the horizontal wavenumber energy spectrum depends upon wavenumber as $k_h^{2.4\pm0.4}$, independent of frequency. For continuum ($f^2 \ll \sigma^2 \ll N^2$) frequencies the horizontal and vertical wavenumber power laws are identical. Thus, $E(m) \propto m^{-2.4\pm0.4}$. The observed frequency spectra of both velocity and temperature are characterized by the power law $\sigma^{-1.75}$ [*Briscoe*, 1975b] (Figure 7).

[64] The *Müller et al.* [1978] analysis includes an estimate of fine structure contamination. That is, their horizontal wavenumber spectrum includes only contributions which are consistent with linear internal waves. An increasing contamination with increasing frequency (decreasing horizontal scale) is apparent. As they make no distinction between permanent fine structure contamination and Doppler shifted internal waves, much of their fine structure contamination could be internal waves [e.g., *Sherman and Pinkel*, 1991; *Polzin et al.*, 2003]. Thus, the horizontal wavenumber domain power law estimate may be biased too steep.

[65] Several features of the IWEX data set reoccur in many of the other data sets analyzed here. The first is that estimates of amplitude based upon fits to the high-frequency part of the spectrum tend to be significantly lower than those in the GM model, whereas estimates of total energy tend to be more nearly equal to the total energy in the GM model. The inference is that the inertial cusp of the GM model is not sufficiently strong to describe the oceanic peak. While this has been noted before [e.g., *Fu*, 1981], the IWEX analysis indicates that the excess near-inertial energy has smaller characteristic vertical scales: At supertidal frequencies the peak wavenumber k_p corresponds to the first vertical mode. At near-inertial frequencies k_p corresponds to the third vertical mode, indicating significantly reduced near-inertial energy in the first two modes. This pattern is consistent with the vertical profile data presented here which depict ratios of E_k to E_p at 100 (1000) m, vertical wavelengths that are significantly larger (smaller) than in the GM model, for which $E_k/E_p = 3$.

[66] *Müller et al.* [1978] avoid interpreting the IWEX spectrum in the context of how it might relate to the background oceanic spectrum. We attribute this as being due to the short duration of the data set and the relative lack of quality data sets at that time. Here, however, we promote the IWEX spectrum as a more realistic representation of the Sargasso Sea background spectrum than the GM model.

3.3.2.3. Long-Term Upper Ocean Study: $\sigma^{-1.75}$–$\sigma^{-1.85}$

[67] One goal of LOTUS was to document variability in the internal wavefield over several seasons in order to investigate its association with a variety of forcing mechanisms and environmental conditions. Meteorological data were obtained with a surface mooring and buoy. Only data from subsurface moorings are described here. The region is notable for extreme air-sea buoyancy exchange resulting in the production of Eighteen Degree Water [e.g., *Kwon and Riser*, 2004].

[68] *Briscoe and Weller* [1984] document an annual cycle of high-frequency internal wave energy at 200–500 m depths from the first year's data. The energy was noted to vary from a half or a third to 2 or 3 times the mean at each depth. That signal is repeated in the second year's data (Figure 8). Apart from the seasonal cycle, internal wave energy varies on time scales of several weeks. The relation between this short time scale variability and low-frequency (subinertial) shear has been noted since MODE [see *Ruddick and Joyce*, 1979, and references therein].

[69] In this study of how nonlinearity may shape and form the internal wave spectrum, there is a potential link between spectral amplitude and spectral shape. The LOTUS spectra in the 325–350 m depth range (Figure 9) were averaged over the time periods indicated in Figure 8. Spectra from the more energetic time periods are slightly less steep ($\sigma^{-1.75}$ versus $\sigma^{-1.85}$) for a factor of 2.5 difference in spectral level. If there is a dynamical link between spectral level and spectral shape, that link is subtle relative to the gamut of variability discussed here.

Figure 6. Site D vertical wavenumber spectra of horizontal kinetic (blue) and potential (green) energy. The black line represents a fit of the GM76 spectrum. Spectral estimates at the lowest wavenumber (circles) were made using a modal fit. These data were acquired as part of a long-term climate monitoring project, Station W (unpublished data from J. Toole, personal communication, 2004). Velocity and density profiles were obtained with the Moored Profiler. Information regarding the internal wavefield is returned by burst sampling 4 times using a 9.5 h sampling interval, then waiting 5 days before repeating. The spectrum presented here represents departures from the burst means. See Appendix B for further details about the Moored Profiler. Departure from the curve fit at vertical wavelengths of 10 m and smaller is interpreted as noise.

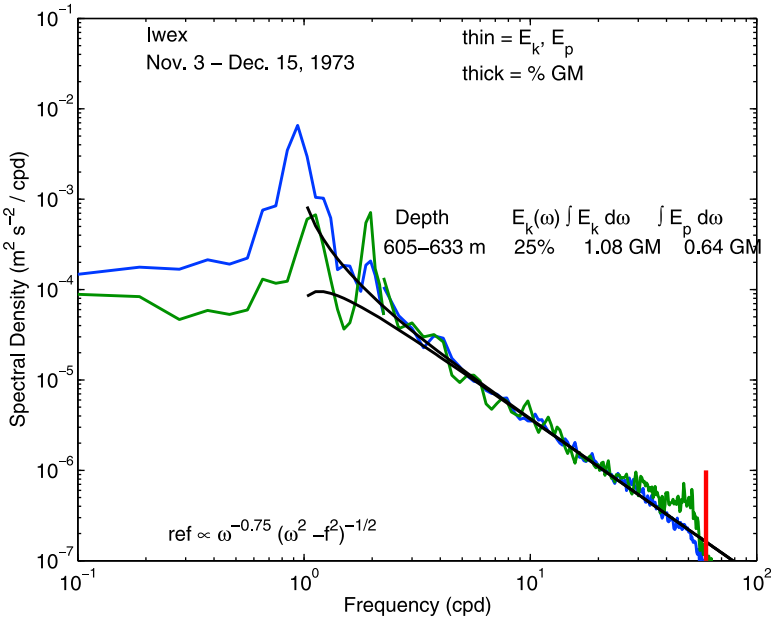

Figure 7. IWEX frequency spectra of horizontal kinetic energy and potential energy (blue and green lines). Black curves represent fits of (21) with $r = 1.75$. The thick vertical line represents the buoyancy frequency cutoff.

3.3.2.4. FASINEX: $m^{-2.3}$ and $\sigma^{-1.85}$

[70] The Frontal Air-Sea Interaction Experiment (FASINEX) was designed to investigate the response of the upper ocean to atmospheric forcing in the presence of oceanic fronts. An array of surface and subsurface moorings with vector-measuring current meters (VMCMs), VACMs, and profiling current meters was deployed in the subtropical convergence zone of the northwest Atlantic (approximately 27°N, 70°W) from January to June of 1986 [*Weller*, 1991; *Eriksen et al.*, 1991]. The moored data in this study are taken from a long-term, subsurface mooring at 28°N. These data document an annual cycle in internal wave energy that is sub-

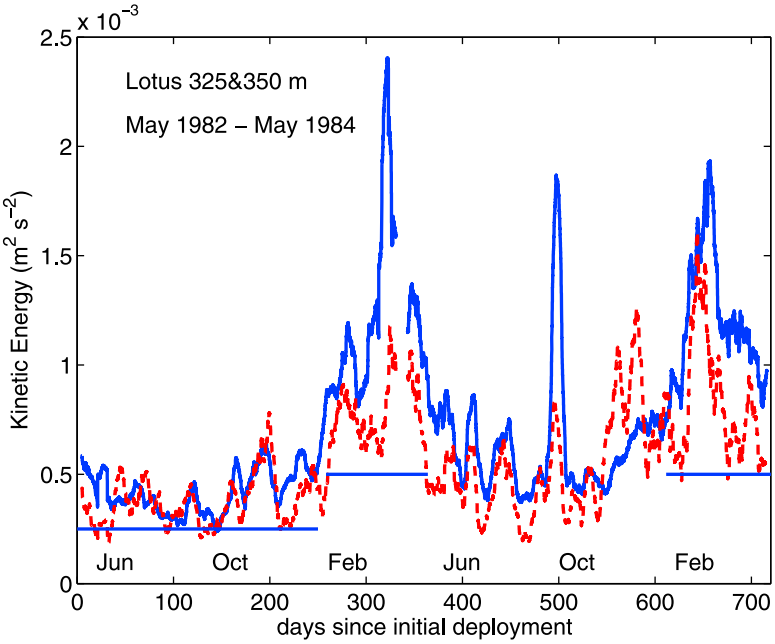

Figure 8. LOTUS time series of high-frequency energy from 325 (year 1) and 350 (year 2) m water depth. This depth range is occupied by 18 Degree Water and represents a local minimum in the stratification rate. Mixed layer depths were observed to be smaller than 300 m over the duration of the data set. The solid blue line represents 10 times the high-frequency energy. The dashed red line represents the entire internal wave band energy estimate. The horizontal lines indicate the time periods over which spectra were averaged into bins of high- and low-energy states in Figure 9.

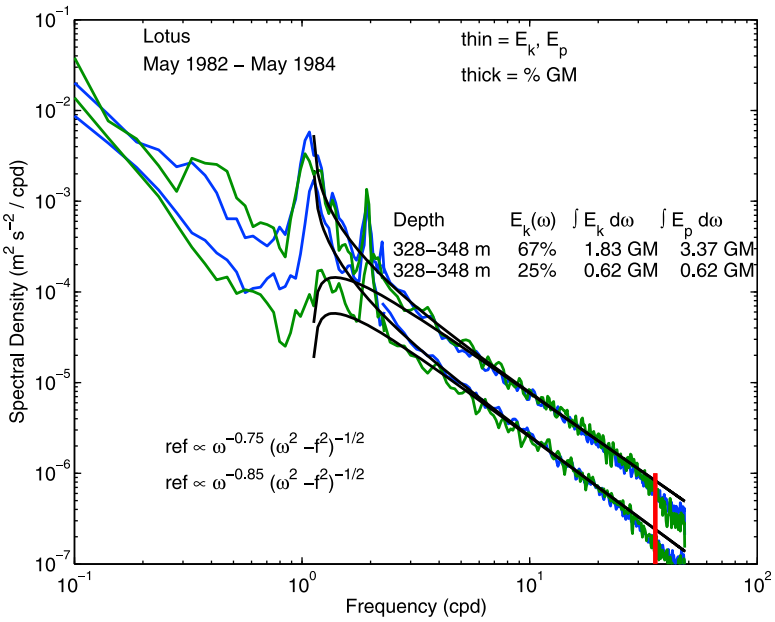

Figure 9. LOTUS frequency spectra of horizontal kinetic energy and potential energy (blue and green lines) for the high- and low-energy states depicted in Figure 8. Black curves represent fits of (21) with $r = 1.75$ and $r = 1.85$. The thick vertical line represents the buoyancy frequency cutoff. Temporal variability is dominated by variability in the overall amplitude of the spectra rather than the shape (power law).

stantially reduced from the LOTUS time series 500 km north (Figure 10). Frequency spectra (Figure 11) at depths of 556 and 631 m are defined by a power law σ^{-r} of $r = 1.85$ and amplitudes significantly smaller than the GM model.

[71] Vertical profiles of horizontal velocity and density were obtained during February–March using the high-resolution profiler (HRP) [*Polzin et al.*, 1996]. The vertical profiles, obtained primarily 1° north of the moored array as part of a spatial survey, revealed a complex pattern of variability associated with the frontal velocity structure in the upper 250 m. Here we report results concerning data from depths of 250–1000 m. Those data are fit with a spectrum having an asymptotic roll-off of $m^{-2.3}$ (Figure 12).

[72] *Weller et al.* [1991a] document a slight excess of clockwise phase rotation with depth over counterclockwise shear variance, a signature of excess downward propagating near-inertial energy. The quoted power law in the vertical wavenumber domain is at a depth for which N^2 varies by less than a factor of 2, so that biases associated with linear wave propagation in nonuniform N are likely small. The instrument does not, however, return robust velocity estimates at large vertical scales, and hence, diagnosing interactions with the thermocline-scale geostrophic shear is problematic.

3.3.3. The Western Tropical Atlantic: Salt Finger Tracer Release Experiment and PolyMode IIIc—$m^{-2.4}$ and $\sigma^{-1.9}$

[73] Extant frequency domain data from thermocline regions in the western tropical Atlantic are limited to those obtained as part of the PolyMode program. The motivation for PolyMode Array III was exploration of low-frequency variability in what were perceived as dynamically distinct regions of the North Atlantic. Cluster IIIc was placed in the eastward flowing North Equatorial Current with the intent of examining the low-frequency variability for characteristics of eddy generation by baroclinic instability [*Keffer*, 1983]. The cluster is situated over the northwestern extension of the Demerara Abyssal Plain. Locally, the bottom is well sedimented and relatively flat, though rough topography lies immediately to the east. Data presented here are an average of the three southeastern moorings (80, 81, and 82).

[74] Frequency spectra (Figure 13) roll off less steeply than σ^{-2}. The simple power law characterization (19) overestimates the observed spectral density at frequencies smaller than semidiurnal. An annual cycle in either high-frequency or internal wave band energy is not apparent in the time series (Figure 14).

[75] Vertical profile (HRP) data used here were obtained during November 2001 as part of a sampling survey for the Salt Finger Tracer Release Experiment. Warm, high-salinity Subtropical Underwater overlies cooler, fresher Antarctic Intermediate Water [*Schmitt et al.*, 2005]. The situation is unstable to the salt-fingering form of double diffusive instability, and a staircase layering of the temperature, salinity, and density profiles is present over much of the region. The profiles examined here were collected between (14°N–16°N, 50°W–57°W) on the northern edge of the survey region.

[76] Vertical wavenumber E_k spectra (Figure 15) roll off more steeply than m^{-2} at high wavenumber. The spectra are anomalous in that potential energy estimates exceed kinetic energy at high wavenumber, a pattern that we attribute to the staircase features. The parametric fit (18) produces a low-wavenumber roll-off equivalent to mode 14. Estimates of E_p dominate E_k at low wavenumber.

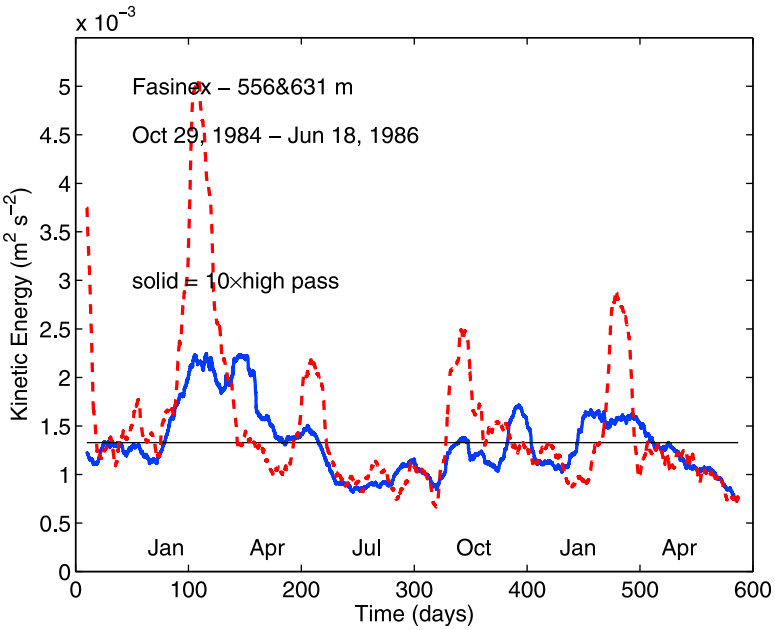

Figure 10. FASINEX time series of high-frequency energy from 556 and 631 m water depth. The solid line represents 10 times the high-frequency energy. The dashed line represents the entire internal wave band energy estimate.

3.3.4. The Southeast Subtropical North Atlantic: North Atlantic Tracer Release Experiment and Subduction—$m^{-2.55}$ or $m^{-2.75}$ and $\sigma^{-1.35}$

[77] Vertical profile (HRP) data were collected during April 1992 southwest of the Canary Islands as part of an initial site survey for the North Atlantic Tracer Release Experiment (NATRE). The bulk of the data were obtained as part of a 400 × 400 km grid centered about (26°N, 29°W). Apart from a minor seamount with a summit at 3000 m water depth, the bottom is relatively featureless near the survey domain. The region is further notable for the production of a relatively minor water mass, Madeira Mode Water [*Weller et al.*, 2004].

[78] A rotary decomposition of the vertical profile data does not return a consistent pattern of phase rotation with depth as a function of wavenumber. Thus, despite the fact that the buoyancy profile in the southeast part of the subtropical gyre decreases monotonically from the mixed layer base through the main thermocline, we consider a possible bias of the spectral slope associated with a purely linear response to wave propagation in variable $N(z)$ to be unlikely.

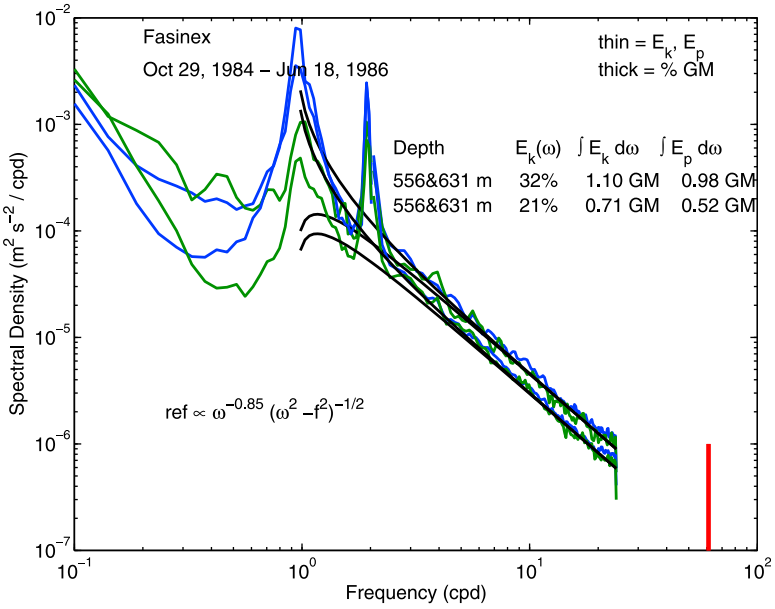

Figure 11. FASINEX frequency spectra (blue and green lines) of horizontal kinetic energy and potential energy from the main thermocline (600 m). Black curves represent fits of (21) with $r = 1.85$. The thick vertical line represents the buoyancy frequency cutoff.

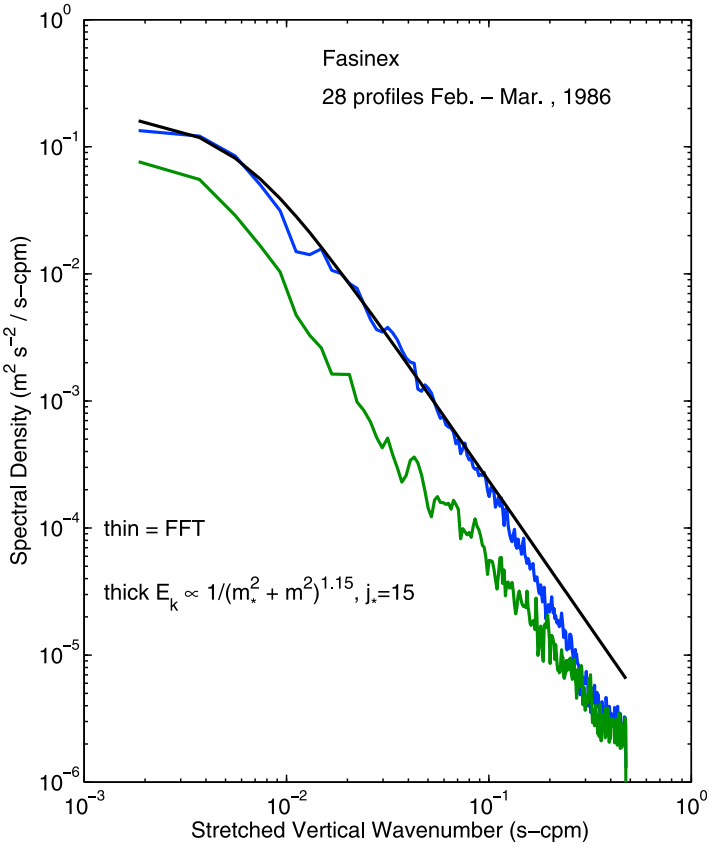

Figure 12. FASINEX vertical wavenumber spectra of horizontal kinetic (blue) and potential (green) energy, N scaled and stretched under the WKB approximation to N_o = 3 cph. The black line is a fit of $1/(m_*^2 + m^2)^{1.15}$. These data were obtained 100–200 km north of the FASINEX moored array. Sampling was intermittent in both space and time. Note that the low-wavenumber spectral estimates have typically smaller ratios of E_k and E_p.

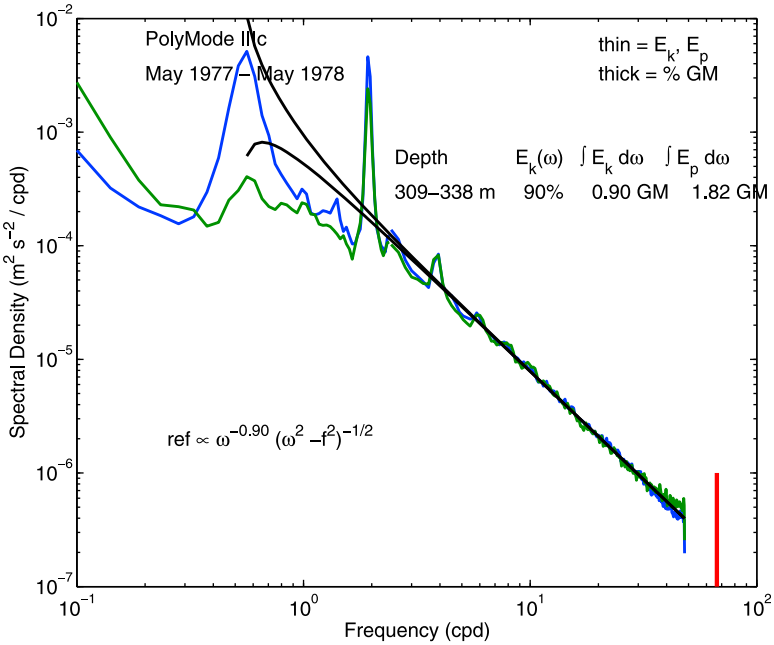

Figure 13. PolyMode IIIc frequency spectra (blue and green lines) of horizontal kinetic energy and potential energy from the main thermocline (300 m). Black curves represent fits of (21) with r = 1.90. The thick vertical line represents the buoyancy frequency cutoff.

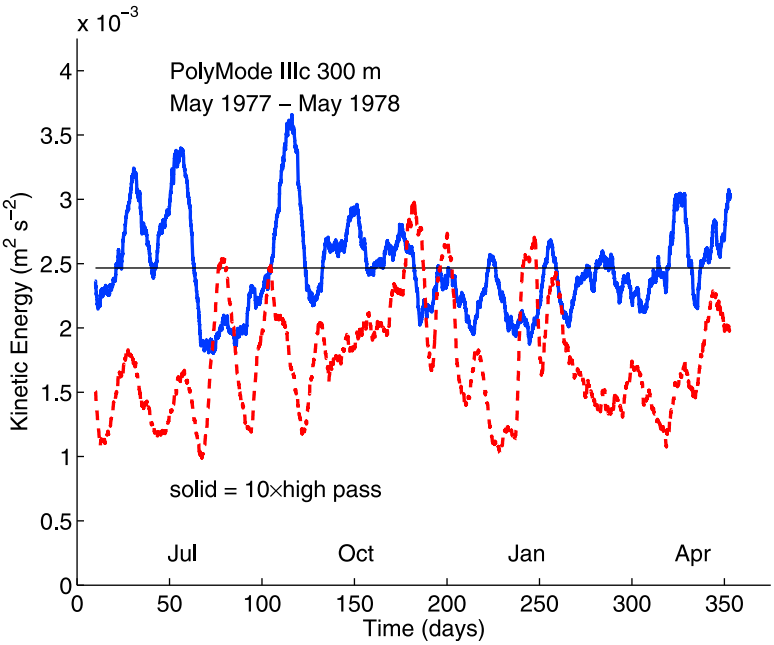

Figure 14. PolyMode IIIc time series of high-frequency and internal wave band energy from nominal 300 m water depth. The solid blue line represents 10 times the high-frequency energy. The dashed red line represents the entire internal wave band energy estimate.

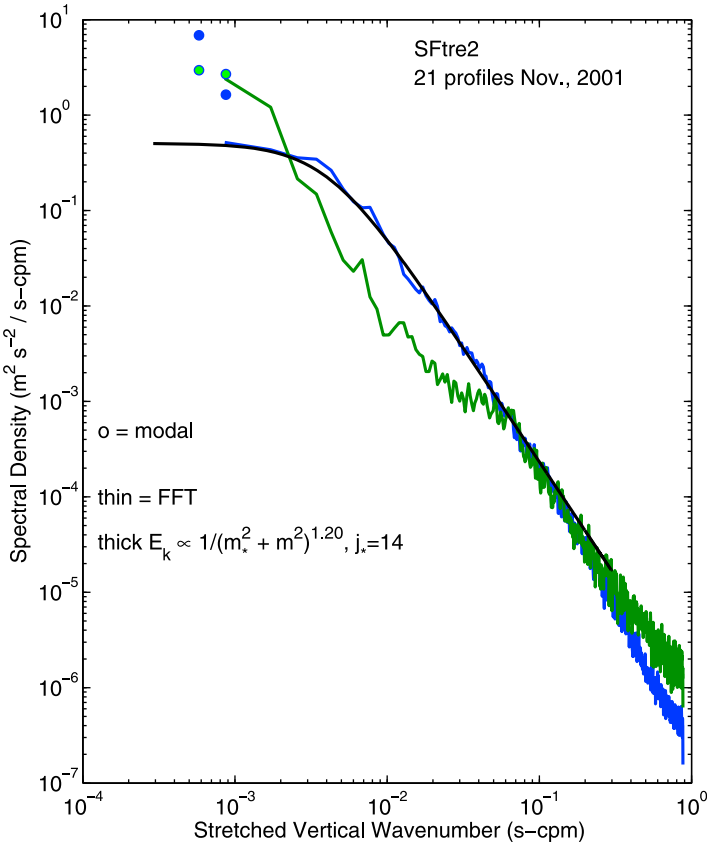

Figure 15. SFTRE2 vertical wavenumber spectra of horizontal kinetic (blue) and potential (green) energy, N scaled and stretched under the WKB approximation to N_o = 3 cph. The black line is a fit of $1/(m_*^2 + m^2)^{1.20}$. These data were obtained on the northern part of the year 1 sampling survey grid. Note that the low-wavenumber spectral estimates have typically smaller ratios of E_k and E_p.

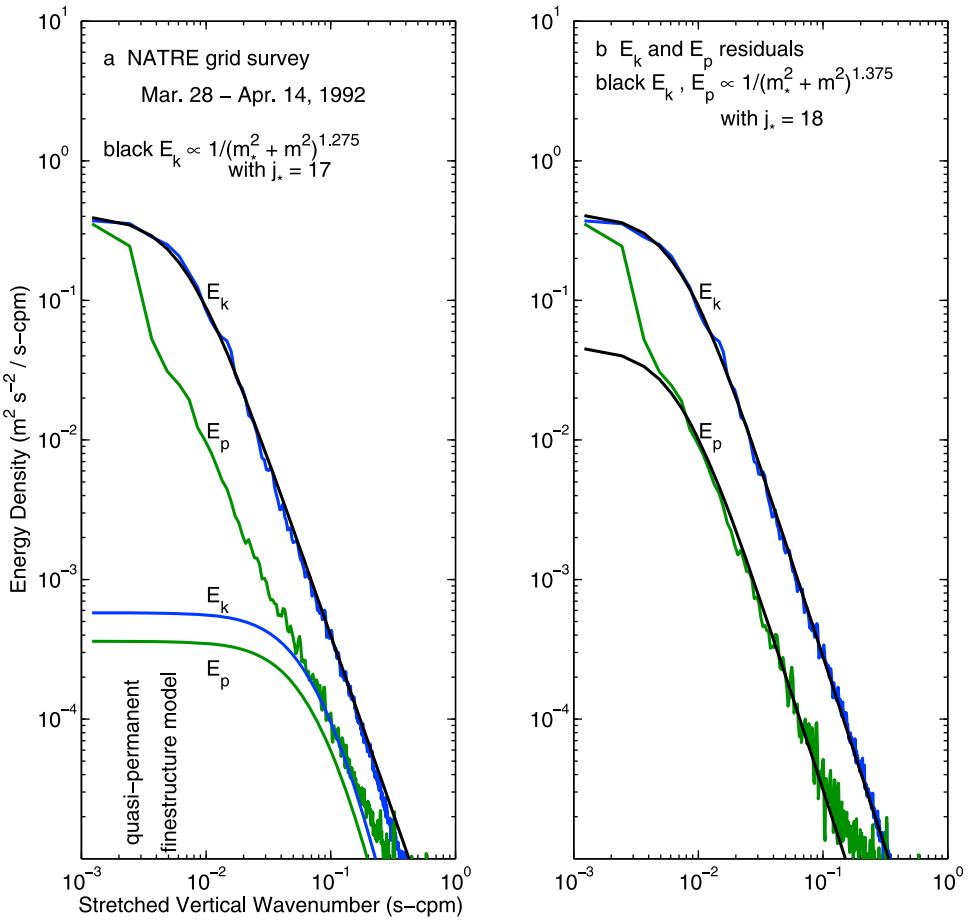

Figure 16. NATRE vertical wavenumber kinetic E_k and potential E_p energy spectra. These 100 profiles were obtained as part of a 400 × 400 km grid survey. (a) Observed vertical spectra, N scaled and stretched under the WKB approximation to N_o = 3 cph, and the quasi-permanent fine structure spectrum from *Polzin et al.* [2003]. (b) The internal wave spectra, observed minus quasi-permanent contributions. The black lines represent fits of $1/(m_*^2 + m^2)^{11/8}$ to the spectra, with m_* = 0.0070 cpm. The fit to the velocity data is obscured as it overlies the data. Note that the low-wavenumber spectral estimates have typically smaller ratios of E_k and E_p.

[79] The vertical wavenumber kinetic energy spectra (Figure 16) are white at low wavenumber and roll off more steeply than m^{-2} for vertical wavelengths smaller than 200 m ($E_k \propto m^{-2.55}$). The observed potential energy spectra exhibit three salient features in contrast with the kinetic energy spectrum. First, kinetic and potential energy are nearly equal at the largest resolved vertical wavelengths, about 1000 m. The spatial survey is of sufficient lateral extent that even though low-frequency variability is dominated by barotropic and low-mode (mode 1 and mode 2) contributions [*Wunsch*, 1997], low-frequency variability may contribute to the observed spectra at the largest resolved scales (equivalent to about mode 3 in Figure 16). Analysis of a subset of these data obtained on a grid with 1 nautical mile spacing returns a consistent signature: E_k/E_p ratios of 2–3 are found at the lowest two resolved vertical wavelengths. Second, the spectra diverge so that E_k is about an order of magnitude larger than E_p at 100 m vertical wavelengths. Third, E_p does not roll off as quickly at high wavenumber, as can be inferred from increasing ratios between E_p and E_k at vertical wavelengths smaller than 10 m. *Polzin et al.* [2003] argue that these increasing ratios at small scales are largely associated with an increasing contribution of quasi-permanent fine structure (section 2.1.4). When the quasi-permanent contribution is subtracted from the observations, both E_k and E_p roll off at about the same rate, $E_k \propto E_p \propto m^{-2.75}$. The low-wavenumber excess of E_p remains. The vertical wavenumber spectrum indicates a nonseparable spectrum, with excess near-inertial content at high wavenumber.

[80] The vertical profile data were obtained from the vicinity of the center mooring of the Subduction array [*Weller et al.*, 2004]. VMCMs deployed on surface moorings document obvious inertial and tidal peaks and peaks at several harmonics (Figure 17). The frequency spectrum is not succinctly characterized in terms of a single power law. At low frequencies ($1 < \sigma < 6$ cpd) the spectrum exhibits a plateau (ignoring the tidal peak and harmonics), and at higher frequencies ($6 < \sigma < 48$ cpd) it rolls off as $\sigma^{-1.35}$. Energy ratios ($E_k(\sigma)/E_p(\sigma)$) agree with linear kinematics (9). Internal wave band ratios ($\int E_k(\sigma)\, d\sigma / \int E_p(\sigma) d\sigma$) are between 2 and 3, consistent with a red vertical wavenumber spectrum having

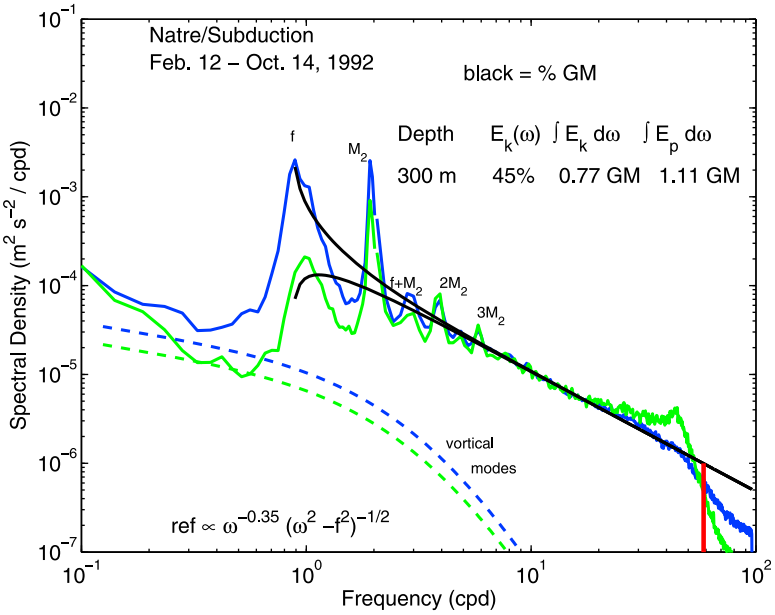

Figure 17. NATRE frequency spectra (blue and green lines) of horizontal kinetic energy and potential energy from the main thermocline (300 m). Observed spectra (solid lines) with vortical mode spectra (dashed lines) superimposed. The nonpropagating vortical fluctuations are assumed to be passively advected by the mesoscale field in this representation. See *Polzin et al.* [2003]. Inertial, semidiurnal, and harmonic peaks are noted. Black curves represent fits of (21) with $r = 1.35$. The thick vertical line represents the buoyancy frequency cutoff.

little near-inertial content at low wavenumber. Unlike the Sargasso Sea, no seasonal cycle is apparent in either internal wave energy time series (Figure 18).

[81] NATRE is special among these data sets in that it exhibits a strikingly large M_2 tide and the region is a relative minimum in eddy energy [*Wunsch*, 1997]. An obvious hypothesis is that structure in the spectral domain reflects the detailed pathway energy takes in draining out of the tidal peak. A second hypothesis is suggested by noting that the transition between the two regimes (roughly 6 cpd) corresponds to the stratification rate near the bottom boundary ($N \simeq 3$ cpd). Waves of higher frequency never reach the bottom and will not be attenuated by viscous processes in the bottom boundary layer.

3.3.5. The Southeast Subtropical North Pacific

[82] A significant number of data sets have been obtained offshore southern California. The major geographic feature here is the California Current System, consisting of a deep poleward flow along the continental slope, equatorward flow at the shelf break, and a 600 km wide band of mesoscale variability extending from the shelf and fading into the northeast Pacific [e.g., *Chereskin et al.*, 2000]. There are, as well, gradients in mesoscale variability along the coast, with the most northern of the data sets discussed here being closest to a regional maximum in surface kinetic energy estimated from surface drifter data [*Chereskin et al.*, 2000]. The data discussed here are more than 400 km distance from the shelf break. The buoyancy frequency ($N(z)$) typically attains a maximum at 100 m water depth and decreases by about a factor of 3 over 300 m. This represents a large gradient.

[83] Data from this region include the oscillating float estimates of isopycnal displacement providing frequency spectra and vertical lag coherence estimates reported by *Cairns* [1975] and *Cairns and Williams* [1976]. These data prompted the revision of GM75 model to the GM76 form. See section 2.3 for further discussion.

[84] Here we utilize moored current meter data from the Eastern Boundary Currents (EBC) program and vertical profile data from the Patches Experiment (PATCHEX) [*Sherman and Pinkel*, 1991] and the Surface Wave Process Program (SWAPP) [*Weller et al.*, 1991b]. PATCHEX was a multi-investigator study of the space and time structure of mixing events. SWAPP was nominally focused upon upper ocean processes, but data were obtained from thermocline regions as well. These latter two field programs featured yo-yo CTD and Doppler sonar data sets obtained from the research platform *Floating Instrument Platform* (R/P *FLIP*). These simultaneous vertical profiles of velocity and density provide a unique representation of the upper ocean wavefield and permit 2-D vertical wavenumber-frequency spectra to be evaluated. This has been done in both depth and density coordinates, with the latter being consistent with and directly comparable to the theoretical analysis presented in the companion piece [*Lvov et al.*, 2010]. The use of this coordinate system will also likely limit contamination by quasi-permanent density fine structure. Quantifying this is difficult, as is quantifying the effects of Doppler shifting by subinertial currents. Results from the density data are used exclusively here as the velocity data are subject to contamination from instrumental noise and beam separation effects at high wavenumber and frequency (section B2). A

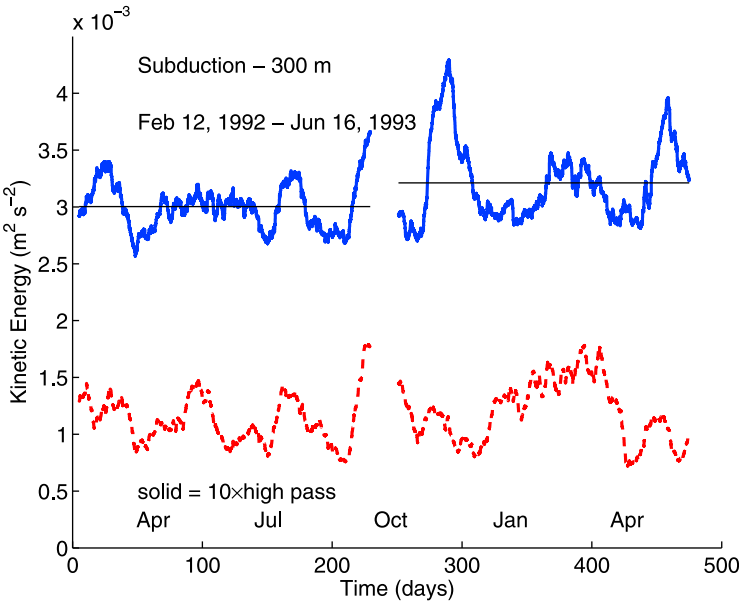

Figure 18. NATRE time series of high-frequency and internal wave band energy from nominal 300 m water depth. The solid blue line represents 10 times the high-frequency energy. The dashed red line represents the entire internal wave band energy estimate.

further cautionary note is that sampling during PATCHEX may not have been of sufficient temporal or spatial extent for the observations to reflect the background wavefield.

3.3.5.1. Eastern Boundary Currents: σ^{-2}

[85] A coherent moored current meter array was deployed for a 2 year period (1992–1994) at the offshore edge of the California Current as part of the Eastern Boundary Currents field program [*Chereskin et al.*, 2000]. These data represent the only available long-term current meter records in the vicinity of the other data from the northeast Pacific discussed herein. As those data are from short-term (several week) field programs, it is a natural question to ask whether those data are representative of the long-term average (Figure 19). The data (both short and long term) share a common frequency dependence of σ^{-2} at high frequency. Variability of both high-passed and wave band energy levels is associated with eddy variability rather than a seasonal cycle (Figure 20).

3.3.5.2. PATCHEX[1]: $m^{-1.9}$

[86] Data from a freely falling vertical multiscale profiler were obtained during PATCHEX. *Gregg* [1988] notes that the velocity profile data are remarkable only for the absence

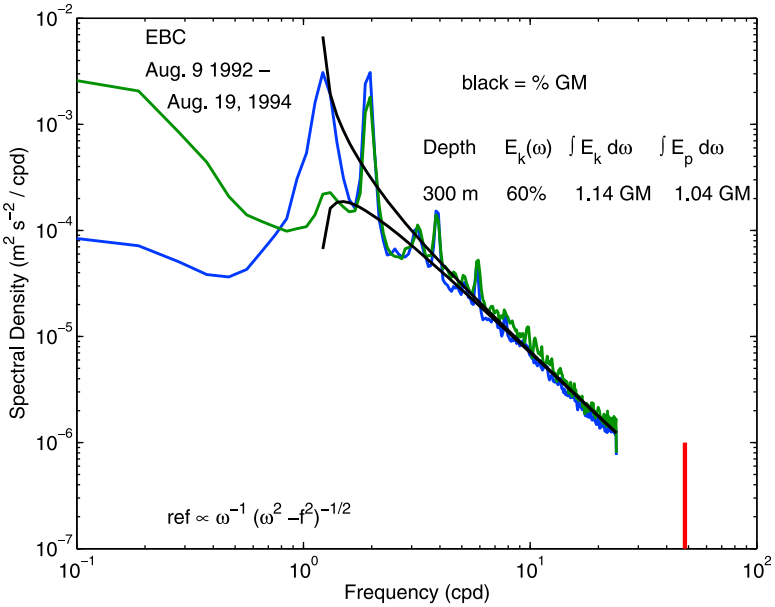

Figure 19. Eastern Boundary Currents frequency spectra (blue and green lines) of horizontal kinetic energy and potential energy from the main thermocline (600 m). Black curves represent fits of (21) with $r = 2.00$. The thick vertical line represents the buoyancy frequency cutoff.

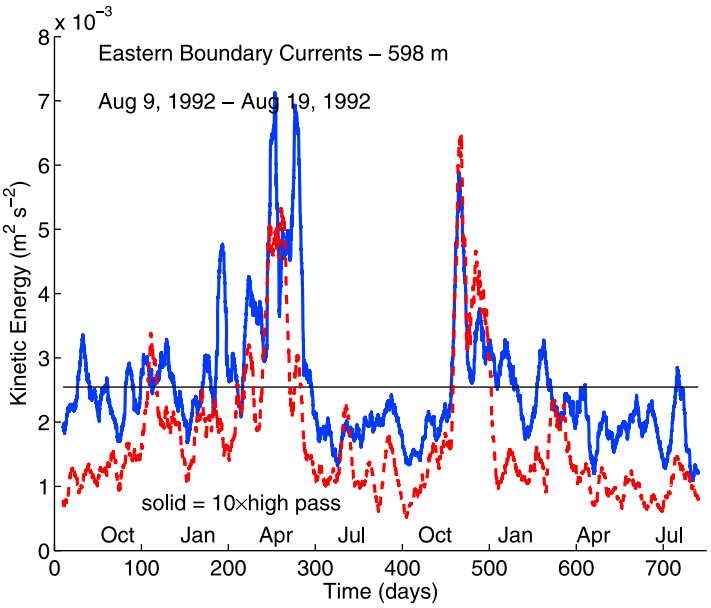

Figure 20. Eastern Boundary Currents time series of high-frequency and internal wave band energy from nominal 600 m water depth. The solid blue line represents 10 times the high-frequency energy. The dashed red line represents the entire internal wave band energy estimate. Peaks in high-frequency and wave band energy during April and November 1993 coincide with the presence of anticyclonic eddies [*Chereskin et al.*, 2000].

of coherent near-inertial wave packets. *Gregg et al.* [1993a] document a shear spectrum that varies from white at pressures of 250–550 db to slightly blue (575–925 db) over vertical wavelengths of 10–100 m (Figure 21).

3.3.5.3. PATCHEX[2]: $m^{-1.75}$ and $\sigma^{-1.65}$–$\sigma^{-2.0}$

[87] During PATCHEX two CTD profilers were deployed from the R/P *FLIP* to obtain density profiles over 0–560 m water depth, with a cycle time of 180 s. The density data considered here come from the depth interval 150–406 m. No information regarding vertical symmetry or mean currents is available.

[88] For vertical wavenumber $1/256 < m < 1/10$ cpm, the density gradient spectrum rolls off as $m^{-1.75}$ over $0.125 < \sigma < 1.4$ cph (Figure 22). This range of wavenumbers and frequencies is characterized by a frequency dependence of $\sigma^{-1.65}$–σ^{-2}. The cumulative spectrum (integrated over all frequencies $f \leq \sigma \leq N$) is slightly blue for $0.02 < m < 0.1$ cpm. These power law relations were determined graphically with use of a straight edge.

3.3.5.4. SWAPP: $m^{-1.9}$ and $\sigma^{-2.0}$

[89] During SWAPP a pair of CTD profilers deployed from *FLIP* returned density profiles from 5 to 420 m with a vertical resolution of about 1.5 m and cycle time of 130 s for a duration of 12 days during March 1990. The data cited here come from depths of 50–306 m.

[90] For vertical wavenumbers $1/128 < m < 1/10$ cpm, the density gradient spectrum rolls off as σ^{-2} over $0.2 < \sigma < 4$ cph (Figure 23). For frequencies of $0.02 < \sigma < 2$ cph, the vertical wavenumber spectrum is nearly white, $m^{0.1}$, so that the energy spectrum rolls off as $m^{-1.9}$ (Figure 24). As with the PATCHEX data from *FLIP*, these power law relations have simply been determined using a χ-by-eye procedure.

[91] The buoyancy frequency ($N(z)$) attains a maximum at 100 m water depth and decreases by about a factor of 3 over 300 m. At periods greater than 8 h, the shear spectra indicate a dominance of downward energy propagation [*Anderson*, 1992]. Thus, the vertical spectrum may be influenced by purely linear kinematics, rather than nonlinearity. The shear spectrum is not easily characterized. It exhibits a peak at about 0.03 cpm associated with downward propagating near-inertial waves [*Anderson*, 1992].

3.3.6. The Northeast Subpolar North Pacific

3.3.6.1. Midocean Acoustic Transmission Experiment: $m^{-2.1}$ and $\sigma^{-1.7}$

[92] An extensive set of moored and profiling (both vertical and horizontal) observations was taken during June–July 1977 as part of the Midocean Acoustic Transmission Experiment (MATE) [*Levine et al.*, 1986]. The experiment was located at 46°46′N, 130°47′W, midway between Cobb seamount, which rises to within 30 m of the surface, and the smaller Corn seamount, which rises to depths of 1000 m. The seamounts are separated by approximately 18 km, and the local water depth is 2200 m. The seamounts may serve as significant generators of an internal tide. Cobb seamount has been noted to support a trapped diurnal tide [*Codiga and Eriksen*, 1997; *Lueck and Mudge*, 1997]. The MATE observations focused upon subthermocline depths of 900–1300 m away from the seamounts.

[93] Current meter data document frequency domain power laws of $\sigma^{-1.7}$ (Figures 25 and 26). Temperature profiles from a Bissett-Berman 9040-5 CTD sound velocity measuring instrument were used along with a locally tight $\theta - S$ relation to estimate vertical displacement. Vertical wavenumber domain power laws of $m^{-2.1}$ are quoted for

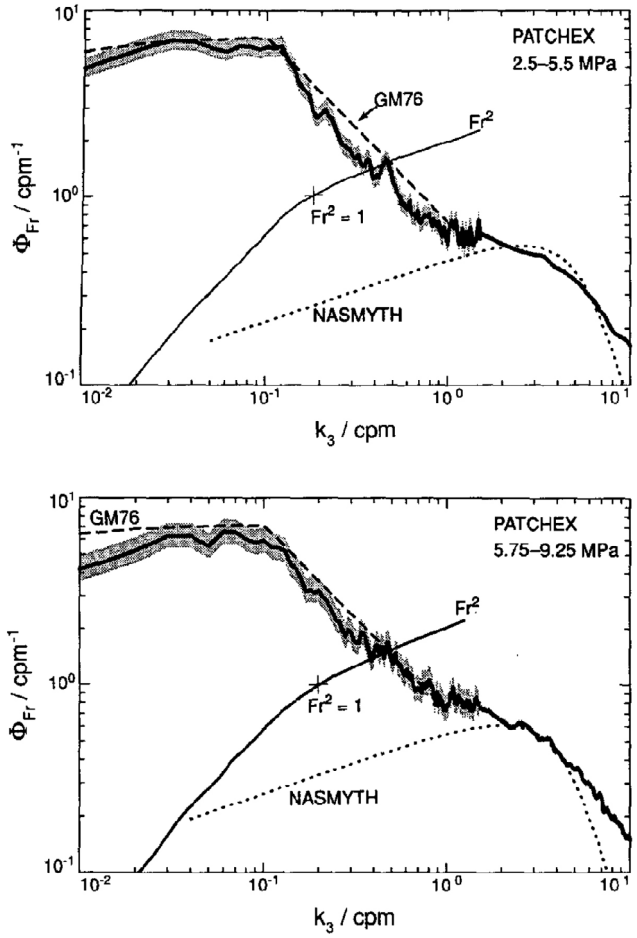

Figure 21. PATCHEX vertical wavenumber shear spectra using the free-fall multiscale profiler. The dashed line represents $m^2/(m_*^2 + m^2)$, with $j_* = 3$ and an m^{-1} dependence at vertical wavelengths smaller than 0.1 cpm. The domain of interest here is $0.01 < m < 0.1$ cpm [from *Gregg et al.*, 1993a, Figure 6].

$6 \times 10^{-3} < m < 6 \times 10^{-2}$ cpm (Figure 27). Horizontal wavenumber spectra of vertical displacement (again estimated from temperature) obtained from the Self-Propelled Underwater Research Vehicle roll off as $|k|^{-2}$ for horizontal wavenumbers $4.7 \times 10^{-4} < |k| < 9.0 \times 10^{-3}$ cpm (Figure 28). A combined analysis of spatial lag coherences returns a roll-off of $j_* = 6$.

3.3.6.2. Storm Transfer and Response Experiment and Ocean Storms: $m^{-2.3}$ and $\sigma^{-2.2}$

[94] The northeast subpolar North Pacific has been the subject of a number of experiments focusing on near-inertial internal wave generation and mixed layer processes. The experiments (vertical profile data from the Storm Transfer and Response Experiment [*D'Asaro*, 1984] taken during November 1980 at 141°W, 50°N, and current meter data from the Ocean Storms Experiment [*D'Asaro*, 1995a] at 139.25°W, 47.5°N, are examined here) are located just south of the climatological storm track in order to emphasize the coupling between inertial motions in the mixed layer and an inertial time scale anticyclonic rotation of the wind stress vector associated with small-scale atmospheric disturbances. The region is also one of relatively low eddy energy and so minimizes the confounding effect of mesoscale eddy–internal wave interactions.

[95] Current meter data from 200 m water depth from the Ocean Storms Experiment clearly documents the input of near-inertial internal wave energy associated with the passage of individual storms (Figure 29). The presence of a seasonal cycle in inertial energy, though, is obvious only at greater depths (500 m). In a broad survey of historical current meters, *Alford and Whitmont* [2007] find that the seasonal cycle in near-inertial energy is most evident at latitudes of 25°–45°, with decreasing seasonal modulations north of 45°. A possible interpretation is a regional emphasis on propagation.

[96] High-frequency energy at 500 m also exhibits a seasonal cycle. Unlike seasonal cycles in the western North Atlantic, here the high-frequency energy appears to lag near-inertial energy by several tens of days. A possible interpretation is that the presence of such a phase lag is related to the absence of an energetic eddy field.

[97] The frequency spectrum fit indicates a spectrum redder than GM (Figure 30). This is paired with a vertical wavenumber spectrum of horizontal velocity also steeper than GM (Figure 31). This represents the sole example of power laws that do not covary.

3.3.7. The Arctic: Arctic Internal Wave Experiment—$m^{-2.25}$ and $\sigma^{-1.2}$

[98] The Arctic Internal Wave Experiment (AIWEX) was conceived as an attempt to study an anomalous internal wavefield. The experiment took place about 350 km north of Prudhoe Bay, Alaska, with sampling extending from March to May 1985. Total energy was a factor of 0.02 to 0.07 times smaller than in the GM model spectrum. Possible reasons for the lower energy are weaker winds and wind stress, the presence of ice cover, a small barotropic tide, and a weak circulation on basin scales [*Levine et al.*, 1987]. Peaks at the M_2 tidal frequency and its harmonics are not apparent. There was no discernible kinetic energy dissipation rate associated with the wavefield [*Padman and Dillon*, 1987], consistent with low levels of energy and shear.

[99] The frequency spectra for both temperature and velocity were much whiter than typical [*Levine et al.*, 1987]. For frequencies much larger than f, the power law σ^{-r} tends to $r = 1.2$ [*Levine*, 1990] (Figure 32).

[100] Velocity profiles were obtained with expendable current profilers (XCPs). These data suggest a vertical wavenumber bandwidth about 10 times larger than in the GM model [*D'Asaro and Morehead*, 1991] (Figure 33).

[101] Several notes of caution are in order. First, the data were not taken as a random sample relative to the eddy field. The Canadian Basin is populated by relatively intense submesoscale vortices, and the AIWEX XCP survey was intentionally taken between such features. It is not clear whether this leaves the data set prone to straining effects as are evident in the MODE data set. Second, *D'Asaro and Morehead* [1991] argue for the presence of quasi-permanent velocity fine structure at 40 m vertical wavelength with relatively

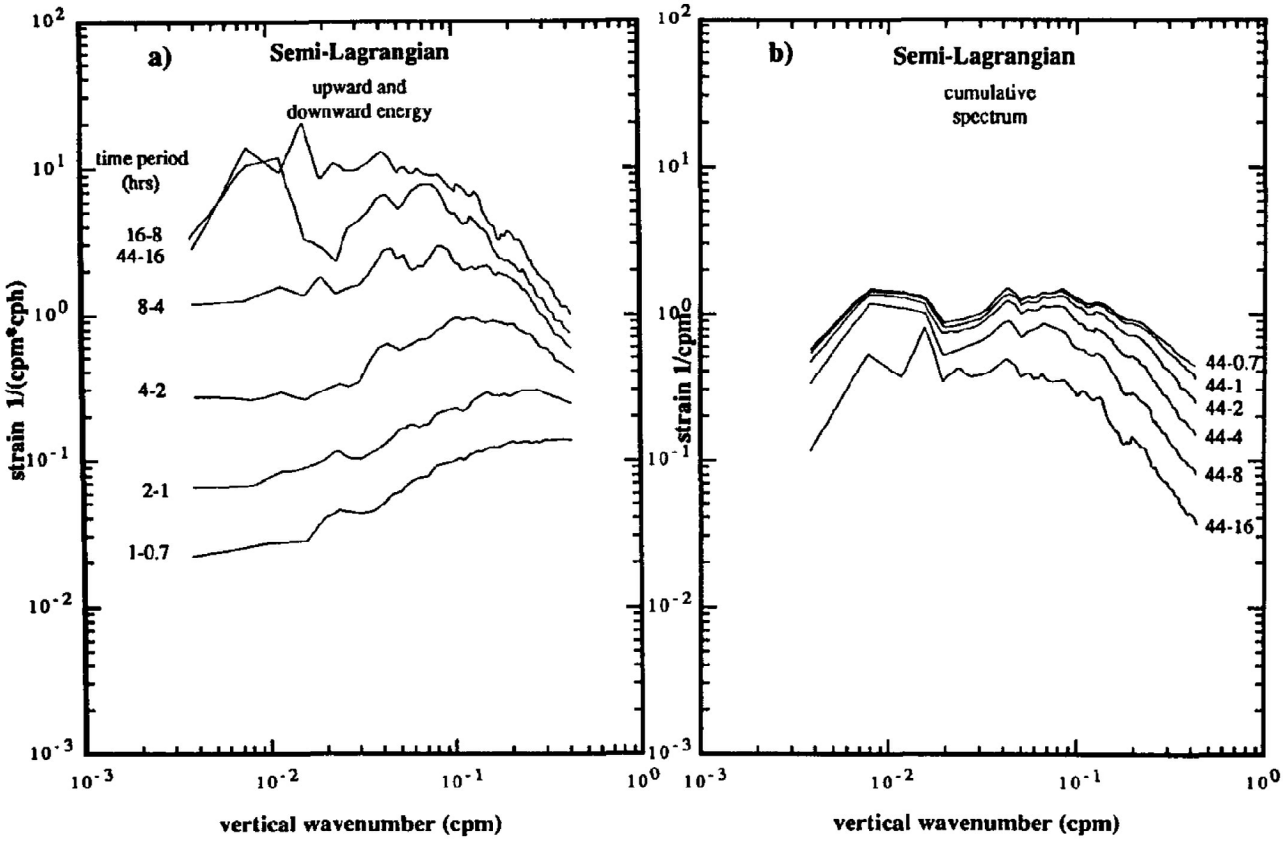

Figure 22. PATCHEX 2-D vertical wavenumber-frequency spectra of isopycnal displacement gradient. The density data from which displacement is estimated were obtained with a rapid-profiling CTD profiler from the research platform *FLIP*. The quoted power law dependencies have been determined graphically [from *Sherman and Pinkel*, 1991, Figure 6].

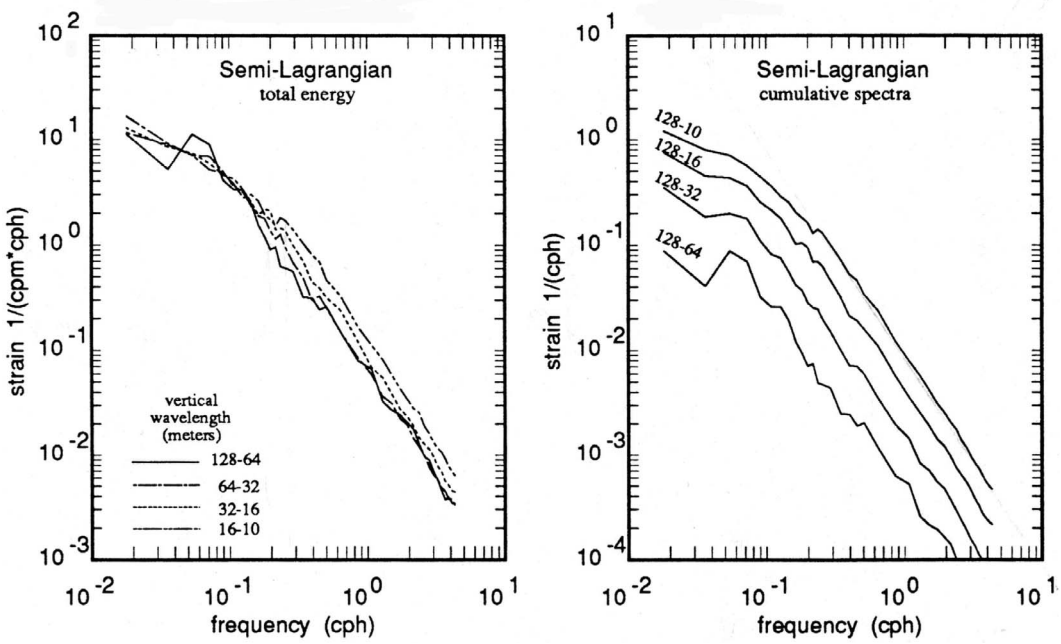

Figure 23. SWAPP frequency spectra of isopycnal displacement gradients. The density data from which displacements are estimated were obtained with a rapid-profiling CTD profiler from the research platform *FLIP*. The quoted power law dependencies have been determined graphically (from *Anderson* [1992, Figure 2.9], with permission from S. Anderson, copyright 1992).

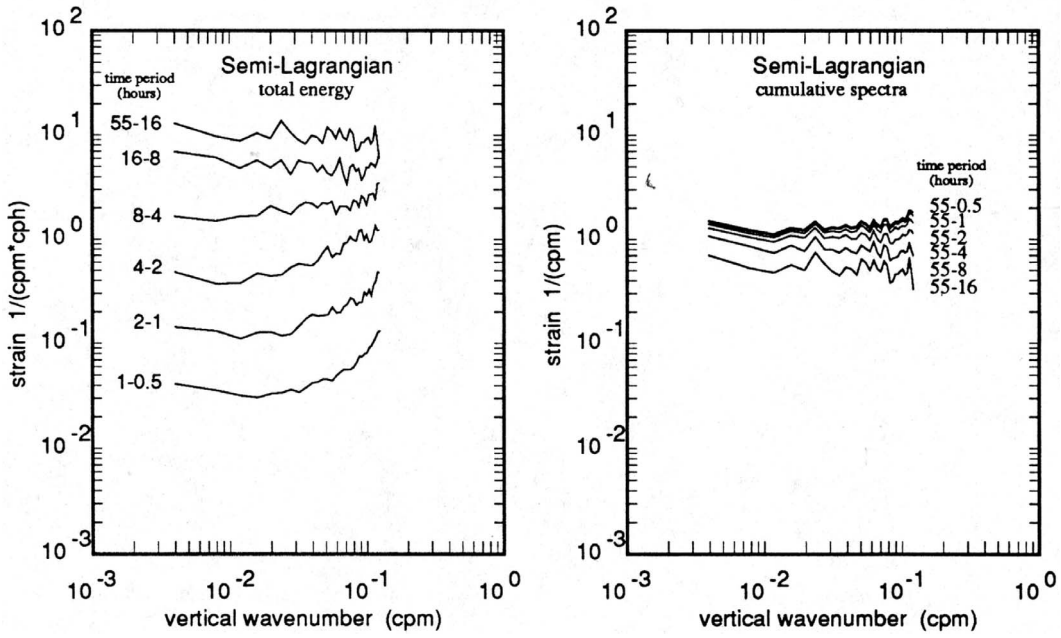

Figure 24. SWAPP vertical wavenumber spectra of isopycnal displacement gradients. The density data from which displacement is estimated were obtained with a rapid-profiling CTD profiler from the research platform *FLIP*. The quoted power law dependencies have been determined graphically (from *Anderson* [1992, Figure 2.7], with permission from S. Anderson, copyright 1992).

small levels of quasi-permanent density fine structure. Their diagnostics, though, depend upon being able to account for all noise in the XCP measurements. Their noise budget does not include noise induced by fall rate variations of the XCP [*Sanford et al.*, 1993], which shows up as noise in the north-south velocity component at 15–30 m vertical wavelength.

[102] Finally, the spectral levels are so small that one might call into question whether nonlinearity is important in shaping the spectrum. Boundary dissipation has been cited as a dominant decay process rather than interior wave breaking [*Pinkel*, 2005].

4. SUMMARY

[103] Despite the fact that major deviations in the model parameters have been noted near boundaries [*Wunsch and Webb*, 1979] and near the equator [*Eriksen*, 1985a], it is

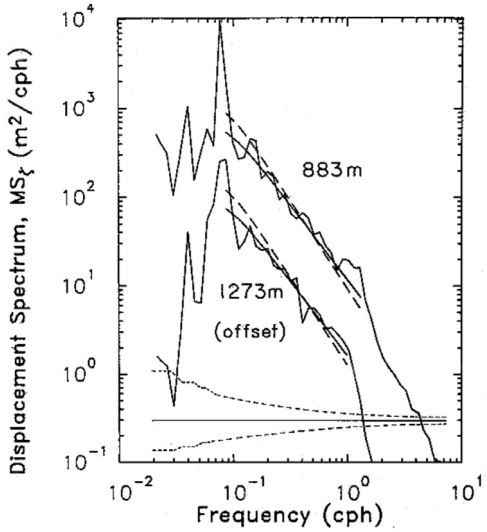

Figure 25. MATE frequency spectra of vertical displacement. Solid and dashed curves are the MATE and GM models, respectively [from *Levine et al.*, 1986, Figure 5].

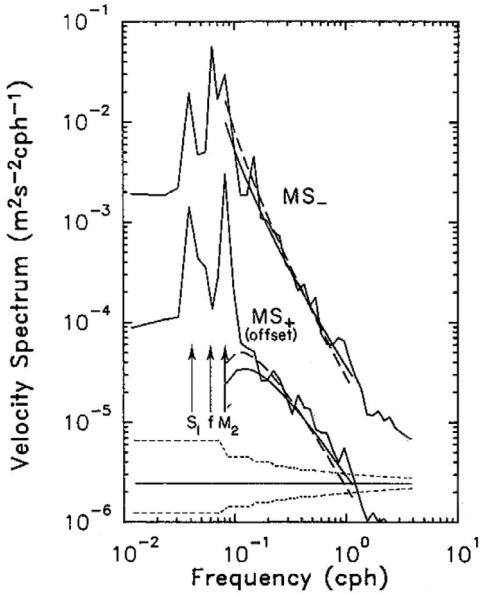

Figure 26. MATE frequency spectra of horizontal kinetic energy. Solid and dashed curves are the MATE and GM models, respectively [from *Levine et al.*, 1986, Figure 8].

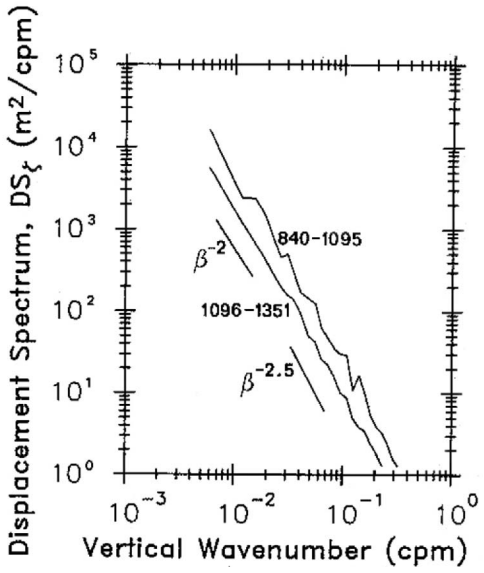

Figure 27. MATE vertical wavenumber spectra of vertical displacement [from *Levine et al.*, 1986, Figure 4].

astonishing that the characteristic shape, and after buoyancy scaling, level, are noted to be nearly universal in the literature. Variability in the spectral characteristics of the deep ocean internal wavefield is apparent. That variability, though, tends to be subtle.

[104] A number of patterns emerge from our analysis:

[105] 1. The variability of spectral shape is geographically related, rather than a function of spectral level. Measurements from Site D exhibit characteristics similar to those from the eastern subtropical North Pacific and have power laws in good agreement with the GM76 model. Both are eddy-rich regions. Observations from the eastern North Atlantic and the Arctic differ most significantly from the GM model. These regions have anomalously weak eddy fields, and the internal wave spectral levels are lower. Spectral shapes from the Sargasso Sea and the eastern boundary of the subpolar North Pacific are intermediate in character.

[106] 2. A seasonal cycle, most prominent in high-frequency energy, is apparent in the western subtropical North Atlantic. A seasonal cycle is also apparent in the eastern subpolar North Pacific. Their character, though, differs. The high-frequency signal in the North Pacific lags the near-inertial cycle, while near-inertial and high-frequency seasonal variability are in phase in the North Atlantic. The eddy fields in the two regions are distinctly different.

[107] 3. In terms of amplitude, the GM spectral model has an energy of $E_o = 30$ cm^2 s^{-2}. With the stipulated frequency distribution (21), this tends to overestimate observed frequency spectra from the deep ocean for $\sigma \gg f$. This pattern is evident in the works by *Wunsch and Webb* [1979, Table 1], *Fu* [1981, Table 3], and *Nowlin et al.* [1986, Table 1]. Despite this overestimate, the total energy in the internal wave band agrees much better with E_o. The difference is additional energy in the tides and at near-inertial frequencies.

[108] 4. The observed deep ocean internal wavefield is not, in general, separable. When available, vertical wavenumber spectra of potential energy tend to have larger characteristic vertical scales than vertical wavenumber spectra of kinetic energy. Fits to the kinetic energy spectra produce roll-offs ranging from $3 < j_* < 15$–20, with lower-amplitude frequency spectra being characterized by larger values of j_*. Fits to the potential energy spectra produce $j_* = 1$–2. Nonseparability is in the sense of a high wavenumber near-inertial addition to a separable spectrum. Indications of this are also apparent in the IWEX spectrum. The issue of separability appears to have been considered only in the continuum limit ($f \ll \sigma \ll N$) by *Garrett and Munk* [1972].

[109] 5. Frequency spectra with power laws whiter than the GM76 model (σ^{-2}) tend to have vertical wavenumber power laws that are redder than the GM76 model (m^{-2}).

[110] 6. Many of the frequency spectra show a departure from the smooth spectral models at frequencies between 1.5 f and 4–5 cph (e.g., Figure 13). Apart from tides, tidal harmonics, and combinations of tidal and inertial frequencies, the observed spectra tend to be at somewhat lower levels than the model fits in this frequency band. *Levine* [2002] notes a similar pattern and suggests that it is linked to internal wave dynamics at frequencies less than semidiurnal.

[111] 7. A recurring pattern is one of the near-inertial field having a larger vertical wavenumber bandwidth than the rest of the internal wavefield. Data sets were selected on the basis that they represent open ocean conditions and are not in the near field of sites associated with topographic generation

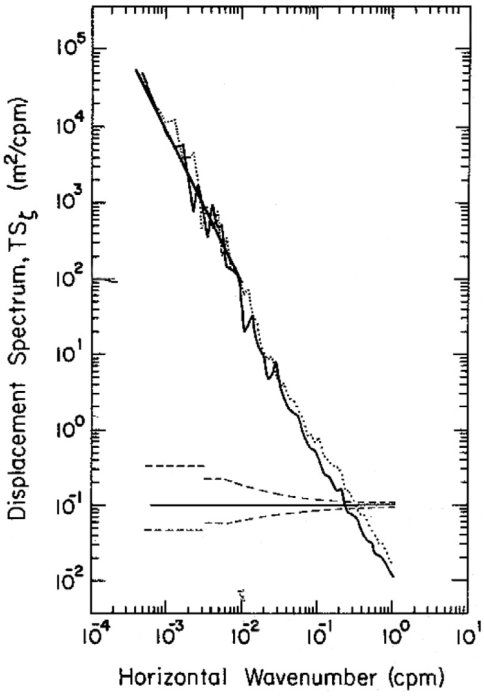

Figure 28. MATE horizontal wavenumber spectra of vertical displacement estimated from SPRUV. Solid and dashed curves represents north-south and west-east runs, respectively [from *Levine et al.*, 1986, Figure 9].

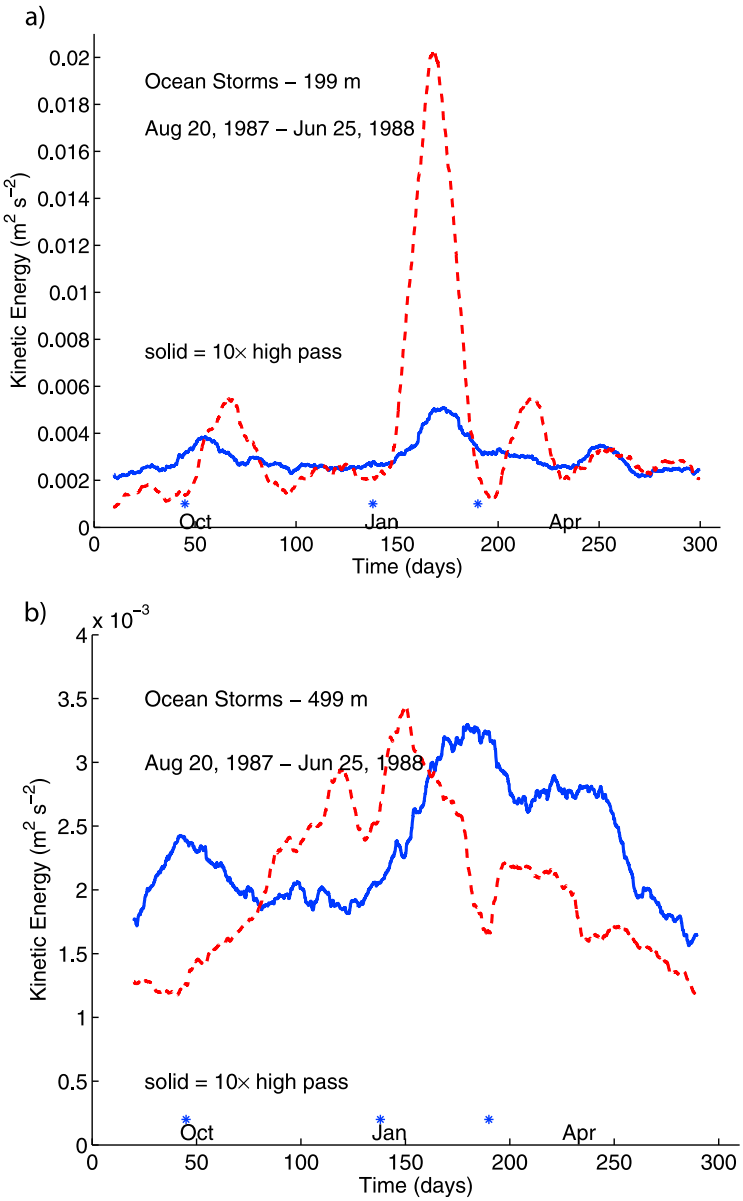

Figure 29. Ocean Storms time series of high-frequency and internal wave band energy from nominal depths of (a) 200 and (b) 500 m water depth. The solid blue line represents 10 times the high-frequency energy. The dashed red line represents the entire internal wave band energy estimate. The passage of storms resulting in strong forcing of mixed layer inertial currents is denoted by asterisks.

processes. We have consequently sought to relate the near-inertial bandwidth to interior processes. An unsettling possibility is that topographic influences may not be appreciated.

[112] The GM76 model is a reasonable description of the wintertime internal wave spectrum at Site D. The representativeness of the GM model for the background state here is not surprising as the GM frequency spectrum is no more and no less than a curve fit to data from Site D. But what may not be appreciated is that those original data were obtained during the dead of winter. At other times and in other places, differences between this model and observations are quite apparent.

[113] Departures from the GM model represent clues about the relative importance of the various possible sources and how those source inputs are modified by dissipation and wave-wave and wave mean interactions. How those clues can be brought together is discussed in section 5.

5. SPECTRAL BALANCES AND RADIATION BALANCE EQUATIONS

[114] In section 4 we documented variability in the background internal wave spectrum. Our hypothesis is that such background states are in near equilibrium between forcing, dissipation, and energy transfers. In this section we review what we perceive to be the key elements underlying such a hypothesis. We do not attempt an exhaustive review nor do we intend to elevate any result beyond the status of plausibility. As a prelude to that discussion, we present a 35 year

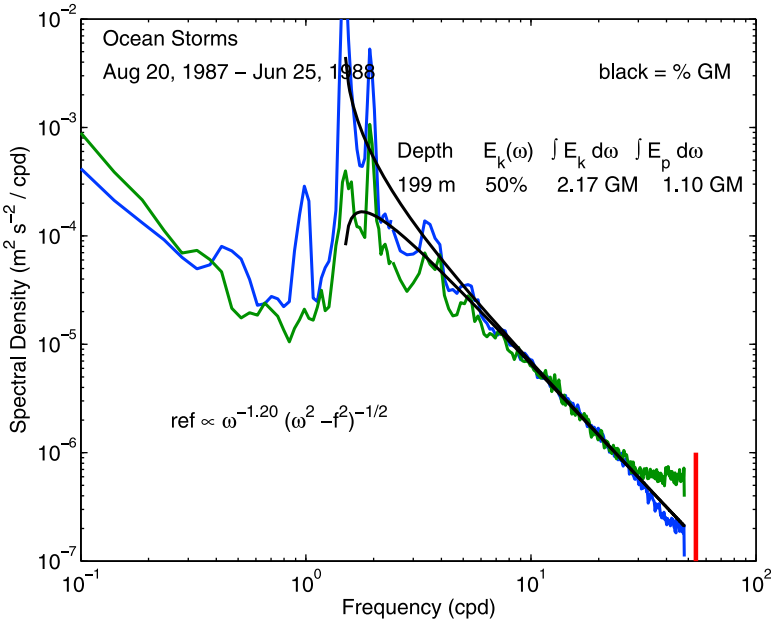

Figure 30. Ocean Storms frequency spectra (blue and green lines) of horizontal kinetic energy and potential energy from the main thermocline (200 m). Black curves represent fits of (21) with $r = 2.20$. The thick vertical line represents the buoyancy frequency cutoff.

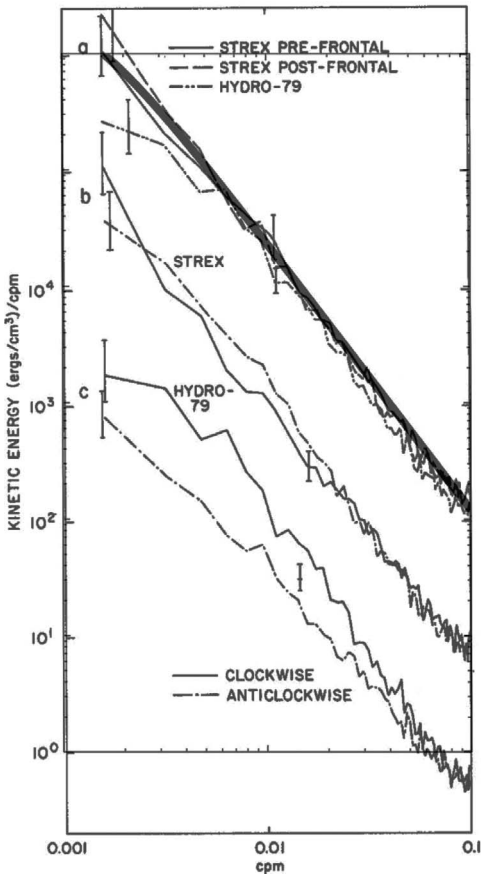

Figure 31. Storm Transfer and Response Experiment (STREX) vertical wavenumber kinetic E_k. The overlay represents a fit of $1/(m_*^2 + m^2)^{1.15}$ to the prefrontal spectra, with $m_* = 0.0070$ cpm (equivalent to $j_* = 3$) [from *D'Asaro*, 1984, Figure 4].

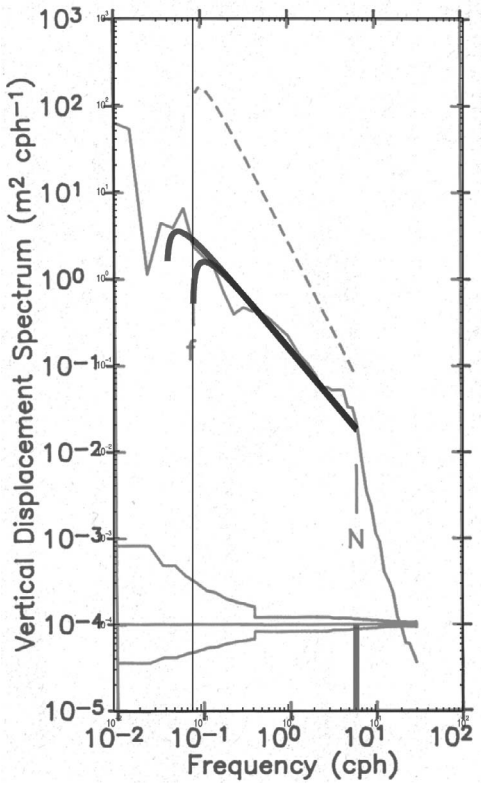

Figure 32. AIWEX frequency spectra of isopycnal displacement gradients. The dashed line represents the GM frequency spectrum, $E(\sigma) \propto \sigma^{-1}(\sigma^2 - f^2)^{-1/2}$. The thick line represents $E(\sigma) \propto \sigma^{-0.2}(\sigma^2 - f^2)^{-1/2}$ with two values for f [from *Levine et al.*, 1987, Figure 2].

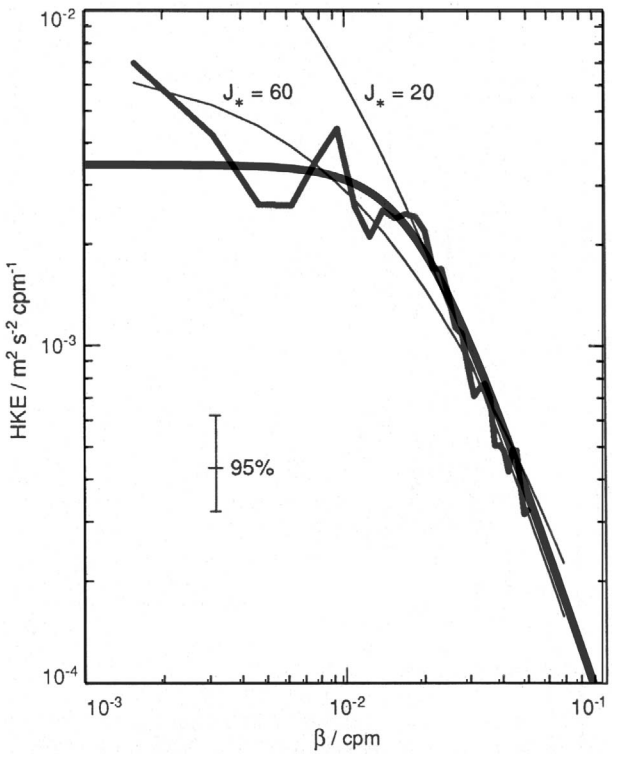

Figure 33. AIWEX vertical wavenumber spectra of horizontal velocity. Thin lines represent fits of the GM75 spectrum, $E_k \propto (1/m_* + m)^{5/2}$, with different values of j_*. This spectrum does not approach its asymptotic roll-off quickly. The thick overlay is $E_k \propto (1/(m_*^3 + m^3))^{0.75}$ with $j_* = 50$ and total energy 0.95×10^{-4} m^2 s^{-2} [from *D'Asaro and Morehead*, 1991, Figure 7].

old paradigm for the spectral balances as a straw man. What we will find in the ensuing discussion is that key components of the straw man require reconsideration.

[115] Figure 34, which is taken from *McComas* [1977], presents one version of the internal wave energy balance in the spectral domain. A similar diagram can be inferred from *Müller and Olbers* [1975]. Energy is gained in region I from surface waves at low vertical wavenumber and high frequency. In the overlapping region II (denoted S.D.), energy is input through interaction with the mesoscale eddy field and moved to region III. Nonlinear interactions transfer energy from region III to region IV via the parametric subharmonic instability. Region V is in equilibrium with respect to nonlinear transfers associated with the induced diffusion mechanism and transports energy to region VI, where dissipation occurs.

[116] We use this straw man to draw focus onto the following questions: (1) Do the observed spectra represent approximate steady states? (2) Are the sources appropriately aligned along or within the spectral domain and of sufficient strength as to balance nonlinear transfers? (3) Does variability of the spectral parameters relate to variability in the forcing?

[117] Intrinsic difficulties with this straw man are that the source distributions are likely to be significantly different than stated and there are significant questions about the characterization of nonlinear transports associated with the weakly nonlinear theory that provides the named mechanisms above.

[118] We proceed by noting that a quantitative explanation of the observed spectral variability requires a corresponding analysis in the spectral domain. In the case of media with weak inhomogeneities the spectral evolution is described by a kinetic equation that has both transfer terms associated with nonlinearity and a transport term that describes the motion of wave packets through the momentum coordinate space. The transport term is a wave analog of Liouville's theorem or the continuity equations for a distribution function in statistical mechanics [*Landau and Lifshitz*, 1980; *Pitaevskii and Lifshitz*, 1981]. The kinetic equation with the transport term is called a radiative balance equation and is given by

$$\frac{\partial n(\mathbf{p})}{\partial t} + \nabla_{\mathbf{r}} \cdot \left[(\overline{\mathbf{u}} + \mathbf{C_g}) n(\mathbf{p})\right] + \nabla_{\mathbf{p}} \cdot [\mathcal{R} n(\mathbf{p})] = S_o(\mathbf{p}) - S_i(\mathbf{p}) + T_r(\mathbf{p}). \quad (23)$$

The factor $\mathbf{C_g} = \nabla_{\mathbf{p}}\omega$ represents the group velocity, $\overline{\mathbf{u}}$ represents subinertial currents, $\mathcal{R} = -\nabla_{\mathbf{r}}(\omega + \mathbf{p} \cdot \overline{\mathbf{u}})$ represents refractive effects associated with spatially inhomogeneous stratification and subinertial currents, T_r represents transfers of action, S_o represents interior sources, and S_i represents sinks (dissipation). Gradient operators in the spatial and spectral domains are $\nabla_{\mathbf{r}}$ and $\nabla_{\mathbf{p}}$, respectively.

[119] Our underlying hypothesis is that the observed variability can be understood as spatially local stationary states of the radiation balance equation (23). Thus, we consider representations of nonlinear transfers $T_r(\mathbf{p})$ in section 5.1, a source function $S_o(\mathbf{p})$ characterization of wave mean interactions (corresponding to terms $\nabla_{\mathbf{r}} \cdot [(\overline{\mathbf{u}} + \mathbf{C_g})\, n(\mathbf{p})] + \nabla_{\mathbf{p}} \cdot [\mathcal{R} n(\mathbf{p})]$) in section 5.2, external forcing $S_o(\mathbf{p})$ in section 5.3, and dissipation $S_i(\mathbf{p})$ in section 5.4. Possible issues related to propagation are addressed in section 5.5. See Figure 35 for a schematic table of contents.

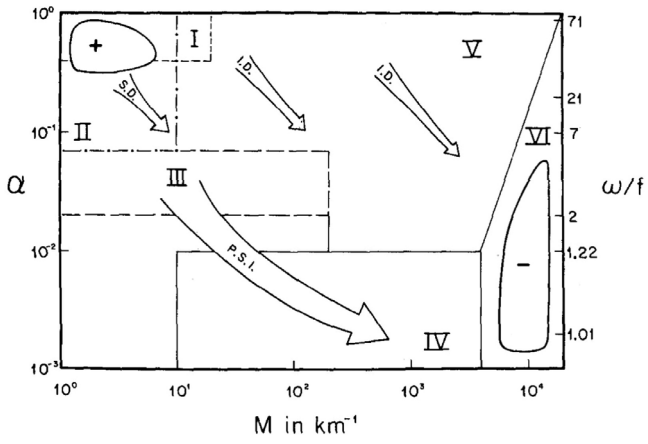

Figure 34. The *McComas* [1977] model for energy flow in the deep sea internal wavefield [from *McComas*, 1977].

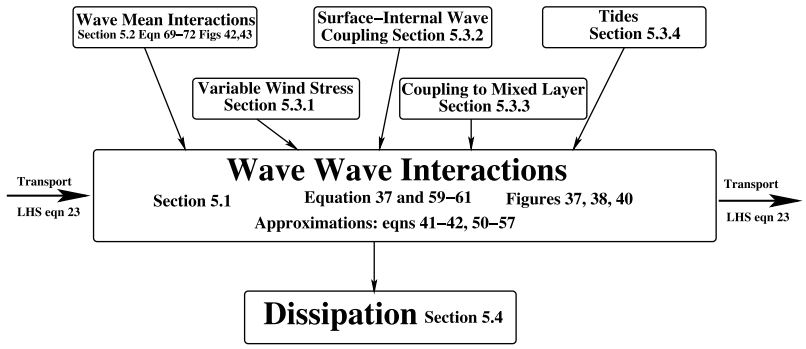

Figure 35. A schematic table of contents for section 5. The radiative balance equation describes the transfer energy in the spectral and spatial domain. Major processes are identified and classified with section, equation, and figure numbers.

5.1. Nonlinearity T_r (p) in (23)

[120] We began this investigation with the hypothesis that the observations, particularly the signature of covariable power laws, represent the end product of a nonlinear equilibration process. Nonlinear interactions between internal waves are a fascinating subject with a significant body of literature spanning 50 years. An inclusive and insightful review is given by *Müller et al.* [1986]. Our discussion below draws from this and includes more recent work.

[121] Our starting place (section 5.1.1) is weak nonlinearity as described by a kinetic equation. A kinetic equation is a closed equation for the time evolution of the wave action spectrum in a system of weakly interacting waves. It is usually derived as a central result of wave turbulence theory. The concepts of wave turbulence theory provide a fairly general framework for studying the statistical steady states in a large class of weakly interacting and weakly nonlinear many-body or many-wave systems. In its essence, classical wave turbulence theory [*Zakharov et al.*, 1992] is a perturbation expansion in the amplitude of the nonlinearity, supposing linear plane wave solutions of $ae^{i(\mathbf{r}\cdot\mathbf{p}-\sigma t)}$ at leading order and a slow amplitude modulation at the next order of the expansion, $a(\tau)\, e^{i(\mathbf{r}\cdot\mathbf{p}-\sigma t)}$, by resonant interactions. This modulation leads to a redistribution of the spectral energy density among space and time scales. Below we sketch the derivation of such an equation following *Zakharov et al.* [1992].

[122] Nonlinearities in the equations of motion are quadratic, so assuming the nonlinearity to be weak, first-order expressions in those equations contain product terms of two waves having wavenumber-frequency ($\mathbf{p}_1$, σ_1) and ($\mathbf{p}_2$, σ_2). For example,

$$\mathbf{u}\cdot\nabla u \propto e^{i(\mathbf{p}_1\cdot\mathbf{r}-\sigma_1 t)} e^{i(\mathbf{p}_2\cdot\mathbf{r}-\sigma_2 t)} = e^{i[(\mathbf{p}_1+\mathbf{p}_2)\cdot\mathbf{r}-(\sigma_1+\sigma_2)t]}. \tag{24}$$

If the combined wavenumber $\mathbf{p}_1 + \mathbf{p}_2$ and frequency $\sigma_1 + \sigma_2$ match those associated with a free wave, resonance occurs, and the amplitude of the third wave grows linearly in time as long as its amplitude remains small. In general, the three-wave resonance conditions can be written as follows:

$$\mathbf{p} = \mathbf{p_1} \pm \mathbf{p_2} \text{ and } \sigma = \sigma_1 \pm \sigma_2. \tag{25}$$

Solutions to (25) are referred to as the resonant manifold, and the three waves form a resonant triad. The possibility of solutions to (25) depends simply upon the geometry of the dispersion surfaces [*Phillips*, 1960]. Such three-wave solutions are possible for internal waves but not, for example, surface gravity waves in deep water.

[123] The evolution of wave amplitude $a_{\mathbf{p}}$ follows most directly from Hamilton's equation,

$$i\frac{\partial}{\partial t}a_{\mathbf{p}} = \frac{\delta\mathcal{H}}{\delta a^*_{\mathbf{p}}}, \tag{26}$$

with Hamiltonian $\mathcal{H}$ that is nominally the sum of kinetic and potential energies, or Lagrange's equation,

$$\frac{d}{dt}\frac{\partial\mathcal{L}}{\partial\dot{a}_{\mathbf{p}}} - \frac{\partial\mathcal{L}}{\partial a_{\mathbf{p}}} = 0, \tag{27}$$

with Lagrangian $\mathcal{L}$ that is the difference of kinetic and potential energies.

[124] Usually, but not always, one needs to adopt a linearization to obtain the Hamiltonian $\mathcal{H}$ in (26) or the Lagrangian $\mathcal{L}$ in (27). The difficulty is that in order to utilize (26) or (27), the Hamiltonian or Lagrangian must first be constructed as a function of the generalized coordinates and momenta and then reexpressed in terms of the complex variables ($a_{\mathbf{p}}$) representing wave amplitude with wavenumber $\mathbf{p}$. It is not always possible to to do so explicitly, in which case one must set up a perturbation expansion which imposes a small amplitude limitation upon the result. See section 5.1.3.1 for further detail.

[125] The Hamiltonian of a system with quadratic nonlinearity can be expressed as [*Zakharov et al.*, 1992]

$$\mathcal{H} = \int d\mathbf{p}\,\sigma_{\mathbf{p}}|a_{\mathbf{p}}|^2 + \int d\mathbf{p}_{012}\Big[\delta_{\mathbf{p}+\mathbf{p}_1+\mathbf{p}_2}\big(U_{\mathbf{p},\mathbf{p}_1,\mathbf{p}_2}a^*_{\mathbf{p}}a^*_{\mathbf{p}_1}a^*_{\mathbf{p}_2} + \text{c.c.}\big) + \delta_{-\mathbf{p}+\mathbf{p}_1+\mathbf{p}_2}\Big(V^{\mathbf{p}}_{\mathbf{p}_1,\mathbf{p}_2}a^*_{\mathbf{p}}a_{\mathbf{p}_1}a_{\mathbf{p}_2} + \text{c.c.}\Big)\Big] \tag{28}$$

after a Fourier decomposition. The interaction coefficients U and V are extended algebraic expressions involving wave amplitude $a_{\mathbf{p}}$, frequency $\sigma_{\mathbf{p}}$, and wavenumber $\mathbf{p}$ of the three waves.

[126] Having obtained the Hamiltonian (28) one introduces wave action as

$$n_{\mathbf{p}} = \langle a^*_{\mathbf{p}} a_{\mathbf{p}} \rangle, \tag{29}$$

where $\langle \ldots \rangle$ means the averaging over statistical ensemble of many realizations of the internal waves. To derive the time evolution of $n_{\mathbf{p}}$ the amplitude equation (26) with Hamiltonian (28) is multiplied by $a^*_{\mathbf{p}}$, the amplitude evolution equation for $a^*_{\mathbf{p}}$ is multiplied by $a_{\mathbf{p}}$, the two equations are differenced, and the result is averaged $\langle \ldots \rangle$ to obtain

$$\frac{\partial n_{\mathbf{p}}}{\partial t} = \Im \int \Big[V^{\mathbf{p}}_{\mathbf{p}_1\mathbf{p}_2} J^{\mathbf{p}}_{\mathbf{p}_1\mathbf{p}_2} \delta(\mathbf{p} - \mathbf{p}_1 - \mathbf{p}_2) - V^{\mathbf{p}_2}_{\mathbf{p}\mathbf{p}_1} J^{\mathbf{p}_2}_{\mathbf{p}\mathbf{p}_1} \delta(\mathbf{p}_2 - \mathbf{p} - \mathbf{p}_1) - V^{\mathbf{p}_1}_{\mathbf{p}\mathbf{p}_2} J^{\mathbf{p}_1}_{\mathbf{p}\mathbf{p}_2} \delta(\mathbf{p}_1 - \mathbf{p}_2 - \mathbf{p}) \Big] d\mathbf{p}_1 d\mathbf{p}_2, \tag{30}$$

where we introduce a triple correlation function

$$J^{\mathbf{p}}_{\mathbf{p}_1\mathbf{p}_2} \delta(\mathbf{p}_1 - \mathbf{p} - \mathbf{p}_2) \equiv \langle a^*_{\mathbf{p}} a_{\mathbf{p}_1} a_{\mathbf{p}_2} \rangle. \tag{31}$$

[127] If we were to have noninteracting fields, i.e., fields with $V^{\mathbf{p}}_{\mathbf{p}1\mathbf{p}2}$ being zero, this triple correlation function would be zero. We therefore invoke a perturbation expansion in smallness of interactions to calculate the triple correlation at first order. The first-order expression for $\partial n_{\mathbf{p}}/\partial t$ thus requires computing $\partial J^{\mathbf{p}}_{\mathbf{p}1\mathbf{p}2}/\partial t$ to first order. To do so, we take definition (31) and use (26) with Hamiltonian (28) and apply $\langle \ldots \rangle$ averaging. We get

$$\begin{aligned} &\left[i\frac{\partial}{\partial t} + (\sigma_{\mathbf{p}_1} - \sigma_{\mathbf{p}_2} - \sigma_{\mathbf{p}_3}) \right] J^{\mathbf{p}_1}_{\mathbf{p}_2\mathbf{p}_3} \\ &= \int \Big[-\frac{1}{2} \left(V^{\mathbf{p}_1}_{\mathbf{p}_4\mathbf{p}_5} \right)^* J^{\mathbf{p}_4\mathbf{p}_5}_{\mathbf{p}_2\mathbf{p}_3} \delta(\mathbf{p}_1 - \mathbf{p}_4 - \mathbf{p}_5) \\ &+ \left(V^{\mathbf{p}_4}_{\mathbf{p}_2\mathbf{p}_5} \right)^* J^{\mathbf{p}_1\mathbf{p}_5}_{\mathbf{p}_3\mathbf{p}_4} \delta(\mathbf{p}_4 - \mathbf{p}_2 - \mathbf{p}_5) \\ &+ V^{\mathbf{p}_4}_{\mathbf{p}_3\mathbf{p}_5} J^{\mathbf{p}_1\mathbf{p}_5}_{\mathbf{p}_2\mathbf{p}_4} \delta(\mathbf{p}_4 - \mathbf{p}_3 - \mathbf{p}_5) \Big] d\mathbf{p}_4 d\mathbf{p}_5. \end{aligned} \tag{32}$$

Here we introduce the quadruple correlation function

$$J^{\mathbf{p}_1\mathbf{p}_2}_{\mathbf{p}_3\mathbf{p}_4} \delta(\mathbf{p}_1 + \mathbf{p}_2 - \mathbf{p}_3 - \mathbf{p}_4) \equiv \langle a^*_{\mathbf{p}_1} a^*_{\mathbf{p}_2} a_{\mathbf{p}_3} a_{\mathbf{p}_4} \rangle. \tag{33}$$

The next step is to assume Gaussian statistics and to express $J^{\mathbf{p}1\ \mathbf{p}2}_{\mathbf{p}3\ \mathbf{p}4}$ as a product of two two-point correlators as

$$J^{\mathbf{p}_1\mathbf{p}_2}_{\mathbf{p}_3\mathbf{p}_4} = n_{\mathbf{p}_1} n_{\mathbf{p}_2} [\delta(\mathbf{p}_1 - \mathbf{p}_3)\delta(\mathbf{p}_2 - \mathbf{p}_4) + \delta(\mathbf{p}_1 - \mathbf{p}_4)\delta(\mathbf{p}_2 - \mathbf{p}_3)].$$

Then

$$\left[i\frac{\partial}{\partial t} + (\sigma_{\mathbf{p}_1} - \sigma_{\mathbf{p}_2} - \sigma_{\mathbf{p}_3}) \right] J^{\mathbf{p}_1}_{\mathbf{p}_2\mathbf{p}_3} = \left(V^{\mathbf{p}_1}_{\mathbf{p}_2\mathbf{p}_3} \right)^* (n_1 n_3 + n_1 n_2 - n_2 n_3). \tag{34}$$

[128] Time integration of the equation for $J^{\mathbf{p}1}_{\mathbf{p}2\mathbf{p}3}$ will contain fast oscillations due to the initial value of $J^{\mathbf{p}1}_{\mathbf{p}2\mathbf{p}3}$ and slow evolution due to the nonlinear wave interactions. Contributions from the first term will rapidly decrease with time, so neglecting these terms we get

$$J^{\mathbf{p}_1}_{\mathbf{p}_2\mathbf{p}_3} = \frac{\left(V^{\mathbf{p}_1}_{\mathbf{p}_2\mathbf{p}_3} \right)^* (n_1 n_3 + n_1 n_2 - n_2 n_3)}{\sigma_{\mathbf{p}_1} - \sigma_{\mathbf{p}_2} - \sigma_{\mathbf{p}_3} + i\Gamma_{\mathbf{p}_1\mathbf{p}_2\mathbf{p}_3}}. \tag{35}$$

Here we introduce the nonlinear damping of the waves $\Gamma_{\mathbf{p}1\mathbf{p}2\mathbf{p}3}$ that relates to the breadth of the resonant manifold. We will elaborate on $\Gamma_{\mathbf{p}1\mathbf{p}2\mathbf{p}3}$ in section 5.1.3. We now substitute (35) into (30), assume for now that the damping of the wave is small, and use

$$\lim_{\Gamma \to 0} \Im \left[\frac{1}{\Delta + i\Gamma} \right] = -\pi \delta(\Delta). \tag{36}$$

We then obtain the three-wave kinetic equation [*Zakharov et al.*, 1992; *Lvov and Nazarenko*, 2004; *Lvov et al.*, 1997]:

$$\begin{aligned} T_r(\mathbf{p}) \equiv \frac{dn_{\mathbf{p}}}{dt} &= 4\pi \int \left| V^{\mathbf{p}}_{\mathbf{p}_1,\mathbf{p}_2} \right|^2 f_{p12}\, \delta_{\mathbf{p}-\mathbf{p}_1-\mathbf{p}_2} \delta(\sigma_{\mathbf{p}} - \sigma_{\mathbf{p}_1} - \sigma_{\mathbf{p}_2}) d\mathbf{p}_{12} \\ &- 4\pi \int \left| V^{\mathbf{p}_1}_{\mathbf{p}_2,\mathbf{p}} \right|^2 f_{12p}\, \delta_{\mathbf{p}_1-\mathbf{p}_2-\mathbf{p}} \delta(\sigma_{\mathbf{p}_1} - \sigma_{\mathbf{p}_2} - \sigma_{\mathbf{p}}) d\mathbf{p}_{12} \\ &- 4\pi \int \left| V^{\mathbf{p}_2}_{\mathbf{p},\mathbf{p}_1} \right|^2 f_{2p1}\, \delta_{\mathbf{p}_2-\mathbf{p}-\mathbf{p}_1} \delta(\sigma_{\mathbf{p}_2} - \sigma_{\mathbf{p}} - \sigma_{\mathbf{p}_1}) d\mathbf{p}_{12}\,, \\ &\text{with } f_{p12} = n_{\mathbf{p}_1} n_{\mathbf{p}_2} - n_{\mathbf{p}} (n_{\mathbf{p}_1} + n_{\mathbf{p}_2})\,. \end{aligned} \tag{37}$$

The δ functions require that the wavenumbers and frequencies sum to zero and ensure that pseudomomentum ($\mathbf{p}n(\mathbf{p})$) and energy ($\sigma_{\mathbf{p}} n(\mathbf{p})$) spectral densities are conserved. The resonant interaction approximation (RIA) is represented by the reduction of (35) to the resonant manifold (25) and δ function representation in (36).

[129] The typical assumptions needed for the derivation of kinetic equations are (1) weak nonlinearity, (2) Gaussian statistics of the interacting wave field in wavenumber space, and (3) resonant wave-wave interactions. In a more systematic derivation, such as that by *Lvov and Nazarenko* [2004], the kinetic equation can be obtained using only an assumption of weak nonlinearity. A theory of weak interaction has its limitations, and this motivates discussions of renormalization attempts to account for increasing nonlinearity (section 5.1.3.2) and ray tracing descriptions of wave-wave interactions (section 5.1.3.3).

5.1.1. Resonant Interactions: Scale-Invariant Solutions

[130] Following Kolmogorov's viewpoint on energy cascades in isotropic Navier-Stokes turbulence, one may look for statistically stationary states using scale-invariant solutions (the scale invariance assumption is, formally, a generic assumption about dependent and independent variables [see, e.g., *Bender and Orzag*, 1978, section 1.7]) to the kinetic equation (37). The solution may occur in an inertial subrange of wavenumbers and frequencies that are far from those where forcing and dissipation act and also far from characteristic scales of the system, including the Coriolis frequency resulting from the rotation of the Earth, the buoyancy frequency due to stratification, and the ocean depth. Under these assumptions, the dispersion relation and

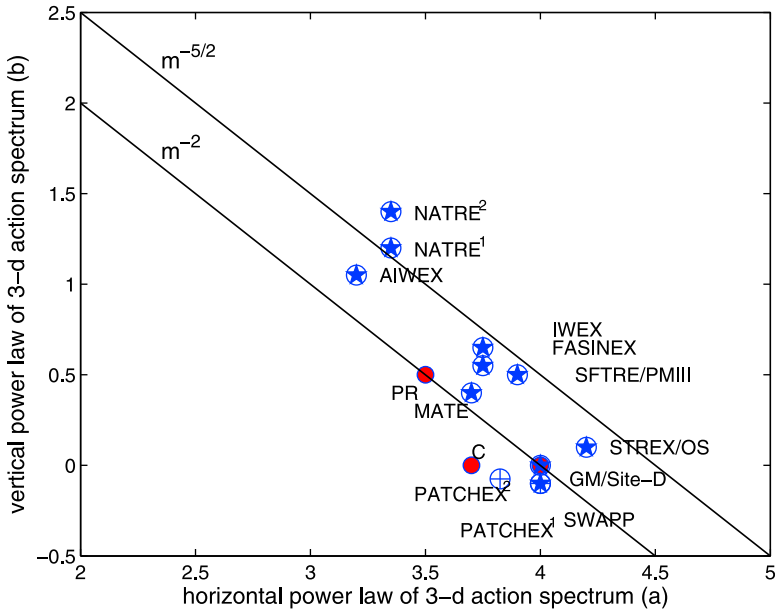

Figure 36. The observational points. The solid circles represent the Pelinovskii-Raevsky (PR) spectrum ($(a, b) = (3.5, 0.5)$), the convergent numerical solution ($(a, b) = (3.7, 0.0)$) determined by *Lvov et al.* [2010], and the GM spectrum ($(a, b) = (4.0, 0.0)$). Circles with stars represent estimates based upon one-dimensional spectra from the western North Atlantic south of the Gulf Stream (IWEX, FASINEX, and SFTRE/PMIII), the eastern North Pacific (STREX/OS and PATCHEX[1]), the western North Atlantic north of the Gulf Stream (Site D), the Arctic (AIWEX), and the eastern North Atlantic (NATRE[1] and NATRE[2]). There are two estimates obtained from two-dimensional data sets from the eastern North Pacific (SWAPP and PATCHEX[2]) represented as circles with cross hairs. NATRE[1] and NATRE[2] represent fits to the observed spectra and observed minus vortical mode spectra, respectively. Lines of constant vertical wavenumber power laws for the observed energy spectrum run diagonally downward. Lines of constant frequency power laws are vertical.

the interaction matrix elements are locally scale invariant, and solutions of (37) take the form

$$n(\mathbf{k}, m) = |\mathbf{k}|^{-a}|m|^{-b}. \tag{38}$$

Values of a and b such that the right-hand side of (37) vanishes identically correspond to steady solutions of the kinetic equation and hopefully also to statistically steady states of the ocean's wave field.

[131] To connect with the observations, the corresponding vertical wavenumber-frequency spectrum of energy is obtained by transforming $n_{\mathbf{k},m}$ from the three-dimensional wavenumber space ($\mathbf{k}$, m) to the two-dimensional vertical wavenumber-frequency space (σ, m) and multiplying by frequency. In the high-frequency–high-wavenumber limit,

$$E(m, \sigma) \propto m^{2-a-b}\sigma^{2-a}.$$

The frequency-wavenumber power laws inferred from the observations ($m^{-q}\sigma^{-r}$) are thus related as

$$r = a - 2,\ q = a + b - 2.$$

[132] Parametric fits to the observations (Figure 36) produce a clustering about two regions of parameter space with several notable outliers. Observations from Site D and from the subtropical North Pacific tend to cluster about the GM76 power laws ($m^{-2}\sigma^{-2}$). These data were obtained in regions poleward of the critical latitude (28.9) at which the M_2 semidiurnal tide can decay into near-inertial frequencies through a parametric subharmonic instability. The MATE data from the subpolar North Pacific and observations from south of the Gulf Stream are grouped together with power laws describing spectra distinctly redder (whiter) in the vertical wavenumber (frequency) domain. This grouping includes data both poleward and equatorward of the semidiurnal critical latitude. Observations from the eastern North Atlantic (NATRE), the Arctic (AIWEX), and, tentatively, the subpolar North Pacific (Ocean Storms) appear as outliers.

5.1.1.1. Nonrotating ($f = 0$) Limit

[133] Unlike Kolmogorov turbulence, the exponents which give steady solutions to (37) cannot be determined by dimensional analysis alone. This is the case owing to multiple characteristic length scales in anisotropic systems [e.g., *Polzin*, 2004a]. The anisotropic analysis is much more complicated, and as a prelude to that discussion we enquire whether the improper integrals in (37) converge. This is related to the question of locality of the interactions: a convergent integral characterizes the physical scenario where interactions of neighboring wavenumbers dominate the evolution of the

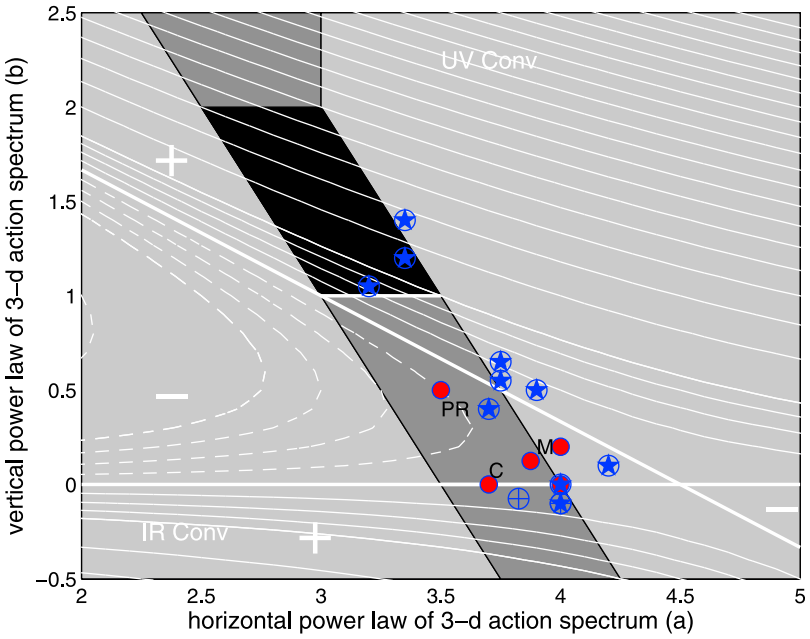

Figure 37. The observational points and the theories [*Lvov et al.*, 2010]. The solid circles represent scale-invariant stationary states identified by *Pelinovskii and Raevsky* [1977], a convergent numerical solution determined by *Lvov et al.* [2010], the GM spectrum, and two possible dynamic balances identified by *McComas and Müller* [1981b]. Circles with stars represent power law estimates based upon one-dimensional spectra. Circles with cross hairs represent estimates based upon two-dimensional data sets. See Figure 36 for the identification of the field programs. Light grey shading represents regions of the power law domain for which the collision integral converges in either the infrared or ultraviolet limit. The dark grey shading represents the region of the power law domain for which neither the infrared nor the ultraviolet limits converge. The region of black shading represents the subdomain for which the infrared and ultraviolet divergences have the same sign. Additionally, a line segment between $3 < a < 7/2$ along $b = 1$ is IR convergent, and a line segment between $7/2 < a < 4$ along $b = 0$ is IR and UV convergent. These line segments arise as higher-order cancellations in the integrand. Overlain as solid white lines are the induced diffusion stationary states. Thin white contours are proportional to the factor $b(9 - 2a - 3b)$ in (41) with contour intervals of $\pm(0.25, 0.50, 0.75, 1.0, 2.0, 3.0, \ldots)$. The plus and minus signs denote the sign of the action tendency (37) in the $a - b$ domain.

wave spectrum, while a divergent one implies that distant, nonlocal interactions in the wavenumber space dominate.

[134] It turns out that the internal wave collision integral diverges (a contrary assessment is given by *Lvov et al.* [2004]; that result is associated with a sign error in the numerical evaluation of (37)) for almost all values of a and b. In particular, the collision integral has an infrared (IR) divergence at zero, i.e., $|\mathbf{k}_1|$ or $|\mathbf{k}_2| \to 0$, and an ultraviolet (UV) divergence at infinity, i.e., $|\mathbf{k}_1|$ and $|\mathbf{k}_2| \to \infty$. A detailed analysis performed by *Lvov et al.* [2010] returns the convergence conditions in the IR limit, $\mathbf{k}_1$ or $\mathbf{k}_2 \to 0$ of

$$a + b/2 - 7/2 < 0 \text{ and } -3 < b < 3,$$

$$a - 4 < 0 \text{ and } b = 0,$$

$$a - 7/2 < 0 \text{ and } b = 1,$$

$$a + b - 5 < 0 \text{ and } b > 3,$$

or

$$a - 5 < 0 \text{ and } b < -3. \tag{39}$$

[135] Similarly, convergence in the UV limit $|\mathbf{k}_1|$ and $|\mathbf{k}_2| \to \infty$ implies that

$$a + b/2 - 4 > 0 \text{ and } -2 < b < 2,$$

$$a - 7/2 > 0 \text{ and } b = 0,$$

$$a - 3 > 0 \text{ and } b > 2,$$

or

$$a + b - 3 > 0 \text{ and } b < -2. \tag{40}$$

The domains of divergence and convergence are shown in Figure 37.

[136] There is only one exception where the integral converges in both limits: the line segment along $b = 0$ with $7/2 < a < 4$. Moreover, there is one special value, $(a, b) = (3.7, 0)$, in which IR and UV contributions are both convergent and cancel. That is, $(a, b) = (3.7, 0)$ represents a stationary state of the kinetic equation in the absence of rotation. Note that the line $b = 0$ is "special" in that it corresponds to wave action independent of vertical wavenumbers, $\partial n(\mathbf{p})/\partial m = 0$.

This convergent solution lies in the general proximity of GM76 (a, b) = (4, 0) and observations from Site D, SWAPP, and PATCHEX.

[137] The possibility also exists that one can construct a divergent solution in the following sense. If the UV and IR nonintegrable singularities have opposite signs for some (a, b), it may be possible to devise a conformal mapping that matches the oppositely signed singularities. In this case one would have, at least on the level of a technical mathematical exercise, an approximate stationary state. *Pelinovskii and Raevsky* [1977], *Caillol and Zeitlin* [2000], and *Lvov and Tabak* [2001] find this to be possible for (a, b) = (3.5, 0.5). *Lvov et al.* [2010] determine that such solutions are more general, and possible approximate stationary states occupy the dark grey shaded regions of Figure 37. The black regions are not permitted because of UV and IR divergences having similar signs.

[138] The parametric spectral estimates tend to have larger a values than either the convergent or the *Pelinovskii and Raevsky* [1977] solution and also tend to lie on the border of UV convergence. One instance (NATRE) is seen to occupy the black region, but this point migrates to a state of UV convergence if an attempt is made to subtract nonwave fine structure (see section 3.3.4 for details).

[139] Although it represents a possible stationary state, a balance between divergent and oppositely signed integrals is not a satisfactory physical situation. What it represents is a statement that integration endpoints other than $\pm\infty$ need to be inserted in (37). Obvious candidates are f in the IR limit and N in the UV limit.

5.1.1.2. $f \neq 0$: Extreme-Scale Separated Interactions

[140] When the kinetic equation is evaluated on the resonance surface, extreme-scale separated interactions are believed to dominate the transfers [*Lvov et al.*, 2010; *Müller et al.*, 1986]. Thus, approaching the issue of scale-invariant solutions to the kinetic equation is not as simple as a spectrally local energy cascade. A detailed analysis of the extreme-scale separated interactions is required. Three simple interaction mechanisms were identified by *McComas and Bretherton* [1977] in the limit of an extreme-scale separation. The limiting cases are as follows: (1) the vertical backscattering of a high-frequency wave by a low-frequency wave of twice the vertical wavenumber into a second high-frequency wave of oppositely signed vertical wavenumber, which is called elastic scattering; (2) the scattering of a high-frequency wave by a low-frequency, small-wavenumber wave into a second, nearly identical, high-frequency large-wavenumber wave, which is called induced diffusion (ID); and (3) the decay of a low-wavenumber wave into two high vertical wavenumber waves of approximately one half the frequency, which is referred to as the parametric subharmonic instability (PSI) and was identified by *McComas and Bretherton* [1977] as causing the transfer of energy from frequencies of $2f$ and low vertical wavenumber to high vertical wavenumber near inertial oscillations in the GM spectra. Below we review how these extreme-scale separated interactions can address the observed covariability in power law fits.

5.1.1.3. Induced Diffusion and Covariable Power Laws

[141] One can further reduce (37) in the ID limit to a Fokker-Plank equation [*Gardiner*, 2004; *McComas and Bretherton*, 1977],

$$\frac{\partial n(\mathbf{p})}{\partial t} = \frac{\partial}{\partial \mathbf{p}_i} D_{ij} \frac{\partial}{\partial \mathbf{p}_j} n(\mathbf{p}), \tag{41}$$

such that

$$D_{ij} = 2 \int\int d^3\mathbf{p}' d^3\mathbf{p}''\, n(\mathbf{p}'') \mathbf{p}_i'' \mathbf{p}_j'' \left| V^{\mathbf{p}}_{\mathbf{p}',\mathbf{p}''} \right|^2 \delta(\mathbf{p} - \mathbf{p}' - \mathbf{p}'') \cdot \delta(\sigma - \sigma' - \sigma''), \tag{42}$$

in which $\mathbf{p}$ and $\mathbf{p}'$ are the wave vectors of high-frequency waves, $\mathbf{p}''$ is the wave vector of the low-frequency member of the triad, and $|V^{\mathbf{p}}_{\mathbf{p}',\mathbf{p}''}|^2 \cong (\pi/2)\sigma'' k^2$. To obtain the Fokker-Plank equation, one (1) neglects terms quadratic in high-frequency amplitude relative to linear terms; (2) expands $[n(\mathbf{p} - \mathbf{p}'') - n(\mathbf{p})]$ in a Taylor series; (3) sums the formulae for the two cases $|\mathbf{p}'| > |\mathbf{p}|$ and $|\mathbf{p}'| < |\mathbf{p}|$; and (4) noting the subtractive cancelation between the two, performs a second Taylor series expansion. *McComas and Bretherton* [1977] present scale estimates of (41) and argue that the vertical coordinate dominates the transfers, thereby reducing the integral expression to being proportional to the vertical gradient variance (i.e., shear variance) along the resonance curve. We reconsider these arguments in section 5.1.1.5.

[142] Substituting the scale-invariant solution (38) into (41), one obtains, for the GM class of spectra in which near-inertial frequencies dominate the shear variance, stationary states if either

$$9 - 2a - 3b = 0 \quad \text{or} \quad b = 0. \tag{43}$$

Lvov et al. [2010] obtain this result via rigorous asymptotic arguments, independent of the reduction of kinetic equation (37) to Fokker-Plank equation (41). *McComas and Müller* [1981b] interpret $b = 0$ as a no action flux in vertical wavenumber domain, while $9 - 2a - 3b = 0$ is a constant action flux solution. Power laws $b \gtrless 0$ imply a down-gradient action flux to higher or lower vertical wavenumber along lines of constant horizontal wavenumber. Associated with this is the transport of action to lower or higher frequency and the gain or loss of energy by the near-inertial field. A positive residual to (37) implies an increase in high vertical wavenumber, high-frequency spectral density and is consonant with a balance between resonant transfers and a high-wavenumber sink.

[143] The situation changes in the absence of rotation ($f = 0$). In this case, similar manipulations suggest that stationary states can be obtained if either

$$b - 1 = 0 \quad \text{or} \quad b = 0, \tag{44}$$

in which $b = 1$ is the constant action flux solution of the Fokker-Plank equation.

[144] The majority of the observational data points cluster in two groups that are not far from the ID stationary states for scale-invariant solutions (Figure 37). The observations exhibit a tendency to lie in regions having either small transport ($b = 0$) or transport to higher vertical wavenumber and lower frequency ($b > 0$). The observations also tend to lie in regions having a positive residual, for which $\partial n/\partial t > 0$ and is consistent with a balance between the ID flux convergence and an unspecified sink. The most extreme departure from the ID stationary states is NATRE, which is equatorward of the critical latitude for the semidiurnal lunar tide and has an anomalously large vertical wavenumber bandwidth ($j_* = 18$).

[145] However appealing the apparent pattern match between the observations and stationary states under the ID mechanism may be, we believe there is more to the story. That story includes numerical evaluations of the kinetic equation which contain significant residuals inconsistent with GM76 being a stationary state. These residuals lead us to consider how increasing levels of nonlinearity at high wavenumber could change our interpretations in section 5.1.3. Before doing so, though, we fill in a bit of the background by discussing the dynamic balance of *McComas and Müller* [1981b].

5.1.1.4. The Dynamic Balance

[146] A quantitative formulation of the internal wave energy budget is given structure by the dynamic balance put forward by *McComas and Müller* [1981b]. This key study ascribes an inertial subrange character to the GM76 spectrum after integrating over the frequency domain. The dynamic balance is constructed by dividing the frequency domain into distinct regions and characterizing each region with transfers associated with the dominant triad class. Thus, frequencies of $f < \sigma < 2f$ and vertical wavenumber m gain energy via PSI transfers from frequencies of $2f < \sigma < 4f$ and lower wavenumber. Frequencies of $2 < \sigma < 4f$ and wavenumber m lose energy via PSI transfers to frequencies of $f < \sigma < 2f$ and higher wavenumber and also gain energy via ID energy spectral fluxes across $\sigma = 4f$. Frequencies $\sigma > 4f$ and wavenumber m gain or lose energy as action is transferred to higher or lower vertical wavenumber in association with ID coupling to near-inertial waves of smaller vertical wavenumber. Finally, frequencies $\sigma = f$ and wavenumber m gain or lose energy in association with ID coupling to high-frequency waves $\sigma > 4f$. These domains are apparent in the schematic from *McComas* [1977] (Figure 34) and in numerical evaluations of the kinetic equation (e.g., Figure 40). Matching expressions for the energy spectrum and its time rate of change across the boundary $\sigma = 4f$ provides the high-frequency solution

$$E_{ID}(\sigma,\beta) = E\frac{\beta_*}{\beta^2}\frac{f}{\sigma^2}\left[1 + \frac{27}{64x}\ln\frac{\sigma}{4f}\right], \tag{45}$$

which is nicely fit by a power law $n(\mathbf{p}) \propto k^{-3.875}\, m^{-0.125}$. Matching along $\beta = \beta_*$ provides

$$E_{ID}(\sigma,\beta) = E\frac{\beta_*}{\beta^2}\frac{f}{\sigma^2}\left[1 - \frac{27}{64x}\ln\frac{\beta}{\beta_*}\right], \tag{46}$$

which is fit by a power law $n(\mathbf{p}) \propto k^{-4.0}\, m^{-0.20}$. Both solutions are plotted in Figure 37.

[147] One of the attractive properties of the first solution ($(a, b) \simeq (3.875, 0.125)$) is that the expressions for energy transport to small vertical scale lead to estimates that are difficult to distinguish from turbulent dissipation estimates obtained as part of the PATCHEX field program [*Gregg*, 1988]. These estimates, along with those obtained in NATRE [*Polzin et al.*, 1995], pin down the GM76 dissipation rate at approximately 8×10^{-10} W kg^{-1}. See *Polzin* [2004a] for discussion.

[148] There are, however, several disquieting issues. The first is that the downscale energy transport occurs only in vertical wavenumber and thus requires an energy source at high frequency. The second is the requirement of integrating over the frequency domain and invocation of dissipation to obtain a stationary state. The RIA dissipation mechanism (section 5.4.2) acts primarily on near-inertial shear, whereas numerical evaluations of the kinetic equation (section 5.1.1.5) indicate significant nonstationary tendencies at high frequencies.

5.1.1.5. Numerical Evaluations of (37)

[149] The analysis presented above was based upon analytic work. Here we report numerical evaluations of the kinetic equation expressed via the Boltzman rate,

$$\nu_B = \frac{\dot{n}(\mathbf{p})}{2n(\mathbf{p})}. \tag{47}$$

The Boltzman rate represents the net rate of transfer for wavenumber $\mathbf{p}$ and is a low-order measure of nonlinearity for smooth, isotropic, and homogeneous spectra. The individual rates of transfer into and out of $\mathbf{p}$ may be significantly larger for spectral spikes [*Pomphrey et al.*, 1980; *Müller et al.*, 1986] and potentially for smooth, homogeneous, but anisotropic spectra.

[150] A characterization of the level of nonlinearity is made by normalizing the Boltzman rate by the characteristic linear time scale $\tau^{\mathrm{L}}_{\mathbf{p}} = 2\pi/\sigma_{\mathbf{p}}$:

$$\epsilon_{\mathbf{p}} = \frac{2\pi\dot{n}_{\mathbf{p}}}{n_{\mathbf{p}}\sigma_{\mathbf{p}}}. \tag{48}$$

A stationary state is defined by $\epsilon_{\mathbf{p}} = 0$. The normalized Boltzman rate (48) serves as a low-order consistency check for the various kinetic equation derivations. An $O(1)$ value of $\epsilon_{\mathbf{p}}$ implies that the derivation of the kinetic equation is internally inconsistent.

[151] We present evaluations of the kinetic equation as discussed by *Lvov et al.* [2011]: we use a numerical scheme designed for off-resonant calculations using the *Lvov and Tabak* [2004] Hamiltonian, and then we take the resonant limit. See also section 5.1.3.1. We use two spectra that mimic those at Site D (GM76 with $(a, b) = (4.0, 0.0)$) and the Sargasso Sea ($(a, b) = (3.75, 0.50)$; Appendix D).

[152] The characteristic pattern for GM76 is two positive and one negative lobe in the vertical wavenumber-frequency domain with boundaries at approximately $2f$ and $5f$ (Figure 38). Action loss at frequencies $2f < \sigma < 5f$ is qualitatively consistent with the PSI mechanism transferring energy into near-inertial frequencies [*McComas and Müller*, 1981a]. The residual at $\sigma \cong 2f$ is, however, nearly an order of magnitude larger than what would be predicted from the

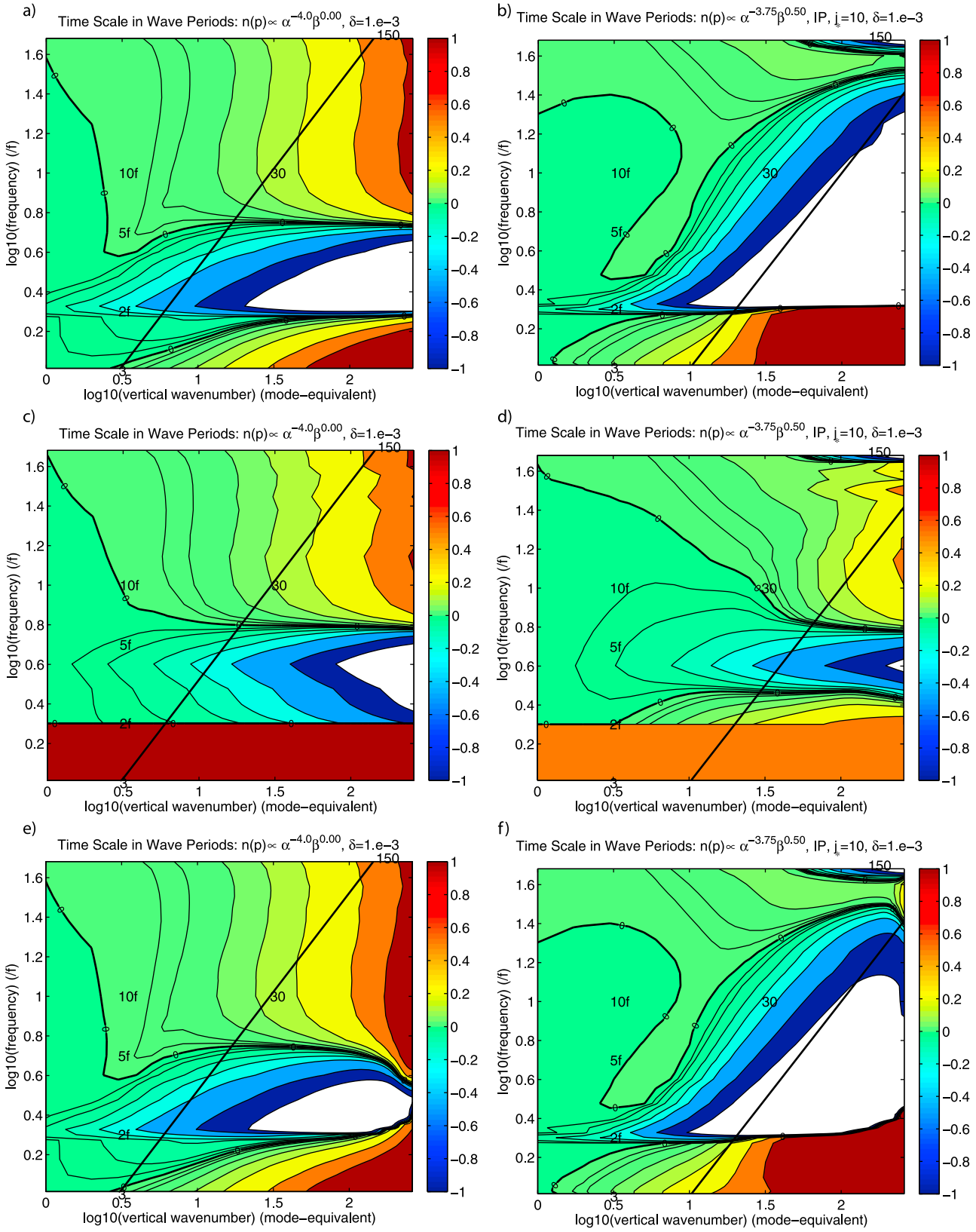

Figure 38

PSI time scale [*McComas and Müller*, 1981a], which leads to

$$\text{PSI}: \qquad \epsilon_{\mathbf{p}} = \frac{\pi^3}{10x}\frac{27}{32}\frac{m}{m_c}, \tag{49}$$

with $x = \sqrt{10}$ and m_c a high-wavenumber cutoff defined in (17). Comparative figures for GM76 are given by *McComas and Bretherton* [1977, Figure 10], *McComas* [1977, Figure 3], *McComas and Müller* [1981b, Figure 11], and *Pomphrey et al.* [1980, Figure 6].

[153] Normalized Boltzman rates within the ID regime $\sigma > 5f$ are both $O(1)$ and positive. The fact that they are $O(1)$ is indicative that GM76 is not a stationary state, and the fact that they are positive is troubling in that the nearby state of (45) was specifically selected by *McComas and Müller* [1981b] as having ID transfers with $\dot{n}(\mathbf{p}) < 0$ to match a similar signed tendency along the ID-PSI boundary $\sigma = 4f$. To resolve this we interpret the results in terms of the convergence conditions of the collision integral.

[154] The rigorous asymptotic analysis presented by *Lvov et al.* [2010] finds that both ultraviolet and infrared limits to the collision integral converge along $3.5 < a < 4$ and $b = 0$. Thus, interactions along this line segment are local in the nonrotating limit. With the addition of rotation the mathematical properties of the collision integral could be altered, but note that the line $b = 0$ corresponds to an action spectrum with vanishingly small amplitude gradients in vertical wavenumber, with correspondingly small transfers that depend upon those gradients, such as the ID mechanism. We therefore infer that the positive contours tending vertical at the highest frequencies are unrelated to extreme-scale separated ID transfers.

[155] We double check this inference by noting that locality implies that frequencies of $f < \sigma < 2f$ make little contribution to the collision integral. If such low frequencies are excluded from the numerical evaluations, we find $\dot{n}(\mathbf{p})$ to be virtually unchanged for GM76 at frequencies $\sigma > 4f$ (Figure 38). Similarly, we find little change if the wavenumber domain is limited to $m < 2\ m_c$ and $k < 2\ m_c$. The influence of extreme-scale separated ID transfers in Figure 38 would be apparent as contours of $\epsilon_{\mathbf{p}}$ tending to be parallel to σ/m = constant in the vicinity of $m = m_*\sigma/f$, i.e., at small vertical wavenumbers prior to the asymptotic roll-off. Such an influence is not apparent in any of these GM76 evaluations.

[156] Finally, we note that in the asymptotic limit of high vertical wavenumber, the gradients of the 3-D action spectrum in vertical wavenumber are vanishingly small for $b = 0$. We therefore hypothesize that local interactions giving rise to these residuals are related to the gradients of the 3-D action spectrum in horizontal wavenumber. A consequence of transfers in horizontal wavenumber is that it potentially changes the energy source at high frequency required by the vertical wavenumber Fokker-Plank equation (41)!

[157] The Sargasso Sea power law combination represents a constant action flux solution $9 - 2a - 3b = 0$ to Fokker-Plank equation (41). Comparative figures for the nearby state of GM75 ($(a, b) = (4.0, 0.5)$) are given by *Olbers* [1976, Figure 4], *McComas and Bretherton* [1977, Figure 12], and *Pomphrey et al.* [1980, Figure 6]. A bandwidth of $j_* = 10$ has been chosen as being representative of the region, and the amplitude has been specified to return a gradient variance at $\lambda_v = 10$ m similar to the GM76 spectrum. The pattern for the Sargasso Sea is, excepting $\sigma \cong N$, a consistent negative tendency for $\sigma > 2f$ and for contours to be parallel to the ID resonance condition of $m_* = fm/\sigma$. Tendencies lead to $\epsilon_{\mathbf{p}} \cong O(1)$ at $m = m_c$. Such $O(1)$ tendencies are inconsistent with the power law combination being a stationary state, but we note that this is potentially an artifact of the high-wavenumber, high-frequency domain $(m, \sigma) = (m_c, N)$ not being within the asymptotic regime of $\sigma/m \gg f/m_*$.

[158] Truncating the spectral domain to exclude frequencies $\sigma < 2f$ changes the tendencies considerably, so that the sign and magnitude are similar to those of GM76. Truncating the spectral domain to exclude vertical wavenumbers $m > 2m_c$ changes only the results at highest vertical wavenumber. These diagnostics suggest that the Sargasso Sea results fit much better into the extreme-scale separated scenario, but local interactions cannot be neglected.

5.1.2. Resonant Interactions: Departures From Scale Invariance

5.1.2.1. NATRE: PSI Decay of a Tidal Peak

[159] The parametric subharmonic instability described in section 5.1.1.2 has also been cited as providing a pathway for the transfer of energy from low-mode internal tides [*Hibiya et al.*, 2002; *MacKinnon and Winters*, 2005]. The question of whether such PSI transfers can explain the unique character of the NATRE spectrum is examined by K. L. Polzin (A regional characterization of the Eastern Subtropical Atlantic internal wave spectrum, manuscript in preparation, 2011). On the assumptions that $m' \ll m, m''$ and $\sigma' \sim 2\sigma \sim 2\sigma'' \sim 2f$, the transfer integral reduces to

$$T_r(\mathbf{p}) \cong 2\int d\mathbf{p}' \left| V^{\mathbf{p}}_{\mathbf{p}',(\mathbf{p}'-\mathbf{p})} \right|^2 \delta[\sigma - \sigma' + \sigma(\mathbf{p}' - \mathbf{p})] \cdot \{n(\mathbf{p}')[n(\mathbf{p}) + n(\mathbf{p}' - \mathbf{p})] - n(\mathbf{p})n(\mathbf{p}' - \mathbf{p})\} \tag{50}$$

Figure 38. Normalized Boltzman rates (48) calculated via (59) using the *Lvov and Tabak* [2004] matrix elements with $\delta = 10^{-3}$. (a, c, and e) The GM76 (18) spectrum and (b, d, and f) Sargasso Sea power laws (Appendix D). Figures 38a and 38b utilize a spectrum that extends to $m = 8m_c$, $k = 8m_c$, with m_c defined in (17). Figures 38c and 38d are the same as Figures 38a and 38b but with $E(\sigma < 2f, m) = 0.0$. Figures 38e and 38f are the same as Figures 38a and 38b but with restricted vertical $m < 2m_c$ and horizontal $k < 2m_c$ wavenumbers. Results are only plotted for $m < m_c$. A value of $\delta = 10^{-3}$ represents the resonant interaction limit. The black diagonal lines represent the ID resonance curve ($f/m* = \sigma/m$) extending from m_*. Contour values are (0, ±0.01, ±0.02, ±0.05, ±0.1, ±0.2, ±0.5, ±1.0).

for the gain at high wavenumber. The transfer function $|V^{\mathbf{p}}_{\mathbf{p}',(\mathbf{p}'-\mathbf{p})}|^2$ in this limit is given by *McComas and Müller* [1981a]:

$$\left|V^{\mathbf{p}}_{\mathbf{p}',(\mathbf{p}'-\mathbf{p})}\right|^2 = \frac{-\pi}{8}\frac{\sigma'^3}{\sigma(\sigma'-\sigma)}\left[\frac{\sigma'^2-f^2}{\sigma'^2}\right]^2\frac{\sigma'^2-f^2}{N^2}m'^2. \quad (51)$$

[160] *McComas and Müller* [1981a] note that with $n(\mathbf{p}) \sim n(\mathbf{p}'') \ll n(\mathbf{p}')$ the transfer integral further reduces:

$$T_r(\mathbf{p}) \cong -\frac{\pi}{4}[n(\mathbf{p})+n(-\mathbf{p})]\frac{\sigma_T^3}{\sigma(\sigma'-\sigma)}\left[\frac{\sigma_T^2-f^2}{\sigma_T^2}\right]^2 \cdot \frac{\sigma_T^2-f^2}{N^2}\int m'^2 n(\sigma_T,m')dm', \quad (52)$$

with $n(\sigma, m)$ a 2-D action spectrum and semidiurnal tidal frequency σ_T. The difference between *McComas and Müller* [1981a] and (52) is that *McComas and Müller* [1981a] assume $n(\mathbf{p}')$ to be a continuous spectrum, and here $n(\mathbf{p}')$ represents an internal tide, bandwidth limited to a narrow range of frequencies. Assuming further that the internal tide is concentrated in mode 1 (m_1), the characteristic growth rate at high wavenumbers is explicitly given by

$$T_r(\mathbf{p})/n(\mathbf{p}) = \tau^{-1}(\mathbf{p}) \cong 2\pi\left[\frac{\sigma_T^2-f^2}{\sigma_T^2}\right]^2\frac{\sigma_T^2-f^2}{N^2}m_1^2E(\sigma_T), \quad (53)$$

with $E(\sigma)$ being the 1-D energy spectrum.

[161] The total rate of energy transfer from the semidiurnal tide to the near-inertial field is

$$\int \sigma T_r d^3k = \int d^3k E(\mathbf{p})\tau^{-1}(\mathbf{p}) = E_{ni}/\tau, \quad (54)$$

with near-inertial energy E_{ni} and time scale τ from (53). This assumes that the near-inertial energy E_{ni} is resonant with the tide. One of the restrictions of the kinetic equation is apparent in (53). The tide cannot be regarded as a single plane wave. Doing so implies that $E(\sigma_T) = E_o\delta(\sigma-\sigma_T)$, so that the transfer rate is infinite. Numerical simulations of PSI transfers [*MacKinnon and Winters*, 2005] indicate large and perhaps unrealistic transfer rates if forced with a single plane wave.

[162] When used as a diagnostic, Polzin (manuscript in preparation, 2011) report that (54) tends to overestimate observed dissipation rates. An additional concern is that the NATRE spectrum is unique in both its vertical wavenumber domain power law and extreme bandwidth. Implied is a scale selection process that is not represented in (54), which states that production is proportional to the shear in the tide times the near-inertial energy.

[163] This can be rectified by noting that the limit $n(\mathbf{p})$, $n(\mathbf{p}'') \ll n(\mathbf{p}')$ does not need to be taken. Since $n(\mathbf{p}'') = n(-\mathbf{p}-\mathbf{p}')$, if one simply assumes that $n(\mathbf{p}'') \cong n(-\mathbf{p})$, then

$$T_r(\mathbf{p}) \cong \frac{\pi}{4}\frac{\sigma_T^3}{\sigma(\sigma_T-\sigma)}\left[\frac{\sigma_T^2-f^2}{\sigma_T^2}\right]^2\frac{\sigma_T^2-f^2}{N^2} \left\{-[n(\mathbf{p})+n(-\mathbf{p})]\int m'^2 n(\sigma_T,m')dm' + [n(\mathbf{p})n(-\mathbf{p})]\frac{\sigma_T}{N^2}\int m'^4 dm'\right\}. \quad (55)$$

Resonance constraints imply that

$$\int m'^4 dm' = \frac{1}{5}m^5\Big|_{\gamma m_1}^{m}, \quad (56)$$

in which γ is the minimum ratio of m'/m permitted by resonance constraints. The factor γ is approximately 1.5–2.0 for NATRE. The term quadratic in near-inertial amplitude represents a scale selection principle.

[164] A diagnostic for application to observed fields is obtained by summing the wave action tendency equations for $n(\mathbf{p})$ and $n(\mathbf{p}'')$; converting from a wave vector representation of the 3-D wave action spectrum to a 2-D energy spectrum in vertical wavenumber-frequency coordinates; and remembering that the observations, in distinction to the theory, reference a one-sided, rather than two-sided, spectrum. The conversion from 3-D to 2-D assumes that the wavefield is horizontally isotropic. The end result is that

$$T_r(\mathbf{p}) \cong -\frac{4\gamma n(\mathbf{p})}{\sigma_T}\left[\int m'^2 E(\sigma_T,m')dm' - \frac{1}{80\pi}\frac{\sigma_T^2}{\sigma^2}m^3E(\sigma,m)\right] \quad (57)$$

with

$$\gamma = \frac{\pi}{8}\frac{\sigma_T^3}{\sigma(\sigma'-\sigma)}\left[\frac{\sigma_T^2-f^2}{\sigma_T^2}\right]^2\frac{\sigma_T^2-f^2}{N^2}.$$

[165] The total transfer from the tide to the near-inertial field is (Polzin et al., manuscript in preparation, 2011)

$$P = \int P(\mathbf{p})d^3k = \int 2\pi\left[\frac{\sigma_T^2-f^2}{\sigma_T^2}\right]^2\frac{\sigma_T^2-f^2}{N^2}E(\mathbf{p}) \times \left[m'^2E(\sigma_T) - \frac{m^3}{20\pi}E(\sigma,m)\right]. \quad (58)$$

[166] Polzin et al. (manuscript in preparation, 2011) report a close correspondence between production (58) and the observed dissipation rate and interpret the roll-off of the vertical wavenumber spectrum as a cancelation between

$$m'^2E(\sigma_T)$$

and

$$\frac{m^3}{20\pi}E(\sigma,m).$$

5.1.2.2. The Dip: ID Decay of a Tidal Peak

[167] The same argument used to provide a scale selection principle in PSI can be invoked for ID. The term quadratic in high-frequency amplitude is dropped in the induced diffusion approximation (41). This term represents a consistent energy loss from the high-frequency field to the low-frequency tide. In this instance the quadratic term is largest when the scale separation is smallest and the arguments used to produce the ID approximation break down. *Furuichi et al.* [2005] report an analysis of energy transfers between a tide and a background sea of internal waves initialized as the

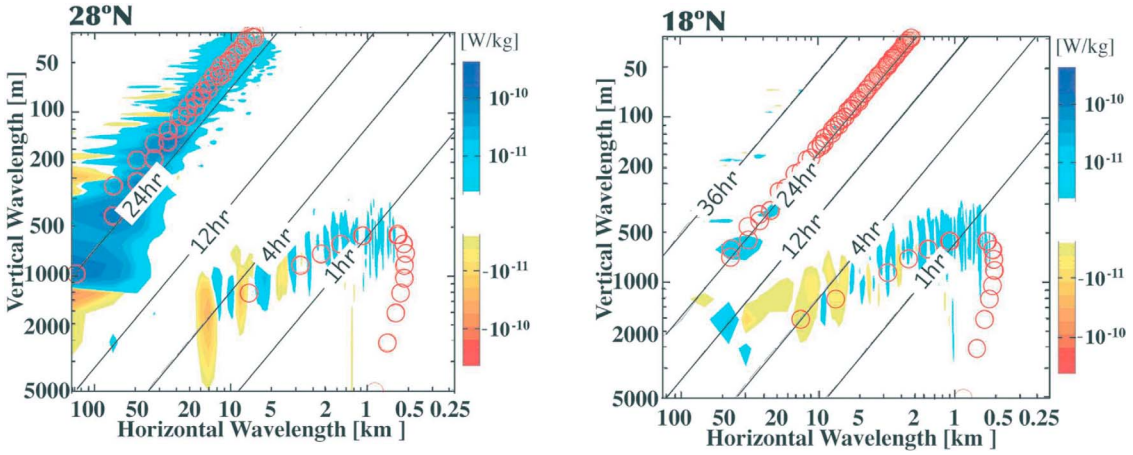

Figure 39. Nonlinear energy transfer rates from the lowest vertical wavenumber M_2 internal tide, with blue shades representing energy transfer from the tide to the background wavefield [*Furuichi et al.*, 2005]. The red circles depict the PSI (top left) and ID (bottom right) resonant curves. Diagonal lines are curves of constant wave period.

GM spectrum. They find an energy loss from the tide to the high-frequency field along the ID resonance curve at relatively high frequencies and an energy gain by the tide from the high-frequency field along the ID resonance curve at relatively low frequencies (small-scale separations) (Figure 39).

[168] Such a pattern of gain and loss is consistent with the midfrequency dip being a product of nonlinear interactions with the tide, as conjectured by *Levine* [2002]. The essential question is whether this energy loss along the ID resonance curve is sufficiently large in comparison to other effects.

5.1.2.3. The Dip: Departure From Scale Invariance

[169] If the pattern of loss and gain in Figure 38a is time stepped in the radiation balance equation, it will, at least initially, tend to result in a pattern resembling the midfrequency dip (e.g., Figure 13). Much depends upon the magnitude and direction of nonlinear transports and distribution of sources within the spectral domain and along the spectral boundaries. It would help to understand how the midfrequency dip is geographically distributed and related to power law combinations in order to understand whether the midfrequency dip results from nonlinearity.

5.1.3. Resonance Broadening and Coordinate Representations

[170] Numerical evaluations of (37) (Figure 38) suggest that neither GM76 nor the Sargasso Sea spectrum is a stationary state, and this contradicts our hypothesis that the observed spectra are in approximate equilibrium. A distinct possibility is that since normalized Boltzman rates for that calculation are $O(1)$, the character of the interaction is altered by nonresonant interactions. We further address this issue in sections 5.1.3.1–5.1.3.4.

5.1.3.1. Representation Dependences

[171] The issue of representation- (coordinate-) dependent differences arises naturally in nonlinear problems. Here it implies a question of whether a statistically stationary state in one coordinate system similarly represents a statistically stationary state in another.

[172] Kinetic equations have been derived in Eulerian, isopycnal, and Lagrangian coordinate systems. *Lvov et al.* [2011] find that Eulerian, isopycnal, and Lagrangian coordinate matrix elements in the hydrostatic, nonrotating $f^2 \ll \sigma^2 \ll N^2$ limit are equivalent on the resonant manifold. With rotation, comparisons are restricted to the isopycnal coordinate formulation of *Lvov and Tabak* [2004] and the Lagrangian coordinate formulation of *Olbers* [1973] and *McComas* [1975]. Strikingly, the $f \neq 0$, hydrostatic resonant expressions are also equivalent. Thus, representation-dependent differences are not apparent at the level of the RIA.

[173] Some physical sense can be made by noting that the resonant interaction approximation assumes, perforce, an expansion in terms of a nonadvected wavefield, with linear dispersion relation (2). It is a description of the wavefield as a system of coupled oscillators with distinct resonance conditions.

[174] Nonresonant kinetic equations are limited to an isopycnal coordinate representation. The isopycnal Hamiltonians given by *Lvov and Tabak* [2001, 2004] are explicitly expressed in terms of the the generalized coordinates and momenta. The generalized coordinates and momenta are implicit functions in the Lagrangian coordinate system formulations of *Olbers* [1976], *McComas and Bretherton* [1977], and *Pomphrey et al.* [1980] and the Eulerian coordinate system formulation of *Voronovich* [1979]. An implicit representation requires an expansion in powers of small fluid parcel displacements in addition to an assumption of weak nonlinearity. This small-amplitude assumption represents an unconstrained approximation whose domain of validity vis-á-vis the assumption of weak nonlinearity is not well defined [*Müller et al.*, 1986]. This matters when the resonances are broadened (section 5.1.3.2). In contrast, derivation of a kinetic equation using the *Lvov and Tabak* [2004] isopycnal Hamiltonian requires only an assumption of weak nonlinearity.

[175] The next level of approximation to the kinetic equation assumes that wave amplitudes vary in time, $a = a(\tau)$,

and the energy conserving delta functions in (37), $\delta(\sigma_{\mathbf{p}} - \sigma_{\mathbf{p}1} - \sigma_{\mathbf{p}2})$, consequently need to be "broadened" to take near-resonant interactions into account: When the resonant kinetic equation is derived, it is assumed that the amplitude of each plane wave is constant in time or, in other words, that the lifetime of a single plane wave is infinite. The resulting kinetic equation nevertheless predicts that the wave amplitude changes. For small levels of nonlinearity this distinction is not significant, and resonant kinetic equation constitutes a self-consistent description. For larger values of nonlinearity this is no longer the case, and the wave lifetime is finite and amplitude changes need to be taken into account. A mathematical interpretation is that resonance broadening represents a bandwidth $\Delta\sigma$ connected to the temporal localization through a Fourier uncertainty principle; that is, the product of wave lifetime τ and bandwidth $\Delta\sigma$ is given by $\tau\Delta\sigma = 2\pi$. This effect is larger for stronger levels of the normalized Boltzman rate (48). Section 5.1.3.2 describes attempts to incorporate resonance broadening effects into the kinetic equation.

5.1.3.2. Renormalization of the Kinetic Equation

[176] Inclusion of resonance broadening requires a renormalization of the kinetic equation (37). *DeWitt and Wright* [1982, 1984] tackle this starting from the Lagrangian of *Olbers* [1976] and carrying forward their calculations in the context of the direct interaction approximation (DIA). Their nominally finite amplitude analysis still retains the small-amplitude approximation inherent in the Lagrangian formulation. *Carnevale and Frederiksen* [1983] begin from the Eulerian equations of motion to derive the DIA closure equations for internal waves in two dimensions and without rotation through the application of renormalization theories originally formulated for quantum and classical statistical field theory. A similar tack is pursued by *Lvov et al.* [1997], and a general formulation for a three-wave system is given in terms of a Hamiltonian representation. There the Wyld diagrammatic technique adapted for the statistical description of a wave interaction system was used. This approach allows the Dyson-Wyld resummation of the reducible infinite class of diagrams, which presents certain parts of the nonlinear interactions as effectively being linear on average. As a result, off-resonant interactions can effectively contribute to long-time statistical averages. This result is obtained by analytical resummation of the infinite diagrammatic series for the Green's function and double correlator. This result is given by

$$\begin{aligned}\frac{dn_{\mathbf{p}}}{dt} = {} & 4\int \left|V^{\mathbf{p}}_{\mathbf{p}_1,\mathbf{p}_2}\right|^2 f_{p12}\mathcal{F}(\mathbf{p}-\mathbf{p}_1-\mathbf{p}_2)d^3\mathbf{p}_1 d^3\mathbf{p}_2 \\ & - 4\int \left|V^{\mathbf{p}_1}_{\mathbf{p}_2,\mathbf{p}}\right|^2 f_{12p}\mathcal{F}(\mathbf{p}_1-\mathbf{p}_2-\mathbf{p})d^3\mathbf{p}_1 d^3\mathbf{p}_2 \\ & - 4\int \left|V^{\mathbf{p}_2}_{\mathbf{p},\mathbf{p}_1}\right|^2 f_{2p1}\mathcal{F}(\mathbf{p}_2-\mathbf{p}-\mathbf{p}_1)d^3\mathbf{p}_1 d^3\mathbf{p}_2, \end{aligned} \tag{59}$$

with $\mathcal{F}(\mathbf{q}) = \delta_{\mathbf{q}}\mathcal{L}(\sigma_{\mathbf{q}})$. Here $\mathcal{L}$ is defined as

$$\mathcal{L}(\Delta\sigma) = \frac{\Gamma_{k12}}{(\Delta\sigma)^2 + \Gamma_{k12}^2}, \tag{60}$$

where Γ_{k12} is the total broadening of each particular resonance and $\Delta\sigma$ represents the residual $\Delta\sigma = \sigma_{\mathbf{p}} - \sigma_{\mathbf{p}1} - \sigma_{\mathbf{p}2}$, etc.

[177] The width of the resonance Γ_{k12} in (60) is given by

$$\Gamma_{k12} = \gamma_{\mathbf{p}} + \gamma_{\mathbf{p}_1} + \gamma_{\mathbf{p}_2}.$$

It means that the total resonance broadening is the sum of individual frequency broadening and thus can be seen as the "triad interaction" frequency.

[178] The single-frequency renormalization is calculated self-consistently from

$$\begin{aligned}\gamma_{\mathbf{p}} = {} & 4\int \left|V^{\mathbf{p}}_{\mathbf{p}_1,\mathbf{p}_2}\right|^2 (n_{\mathbf{p}_1} + n_{\mathbf{p}_2})\mathcal{F}(\mathbf{p}-\mathbf{p}_1-\mathbf{p}_2)d\mathbf{p}_1 d\mathbf{p}_2 \\ & - 4\int \left|V^{\mathbf{p}_1}_{\mathbf{p}_2,\mathbf{p}}\right|^2 (n_{\mathbf{p}_2} - n_{\mathbf{p}_1})\mathcal{F}(\mathbf{p}_1-\mathbf{p}_2-\mathbf{p})d\mathbf{p}_1 d\mathbf{p}_2 \\ & - 4\int \left|V^{\mathbf{p}_2}_{\mathbf{p},\mathbf{p}_1}\right|^2 (n_{\mathbf{p}_1} - n_{\mathbf{p}_2})\mathcal{F}(\mathbf{p}_2-\mathbf{p}-\mathbf{p}_1)d\mathbf{p}_1 d\mathbf{p}_2. \end{aligned} \tag{61}$$

Note that if the nonlinear frequency renormalization tends to zero, i.e., $\Gamma_{k12} \to 0$, $\mathcal{L}$ reduces to the delta function

$$\lim_{\Gamma_{k12}\to 0} \mathcal{L}(\Delta\sigma) = \pi\delta(\Delta\sigma).$$

In the limit of no broadening (59) reduces to (37).

[179] A self-consistent estimate of $\gamma_{\mathbf{p}}$ requires the iterative solution of (59) and (61) over the entire field: the width of resonance (61) depends on the lifetime of an individual wave (from (59)), which in turn depends on the width of resonance (60). The result is a numerically intensive computation which has yet to be undertaken. Instead, *Lvov et al.* [2011] make the uncontrolled approximation that

$$\gamma_{\mathbf{p}} = \varepsilon\sigma_{\mathbf{p}}, \tag{62}$$

with ε taken as 10^{-3} and larger.

[180] The patterns of gain and loss at $\varepsilon = 1 \times 10^{-3}$ (Figure 40) are quantitatively similar to previously published results including only resonant interactions [e.g., *Olbers*, 1976]. Minimal variation is noted in evaluations using $\varepsilon = 1 \times 10^{-3}$ and $\varepsilon = 1 \times 10^{-2}$, implying that the $\varepsilon = 1 \times 10^{-3}$ evaluations represent the resonant interaction limit. Normalized Boltzman rates are $O(1)$ at high wavenumber and in particular within the high-frequency part of the spectral domain which is nominally a stationary state in the ID approximation. *Lvov et al.* [2011] find that normalized Boltzman rates are reduced by factors of 2–3 with $\varepsilon = 0.5$ [see *Lvov et al.*, 2011, Figure 5]. Here we present results for which it is difficult to claim that resonance broadening significantly decreases the normalized Boltzman rate (Figure 40). The difference between results presented by *Lvov et al.* [2011] and in Figure 40 is that *Lvov et al.* [2011] extend the GM76 spectrum to $2m_c$, zeroing the spectrum at higher vertical wavenumber. Here we roll off the GM76 spectrum as GM76 $\times\, m_c/m$ for $m > m_c$, zeroing the spectrum only for $m > 8m_c$. We regard this as being a much more realistic characterization of the observations. Clearly, the numerical

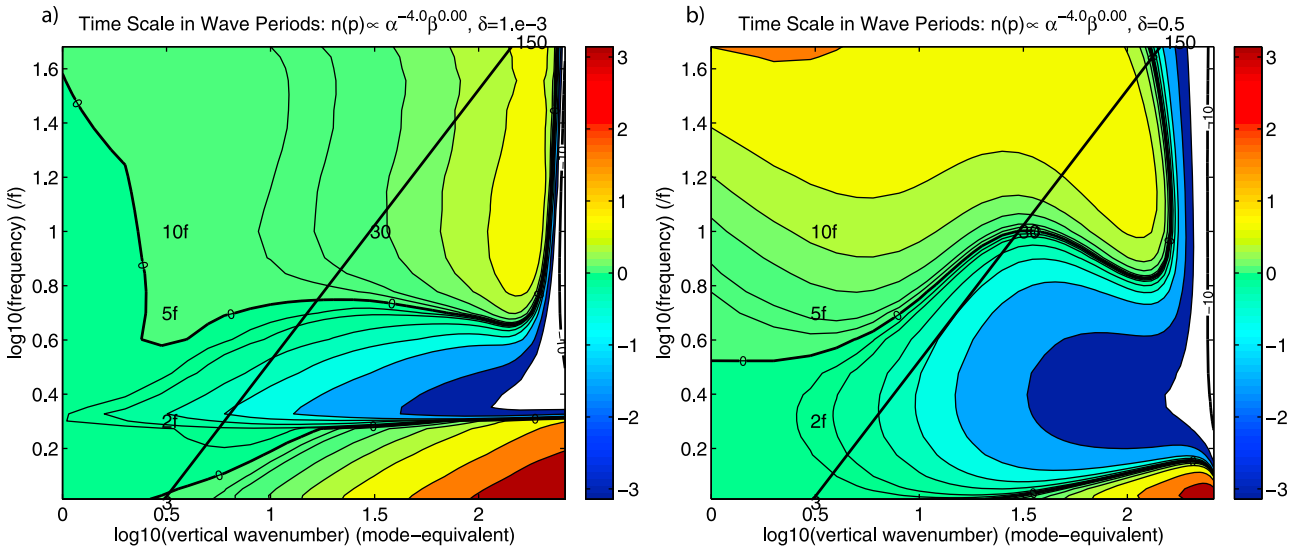

Figure 40. Normalized Boltzman rates (48) for the GM76 spectrum calculated via (59) using the *Lvov and Tabak* [2004] matrix elements with (a) $\delta = 10^{-3}$ and (b) $\delta = 5 \times 10^{-1}$ [*Lvov et al.*, 2011]. A value of $\delta = 10^{-3}$ represents the resonant interaction limit. The spectra have been extended beyond $m > m_c$ by rolling off the spectrum as GM $\times$ m_c/m.

evaluations are sensitive to the treatment of the spectral boundaries. Experimentation suggests that numerical evaluations of the broadened kinetic equation are also sensitive to the functional representation of $\gamma_{\mathbf{p}}$ other than (62).

[181] The iterative calculation needs to be carried out in order to address whether the patterns in equation (43) associated with the induced diffusion mechanism (Figure 37) are more than simply fortuitous.

5.1.3.3. Ray Tracing Models

[182] The interpretation offered immediately above is one that attempts to define the breadth of the resonance associated with a forced-damped system of weakly coupled oscillators, in which "forcing" and "damping" can be construed as the scattering of energy into and out of ($\mathbf{p}$, σ). An alternative description is to view the wavefield as a collection of wave packets, i.e., as particles. In this particle perspective, the time evolution of a wave packet (a "test" wave) is proportional to gradients of the Doppler shift as one evaluates the evolution of the wavenumber, frequency, and amplitude of the wave packet along its trajectory, in contrast to the coupled oscillator construct that assumes only an amplitude modulation. These ray methods do not make a weak interaction assumption. They do, however, make scale separation and small-amplitude assumptions.

[183] The ray equations [*Witham*, 1974] are

$$\mathcal{R} \equiv \frac{d\mathbf{p}}{dt} = -\nabla_{\mathbf{r}}\omega - (\nabla_{\mathbf{r}}\overline{\mathbf{u}}) \cdot \mathbf{p} \tag{63}$$

for the time evolution of a wave vector following a wave packet and

$$\frac{d\mathbf{r}}{dt} = \overline{\mathbf{u}} + \nabla_{\mathbf{p}}\omega \tag{64}$$

for the position of the wave packet, which varies as the sum of advection plus group velocity. The background velocity $\overline{\mathbf{u}}$ is assumed to be slowly varying in comparison to the wave phase and is treated as time-dependent stochastic realizations based upon the GM model in this wave-wave interaction problem. The intrinsic frequency

$$\omega = \sigma - \mathbf{p} \cdot \overline{\mathbf{u}} \tag{65}$$

is given by a linear dispersion relation (2). The amplitude of the wave packet is assumed to be small and obeys an action conservation principle:

$$\frac{\partial n(\mathbf{p})}{\partial t} + \nabla_{\mathbf{r}} \cdot (\overline{\mathbf{u}} + \mathbf{C}_{\mathbf{g}}) n(\mathbf{p}) + \nabla_{\mathbf{p}} \cdot \mathcal{R} n(\mathbf{p}) = 0. \tag{66}$$

A rigorous derivation [*Witham*, 1974] is based upon the concept of phase ($\mathbf{p} \cdot \mathbf{r} - \sigma t$) conservation for a single wave packet rather than energy ($\Sigma_{i=1}^{3} \sigma_i \dot{n}_i = 0$) and momentum ($\Sigma_{i=1}^{3} \mathbf{p}_i \dot{n}_i = 0$) conservation of a triad system. The extent to which the dynamics inherent in the kinetic equation (59) are captured by the restricted description (63), (64), and (66) has not been fully elucidated.

[184] The ray equations do not constitute a transport representation in (23), which attempts to describe the average evolution of a field, rather than the evolution of a single wave packet. To this end, *Flatté et al.* [1985] report that test wave spectra exhibit a tendency to relax to one-dimensional vertical wavenumber spectra proportional to m^{-2} (GM76) and one-dimensional horizontal wavenumber spectra proportional to $k_h^{1/2}$ times GM76, independent of whether the background was consistent with the GM model. This is the solution to kinetic equation (37) defined by *Pelinovskii and Raevsky* [1977] and that which appears in the dimensional

analysis by *Polzin* [2004a]. The model diagnostics of *Flatté et al.* [1985] indicate action transport to higher frequency, which is inconsistent with the induced diffusion model of action transport to higher vertical wavenumber without transport in horizontal wavenumber, i.e., transport to lower frequency. These tendencies are captured by a cascade representation of T_r given by *Polzin* [2004a]:

$$\omega T_r(\mathbf{p}) = \frac{\partial}{\partial m}\left[0.2m^4N^{-1}\left[\frac{\omega^2 - f^2}{N^2 - \omega^2}\right]^{1/2} E(m)E(\mathbf{p})\right]. \quad (67)$$

The cascade closure has been used in combination with PSI forcing of the inertial field (Polzin, manuscript in preparation, 2011) to obtain a link between power law dependencies in the vertical wavenumber and frequency domains. This closure is also used to discuss the near-boundary decay problem presented by *Polzin* [2004b]. It is equivalent to the ray tracing based formulas employed in diagnostic studies of dissipation parameterizations [*Gregg*, 1989; *Polzin et al.*, 1995; *Gregg et al.*, 2003].

[185] The most important point is the frequency domain weighting of energy transports to small vertical scales in (67):

$$\int_f^N \sigma T_r(m,\sigma)d\sigma \propto \int_f^N \left[\frac{\omega^2 - f^2}{N^2 - \omega^2}\right]^{1/2} E(\omega)d\omega. \quad (68)$$

Despite the small spectral density at high frequency, high frequencies make a significant contribution to the total spectral transports.

5.1.3.4. Numerical Simulations

[186] Direct numerical simulations of the equations of motion are not limited by the dynamical assumptions inherent in either the weakly nonlinear or eikonal representations. They are, however, subject to computational restrictions.

[187] *Winters and D'Asaro* [1997] present spin-down simulations based upon the GM76 spectrum with varying amplitude. They regard their results as being consistent with the magnitude ($\epsilon = 7 \times 10^{-10}$ W kg^{-1}) and scaling of *Gregg* [1989], $\epsilon \sim E^2N^2$. *Polzin et al.* [1995] and *Polzin* [2004a] argue that theoretical estimates based upon the eikonal model of *Henyey et al.* [1986] and the dynamic balance of *McComas and Müller* [1981b] are indistinguishable from the observational results. Thus, both observations, *Henyey et al.* [1986], *McComas and Müller* [1981b], and *Winters and D'Asaro* [1997] are consistent. The domain considered by *Winters and D'Asaro* [1997] consists of a rectangular box $80 \times 10 \times 1$ km on a side with resolved wavelengths of 1 km in the horizontal and 50 m in the vertical. Note that this domain does not include regions in Figure 38 exhibiting large values of the normalized Boltzman rate. Interactions in the resolved domain may be dominated by PSI transfers as discussed by *McComas and Müller* [1981b].

[188] Forced nonrotating simulations are presented by *Furue* [2003]. The computational domain is a box of horizontal size $100 \times 100 \times 128$ m height. The forcing is isotropic in wavenumber and peaks at a horizontal wavelength of 25 m. The forcing is controlled so that amplitudes are consistent with GM76 and the resulting dissipation is a significant fraction of that associated with GM76. While we are uncertain about how to relate these forced simulations to the wave-wave interaction problem, we believe that finding significant dissipation at high frequencies is credible (see (67) and section 5.4.2). Also notable are findings that wavenumber-local interactions dominate the transfers and that energy transport to higher horizontal wavenumbers (section 5.1.1.5) is a robust feature of the simulations whereas energy transport in vertical wavenumber is strongly dependent upon spectral shape.

[189] Quantitative estimates of spectral transports in high resolution and realistically forced direct numerical simulations is a high priority, especially in conjunction with efforts to understand the limitations of a broadened kinetic equation (59).

5.1.4. Does the Continuum Exist?

[190] Eulerian frequency spectra at high vertical wavenumber are contaminated by vertical Doppler shifting: near-inertial frequency energy is Doppler shifted to higher frequency at approximately the same vertical wavelength. High-frequency, small-horizontal-scale internal waves are also easily advected past a similar Eulerian observer by the horizontal velocity of near-inertial waves. Such differences motivate our concern with different coordinate systems in section 5.1.3.1.

[191] *Pinkel* [2008] posits that the apparently continuous wavenumber-frequency spectrum at high vertical wavenumber results from the advective smearing of variance contained in a few discrete spectral lines. A "simple" model is introduced to quantify the effects of lateral advection and both random and deterministic vertical advection on these spectral lines. Two data sets, including one from the Arctic (the Surface Heat Budget of the Arctic (SHEBA) (Figure 41)) were used to demonstrate the model.

[192] Model implementation includes arbitrary choices of functional forms for lag coherence estimates and choosing model parameters to maximize the high-frequency shear variance which would be interpreted as resulting from Doppler smearing. Further observational constraints, such as requiring the vertical displacement spectrum to be consistent with the observations, could have been implemented. As presented, the model's vertical displacement spectrum appears to be about a factor of 2 larger than expected (Figure 41).

[193] The SHEBA spectrum is quite different from the AIWEX spectrum. The SHEBA frequency domain power laws are much steeper. This is possibly related to time dependence in forcing or nonlinearity (the SHEBA spectrum was obtained in August–September 1998, AIWEX was conducted in March–May 1985, and *Pinkel* [2005] notes significant temporal variability in the stratification with the recent buildup of a seasonal thermocline prior to the SHEBA observations) and/or to spatial variability (thereported SHEBA observations were obtained atop the continental shelf, whereas the AIWEX data represent deep ocean

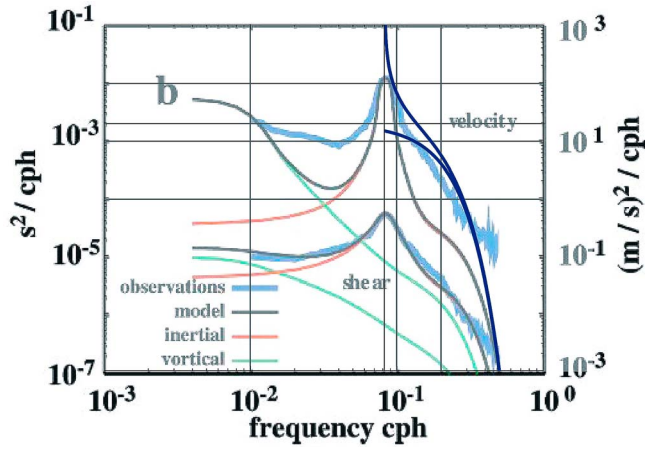

Figure 41. Figure 4b of *Pinkel* [2008] with a displacement variance overlay and associated velocity spectrum, assuming the Gaussian distribution given by *Pinkel* [2008] with 2 h lag correlation and 1.25 m^2 displacement variance. The associated velocity spectrum (upper curve within the overlay) lies above the observed velocity spectrum. A buoyancy frequency of $N = 6$ cph has been assumed.

conditions). The AIWEX data [*Levine*, 1990] appear to argue strongly for a high-frequency, high-wavenumber continuum.

[194] While there assuredly is some contamination of the high vertical wavenumber continuum by Doppler shifting, the goodness of fit given by *Pinkel* [2008] cannot be interpreted as evidence for the nonexistence of the continuum. If robust, the goodness of fit simply implies that the velocity observations are consistent with the proposed model. Further consistency tests based upon both density and velocity fields could demonstrate otherwise. Note that the 2-D PATCHEX and SWAPP spectral parameters (section 3.3.5) were extracted from E_p rather than E_k spectra in an attempt to limit the effects of Doppler shifting and instrument response functions.

5.1.5. A Summary and Future Challenges

[195] The characterization of nonlinear interactions is a complicated process, and therefore, reductions to simplified forms for various limiting cases are highly desirable. The reduction of the kinetic equation in the ID limit to a Fokker-Plank equation in vertical wavenumber is fundamental in this regard: the stationary states of this equation collapse much of the observed variability in the spectral parameters (a, b) (Figure 37). There are, however, significant questions regarding the validity of the underlying assumption of resonant interactions, especially in the ID limit at small vertical scales, that prompt one to wonder if the pattern match is merely fortuitous. At these small vertical scales, diagnostic studies that compare simplified representations of the downscale transport with estimates of turbulent dissipation often settle upon the ray tracing model (67) as providing the theoretical framework for the fine-scale internal wavefield. However, the simplified representations derived within the RIA provide predictions that are similar both in magnitude and in scaling [*Polzin*, 2004b]. Thus, one might be prompted to suggest that such misgivings are simply due to offenses against one's theoretical sensibilities.

[196] There is, however, a very substantive issue that cries out for explanation. Associated with the ID mechanism and $b > 0$ are energy transports to higher vertical wavenumber and lower frequency. A stationary state under the ID mechanism and $b > 0$ thus requires either an external energy source at high frequencies (sections 5.2 and 5.3), a change in spectral transports associated with finite amplitude effects that acts to reduce transports through the frequency domain (section 5.1.3), a change in the character of spectral transports associated with local interactions neglected in the ID approximation (section 5.1.1.5), or an effective source associated with nonhydrostatic effects. Our knowledge of high-frequency sources is incomplete, studies of resonance broadening are limited by the difficulty of obtaining an iterative solution to (59) and (61), our numerical result concerning local transfers in the horizontal wavenumber domain requires an analytic characterization, and numerical evaluations that have included nonhydrostatic effects [*Olbers*, 1976] are silent on this issue.

5.2. Wave Mean Interactions

5.2.1. Spectral Patterns

[197] Much of the analysis in section 5.1 was predicated upon the assumption of an inertial subrange: there exists a range of wavenumbers and frequencies removed from the influence of forcing and dissipation, and far from the characteristic spatial and temporal scales of the system, so that the spectrum can be characterized as being scale invariant. We have noted the difficulties for this scenario with respect to the importance of extreme-scale separated interactions in section 5.1.1. Here we note that wave mean interactions pose a special problem for the scale-invariant solution in that wave mean interactions can be cast as a source representation $S_o(\mathbf{p})$ acting throughout the spectral and spatial domains rather than being located at the boundaries.

[198] A large body of work focuses upon the simplified cases of waves interacting with parallel shear flows [*Molemaker et al.*, 2005; *Ruddick*, 1980] or vortices [*Kunze*, 1985], i.e., symmetric background flows. This conceptual paradigm may be made much more general and useful by allowing the background flow to have spatial gradients in both horizontal coordinates. While the assumption of a spatially symmetric background flow makes for a more tractable theoretical problem, it also introduces a hidden constraint in which the vertical flux of streamwise pseudomomentum is nondivergent except at a critical layer. In the general problem of internal waves interacting with a mesoscale eddy field having three-dimensional structure, a wave packet can freely exchange wave pseudomomentum for eddy potential vorticity [*Bühler and McIntyre*, 2005]. This is restricted from happening in a symmetric background flow.

[199] The essence of the interaction in three dimensions is the filamentation of an internal wave by the horizontal rate of strain and vertical propagation into a critical layer. This

can be directly seen from a linearized internal wave energy equation for wave propagation in a quasigeostrophic background [*Polzin*, 2010]:

$$\left(\frac{\partial}{\partial t}+\overline{u}\cdot\nabla_h\right)\left(E_k+E_p\right)+\nabla\cdot\overline{\pi''\mathbf{u}''}=-\left[\overline{u''u''}-\overline{v''v''}\right]S_n/2 - \overline{u''v''}S_s-\left[\overline{u''w''}-\frac{f}{N^2}\overline{b''v''}\right]\overline{u}_z-\left[\overline{v''w''}+\frac{f}{N^2}\overline{b''u''}\right]\overline{v}_z, \quad (69)$$

with kinetic ($E_k = (u''^2 + v''^2 + w''^2)/2$) and potential ($E_p = (N^{-2}\, b''^2)/2$) energies. Temporal variability and advection of internal wave energy by the geostrophic velocity field are balanced by wave propagation and energy exchanges between the quasigeostrophic and internal wave fields. Nonlinearity and dissipation are assumed to be higher-order effects. Spatial gradients of the vertical velocity $\overline{w}$ do not appear as $\overline{w}_z$ is small (order Rossby number squared) in the quasigeostrophic approximation. The thermal wind relation has been invoked to cast the vertical Reynolds stress and horizontal buoyancy flux as the rate of work by an effective vertical stress acting on the vertical gradient of horizontal momentum. These two terms in the effective stress will cancel each other in the limit that $\omega \to f$ [*Ruddick and Joyce*, 1979]. Finally, $S_s \equiv \overline{v}_x + \overline{u}_y$ represents the shear component, and $S_n \equiv \overline{u}_x - \overline{v}_y$ represents the normal component of the rate of strain tensor. In the limit of an extreme-scale separation between wave and background flow, horizontal group velocities are small, and an internal wave behaves much like a passive tracer [*Bühler and McIntyre*, 2005; *Polzin*, 2008] as the rate of strain cascades the wave to higher horizontal wavenumber. As it does so, the horizontal components of the internal wave stress result in work against the mean flow gradients and gain of wave energy. In the situation in which a wave is propagating vertically into a critical layer, the vertical stresses are such that the wave loses energy to the eddy field.

[200] The coupling of mesoscale eddies and internal waves and construction of a $S_o(\mathbf{p})$ representation was explicitly addressed by *Müller* [1976]. *Müller*'s [1976] analysis was based upon a perturbation expansion of the internal wave radiation balance equation (23). Internal waves were assumed to be of small amplitude and have small spatial scales relative to a geostrophically balanced background that evolves over a much longer time scale. Spatial gradients in the background were assumed to be sufficiently weak that wave mean interactions affect wave propagation only through an advective Doppler shift. In this limit of small-amplitude waves interacting with a quasi-qeostrophic eddy field, exchanges of energy, momentum, and vorticity are reversible unless an external force is invoked which acts in phase on the wave mean induced perturbations. In the work by *Müller* [1976], the external force is identified as the tendency for nonlinear interactions to relax the wave mean induced perturbations to an isotropic state. It is this relaxation that creates a permanent exchange of pseudomomentum for potential vorticity. In order to close the problem, *Müller* [1976] invoked a relaxation time approximation and further assumed the relaxation time scale to be constant. Estimates of the eddy–internal wave coupling strength were not supported by observations [*Ruddick and Joyce*, 1979; *Brown and Owens*, 1981], and this line of investigation was dropped. With regards to the straw man in Figure 34, the consequence is that wave mean interactions are not available as a source to supply energy depleted by PSI transfers.

[201] The work by *Müller* [1976] was written from the perspective that the thermocline is characterized by a diapycnal diffusivity of $K_\rho = 1 \times 10^{-4}$ m^2 s^{-1}, which implies a time scale of 5–10 days for nonlinear interactions to drain energy out of the background internal wavefield. Several decades of research have since demonstrated that the background diffusivity is $K_\rho = 5 \times 10^{-6}$ m^2 s^{-1}, with corresponding time scale of 50–100 days. The difference is crucial as Müller assumed that the eddy–internal wave interaction was local in the spatial domain. With O(50–100) day relaxation time scales, wave propagation effects become important: larger-scale internal waves can propagate through an eddy-wave interaction event with minimal permanent exchange of pseudomomentum and vorticity. Fortunately, *Müller* [1976] tells us how to account for such propagation effects. Accounting for propagation effects and use of a more realistic prescription of the nonlinear time scale returns estimates of the coupling that are in much better agreement with the observations (K. L. Polzin, Mesoscale eddy–internal wave coupling. III. The end of the enstrophy cascade and implications for the fast manifold–slow manifold debate, manuscript in preparation, 2011a).

[202] The radiation balance equation source function,

$$\sigma S_o(\mathbf{p}) = S_o^h + S_o^v, \quad (70)$$

can be characterized with the following relaxation time scale formulas:

$$S_o^h(\sigma,m) = -\frac{1}{8}\frac{\sigma^2-f^2}{\sigma^2}\frac{m^2}{m^2+k_h^2}\frac{\sigma k_h \tau_R}{1+\left(\tau_R/\tau_p\right)^2} \times \frac{\partial n_3^{(0)}}{\partial k_h}\left(\overline{u}_x^2+\overline{u}_y^2+\overline{v}_x^2+\overline{v}_y^2\right) \quad (71)$$

$$S_o^v(\sigma,m) = \frac{1}{2}\frac{\sigma^2-f^2}{\sigma^2}\frac{\sigma k_h^2}{m}\frac{m^2}{m^2+k_h^2}\frac{\tau_R}{1+\left(\tau_R/\tau_p\right)^2} \times \frac{\partial n_3^{(0)}(k_h,m)}{\partial m}\left(\overline{u}_z^2+\overline{v}_z^2\right), \quad (72)$$

with relaxation time scale τ_R and propagation time scale (wave group velocity divided by eddy length scale) τ_p. Evaluations of the relaxation time scale formulas are presented in Figures 42 and 43. We use two spectra intended to mimic those at Site D (GM76) and the Sargasso Sea ((18) and (19) with ($s = 2$, $t = 2.3$, $j_* = 15$, $r = 0.8$, $q = 0.5$, $N = 2.6$ cph, $E = 0.7E^{\mathrm{GM}}$)). Mean flow gradient statistics are taken from the Local Dynamics Experiment (LDE) data [*Polzin*, 2010]: (H, L, $\overline{u}_z^2 + \overline{v}_z^2$, $\overline{u}_x^2 + \overline{u}_y^2 + \overline{v}_x^2 + \overline{v}_y^2$) = (700 m, 100 km, 4.1×10^{-8} s^{-2}, 5.8×10^{-12} s^{-2}). Preliminary estimates from Site D array data indicate that this is an appropriate char-

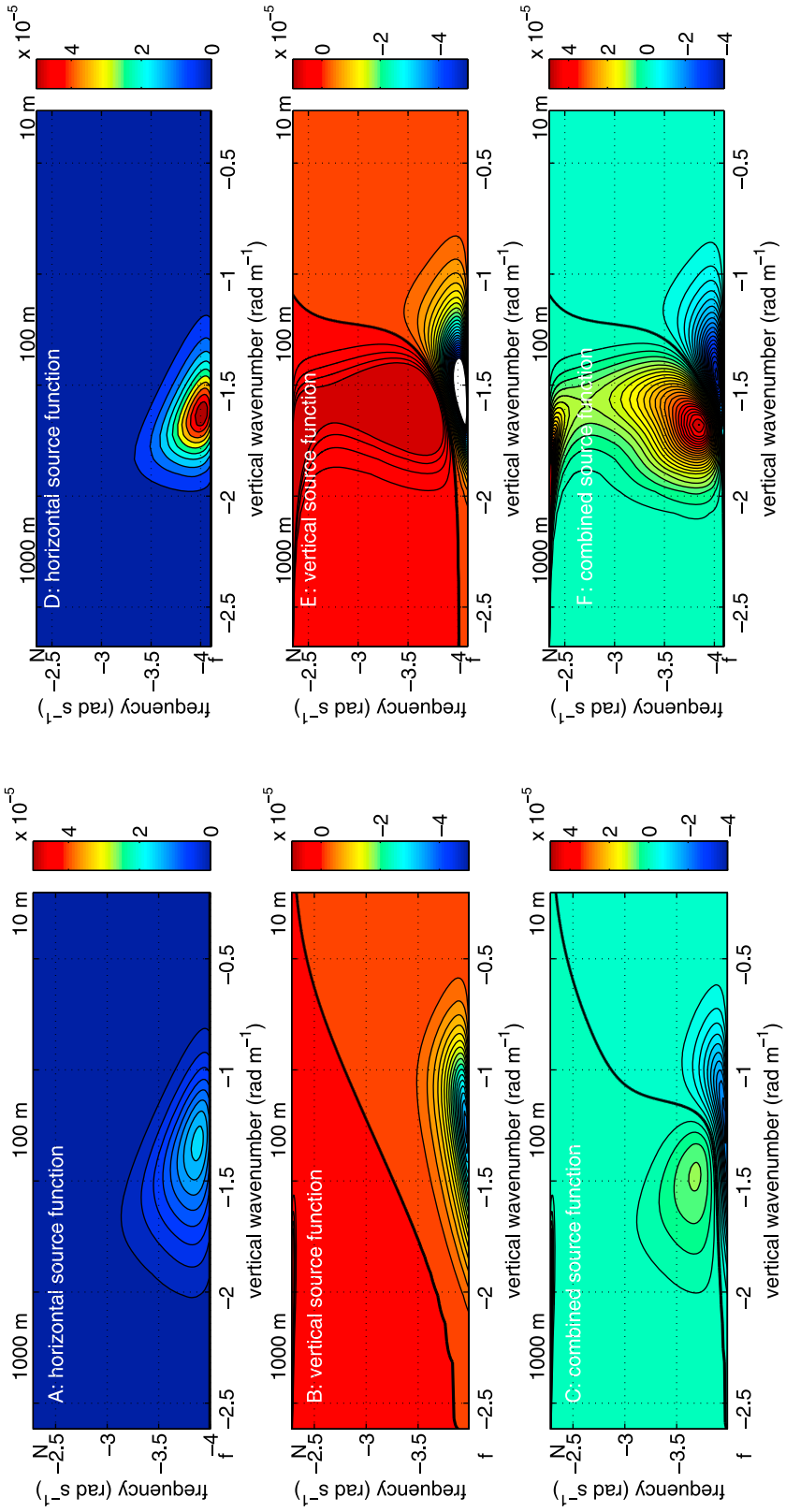

Figure 42. The spectral source functions defined in (71) and (72). (a–c) GM76 evaluations. (d–f) Source functions using a "Sargasso Sea" spectrum. Figures 42a and 42d represent the horizontal source functions, Figures 42b and 42e represent the vertical source functions, and Figures 42c and 42f represent combined source functions. The thick line separates positive source values from negative. Negative values of the source function are, effectively, energy sinks for the internal wavefield.

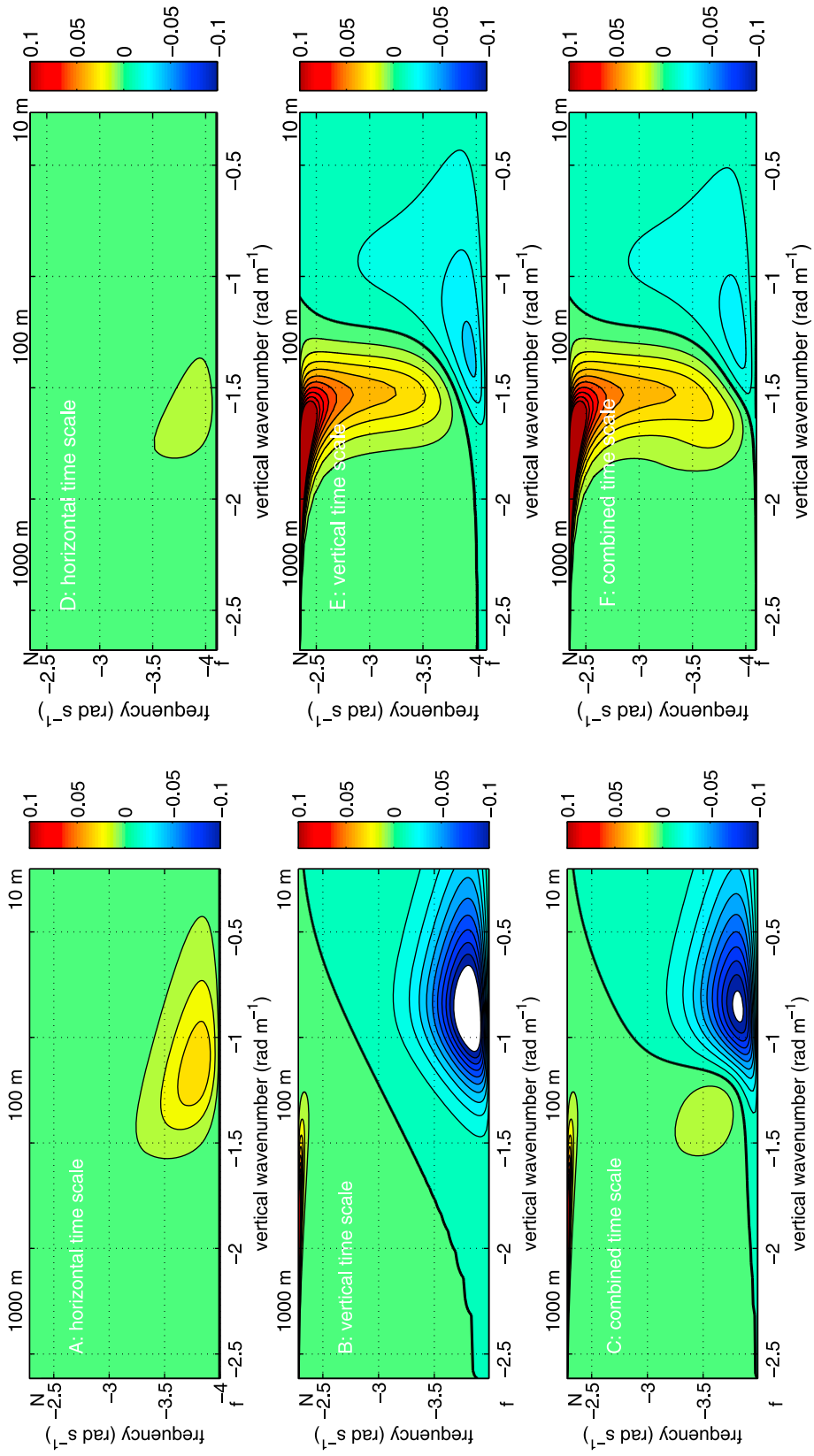

Figure 43. The spectral source functions appearing in Figure 42 but expressed as a normalized transfer rate $2\pi S_o(\sigma, m)/\sigma E(\sigma, m)$. This normalization permits a direct comparison with Figures 38 and 40. Contour intervals here are 0.01.

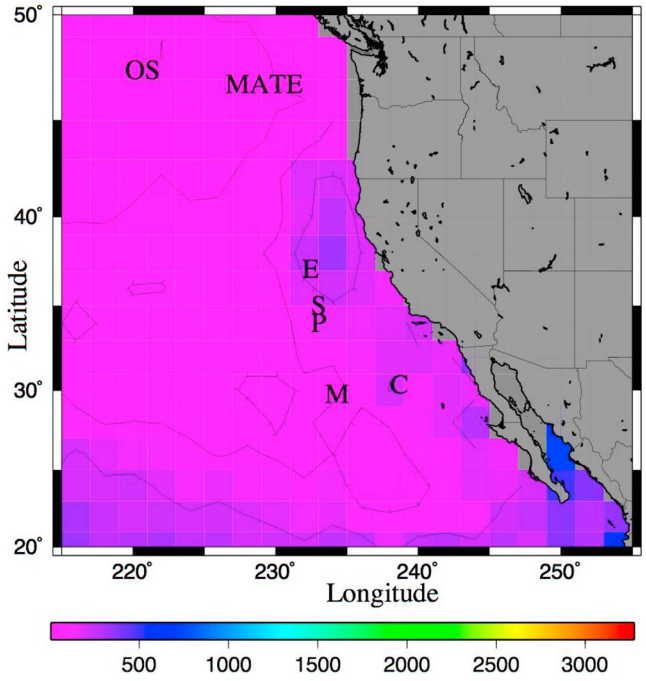

Figure 44. Western North Pacific surface eddy kinetic energy in units of 10^{-4} m^2 s^{-2}. Contour intervals are [50, 100, 200, 500, 1000, 2000] × 10^{-4} m^2 s^{-2}.

acterization there. The relaxation time scale is specified using (67).

[203] The coupling is a complicated function of the spectral parameters (spectral amplitude, high-wavenumber and high-frequency power law specifications, and low-wavenumber roll-off) and external parameters (i.e., mesoscale velocity gradient variances and characteristic spatial scales (Figures 44 and 45)). Without having executed a complete parameter regime survey, we rationalize the results as follows.

[204] In the continuum frequency band, differences between the vertical source functions for GM76 and the Sargasso Sea result from the GM76 3-D action spectrum having minimal gradients of action in the vertical wavenumber domain, i.e., $b = 0$. For $b \neq 0$, the zero-contour demarcating source-sink tendencies is dictated by m_*: larger vertical wavelengths are sources of energy for the internal wavefield. The magnitude of the positive region relative to the high-wavenumber negative region is dictated by the ratio of relaxation to propagation time scales, $\tau_r : \tau_p$. The possibility of a positive feedback mechanism dictating m_* is obvious.

[205] In the near-inertial band, vertical transfers are sinks and horizontal transfers are sources, consistent with a vertical critical layer and horizontal filamentation scenario. The net transfer obviously is a function of the horizontal versus vertical gradient variances of the mesoscale eddy field, i.e., its aspect ratio. The Sargasso Sea estimates imply an eddy aspect ratio slightly less than f/N, and this may be typical [*Arbic and*

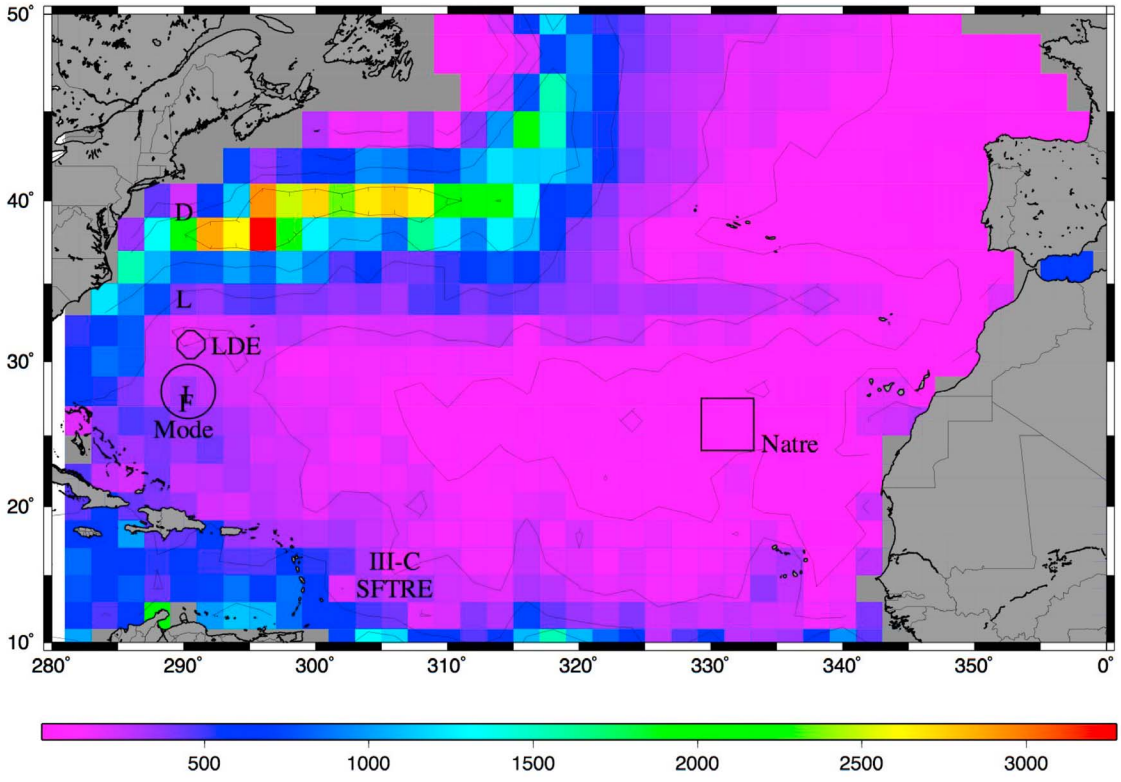

Figure 45. North Atlantic surface eddy kinetic energy in units of 10^{-4} m^2 s^{-2}. Contour intervals are [50, 100, 200, 500, 1000, 2000] × 10^{-4} m^2 s^{-2}.

TABLE 1. Estimates of Source Strengths[a]

Program	Latitude	Longitude	Mechanism	Start	Stop	Source Strength
LOTUS	34°N	70°W	wind work	May 1982	Oct 1982	1 mW m^{-2} × 50%
LDE	31°N	70°W	eddy-wave coupling	May 1978	Jul 1979	>0.4 mW m^{-2}
Mode	28°N	70°W	tide	Mar 1973	Jul 1973	300 W m^{-1}/700 km
FASINEX	27°N	70°W	wind work	Jan 1986	May 1986	0.4 mW m^{-2} × 50%
Subduction	25.5°N	29°W	wind work	Apr 1992	Oct 1992	0.05 mW m^{-2} × 50%
Subduction	25.5°N	29°W	tides	Apr 1992	Oct 1992	1 kW m^{-1}/1000 km
Site D	39°N	69°W	wind work	Nov 2001	Apr 2006	1.0 mW m^{-2} × 50%

[a]Best estimates of the internal wave source associated with wind work are a fraction (50%) of the wind work. The internal wave source associated with the decay of a low-mode tide is obtained by dividing the energy flux estimate by a length scale. Those length scales are ill constrained.

Flierl, 2004]. We have also included nonhydrostatic conditions in these calculations. There is a signature of a significant source at the buoyancy frequency in the vertical source function that is largest for $b \neq 0$. This could potentially resolve issues related to ID transfers requiring a high-frequency source in order to maintain a transport of action to high vertical wavenumber (section 5.1.1.4). Some skepticism is required: such dynamics will compete with turning point effects and questions of how to specify H in τ_p arise. Apart from the buoyancy frequency, note that these wave mean transfers are far too small to offset resonant wave-wave interactions: Compare Figure 38 with Figure 43.

5.2.2. Budgets

[206] Energy exchange between the mean and wave fields results from a stress-strain relation in the horizontal. Direct evaluation of the energy exchange using the PolyMode LDE current meter array data [*Polzin*, 2010] returns a transfer rate somewhat smaller than previously obtained [*Brown and Owens*, 1981], 4×10^{-10} W kg^{-1} at 825 m depth. If this value characterizes the thermocline region having a characteristic depth $H = 1000$ m, a net source strength of 0.4 mW m^{-2} can be anticipated (Table 1). This estimate may be biased low, however, as both vertical and horizontal velocity gradients increase toward the surface and the rate at which energy is transferred is proportional to the velocity gradient variances. The LDE was located at (31°N, 70°W), midway between LOTUS and FASINEX. The estimates of energy transfer through eddy–internal wave coupling at 825 m depth do not appear to explain the regional seasonal cycle of internal wave energy. There is, however, a seasonal cycle in upper ocean fronts associated with buoyancy forcing [e.g., *Weller*, 1991]. This upper ocean frontal regime is characterized by an $O(1)$ Froude (vertical gradient of horizontal velocity divided by buoyancy frequency) and Rossby (relative vorticity divided by f) number parameter regime [*Pollard and Regier*, 1992] which may support more efficient energy transfers than the quasi-geostrophic regime at the thermocline base.

5.3. Forcing

[207] The focus of sections 5.1 and 5.2 was the genesis of spectral structure. In sections 5.3–5.5 we focus more upon (1) whether the variability in spectral parameters represents the character of the forcing at the endpoints of the cascade-spectral boundaries and (2) whether the forcing is consistent with the direction and magnitude of energy transfers.

5.3.1. Near-Inertial Wave Generation by a Variable Wind Stress

[208] Work done by the wind in generating inertial frequency mixed layer motions has been the subject of several recent publications. Nearly global maps of this wind work using the *Pollard and Millard* [1970] damped slab model are presented by *Alford* [2003] and *Watanabe and Hibiya* [2002] (Figures 46 and 47). The slab model is highly idealized. Using observations of the upper ocean response to atmospheric forcing and a more sophisticated mixed layer model, *Plueddemann and Farrar* [2006] describe how the slab model tends to overestimate inertial frequency wind work by a factor of 2. Their estimates for the LOTUS, FASINEX, and Subduction field programs are given in Table 1. Similar estimates for Site D are presented by *Silverthorne and Toole* [2009].

[209] *Plueddemann and Farrar* [2006] also note that other modeling investigations [*Crawford and Large*, 1996; *Skyllingstad et al.*, 2000] imply that only a fraction of this

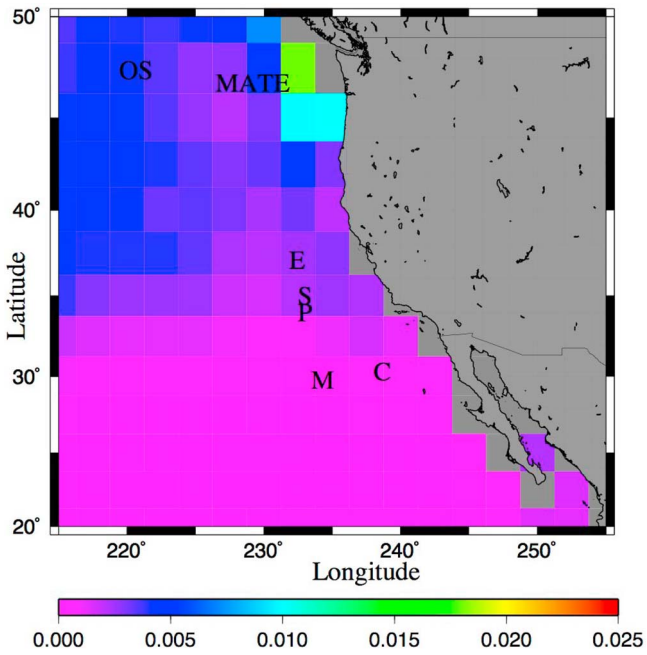

Figure 46. Power input by near-inertial winds to the oceanic mixed layer, in units of W m^{-2}, for the western North Pacific [*Alford*, 2003] (data from M. Alford, personal communication, 2008).

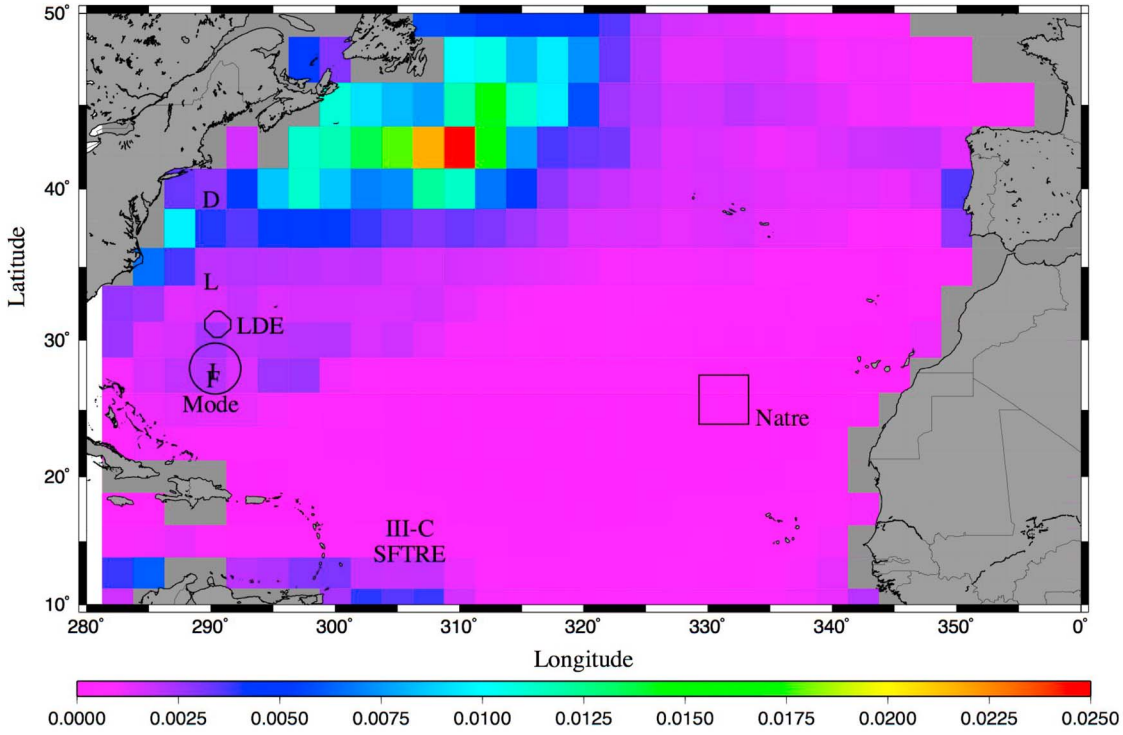

Figure 47. Power input by near-inertial winds to the oceanic mixed layer, in units of W m^{-2}, for the North Atlantic [*Alford*, 2003] (data from M. Alford, personal communication, 2008).

work (50%) may be available for near-inertial internal wave generation as the other part is lost to viscous dissipation in the mixed layer for the resonant forcing conditions that dominate the revised transfer estimates. "Best" estimates of source strength in Table 1 incorporate this dissipation.

[210] The aforementioned work concerns only getting inertial energy into the mixed layer. Radiation of this energy into the stratified interior can be represented by invoking a Fourier decomposition of the slab model and mapping onto the internal wavefield using a linear model that includes the variation of the Coriolis parameter with latitude [*D'Asaro*, 1995a]. There are, however, unresolved issues: the linear model underestimates the initial rate at which energy leaves the mixed layer by 20%–50% and cannot explain the evolution of the small vertical wavelength near-inertial field. Nonlinear interactions are held to be a primary candidate to explain the latter [*D'Asaro*, 1995b]. For further consideration of near-inertial motions see section 5.5.

5.3.2. Surface–Internal Wave Coupling

[211] Internal waves can also exchange energy with the surface wavefield, thereby implying a parametric dependence of source strength upon wind stress and possible seasonality. In the resonant interaction approximation, a pair of surface waves with nearly equal wavenumber and frequency can interact with an internal wave mode through a difference interaction [*Watson et al.*, 1976; *Olbers and Herterich*, 1978]. Estimates of energy transfer are sensitive to the structure of the upper ocean buoyancy profile. Estimates [*Watson*, 1994] using climatological buoyancy profiles and seasonally averaged wind estimates return transfer rates of several tenths of a mW m^{-2} from the internal wavefield to the surface wavefield during summer months (Figure 48) and at low latitudes during winter months (Figure 49). The high-latitude transfer rates during winter are smaller. In contrast to these wind wave results, rapid transfers of energy from a narrowband ocean swell to the internal wavefield are possible [*Watson*, 1990] and remain to be quantified.

[212] The coupling of surface and internal gravity waves thus does not appear to be the effective source at high frequencies and low vertical wavenumber as depicted in the straw man in Figure 34 and required as a boundary condition on the energy transports in the dynamic balance (section 5.1.1.4).

5.3.3. Internal Wave Coupling to Mixed Layer Turbulence

[213] The coupling of surface and internal gravity waves is not the only possible source of high-frequency internal wave energy. It has long been conjectured that mixed layer turbulence can be coupled to the internal wavefield [*Bell*, 1978]. Observations presented by *Wijesekera and Dillon* [1991] reveal a narrowband internal wave response in the upper equatorial ocean at frequencies near the upper ocean stratification rate. *Skyllingstad and Denbo* [1994] point toward shear instability as a generation mechanism. It is unclear how this mechanism translates to a rotating system.

[214] *Polton et al.* [2008] use large-eddy simulations of mixed layer turbulence with a parameterization of Stokes drift forcing by a surface gravity wavefield. This forcing sets up Langmuir circulations, and an inertial current oscillation is superimposed that advects the Langmuir cells relative to

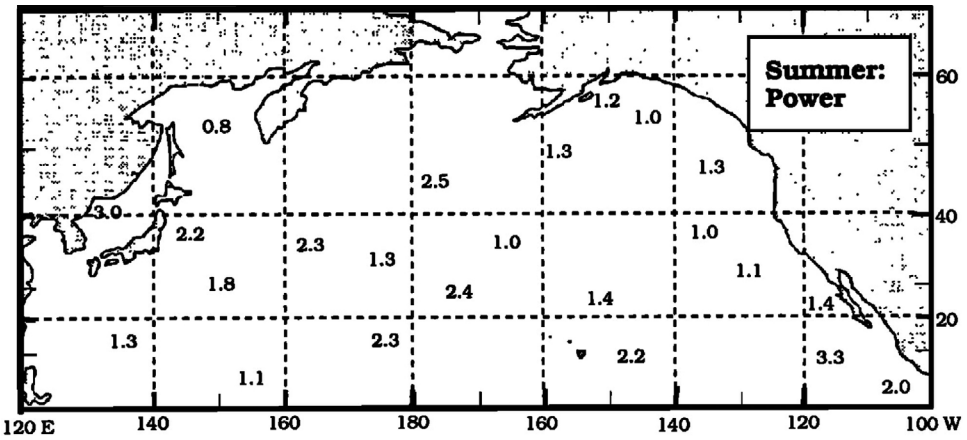

Figure 48. Power lost from the internal wavefield to the surface wavefield in units of 10^{-4} W m^{-2} for summer months [*Watson*, 1994].

the stratified interior. Vertical circulations of the Langmuir cells excite high-frequency internal waves having a phase velocity that matches the depth-averaged mixed layer velocity.

[215] *Polton et al.* [2008] estimate that energy and momentum are radiated at rates comparable to those associated with near-inertial wave radiation. These waves, however, are likely trapped within the highly stratified transition layer with implications either for mixing or for acting as a source of high-frequency energy that can be transported to lower frequency via wave-wave interactions. Analysis of upper ocean data sets for a high-frequency response on the time scale of the wind forcing could be quite enlightening.

5.3.4. Tides

5.3.4.1. Spatial Patterns

[216] Numerical models have, in several instances, been used both to estimate the energy conversion from barotropic to baroclinic tides and to keep track of the nonlinear evolution of the internal tides [e.g., *Simmons*, 2008]. While such models may not have the spatial resolution required to get the details of the nonlinear transfer process right or pick up the generation of baroclinic tides from small-scale topographic roughness, they should give some indication of where the PSI decay can be expected to be important. The eastern Atlantic is one such region (Figure 50), providing further circumstantial evidence that the NATRE spectrum is forced primarily through PSI decay.

5.3.4.2. Budgets

[217] The issue of internal tide generation, propagation, and decay has received a great deal of attention this past decade, in part because of several major field programs (the Brazil Basin Tracer Release Experiment [*Ledwell et al.*, 2000] and the Hawaiian Ocean Mixing Experiment [*Rudnick et al.*, 2003]). Near-global maps of the rate of conversion of barotropic tidal energy to baroclinic (internal) tidal energy have been provided by several [*Egbert and Ray*, 2003; *Simmons et al.*, 2004; *Simmons*, 2008; *Niwa and Hibiya*, 2001] groups. As our focus is on the background internal wavefield, none of the data sets described here is from a region of significant barotropic to baroclinic conversion.

[218] The relevant phenomenon appears to be the far-field decay of a low-mode tide via resonant interactions. This particular phenomenon is believed to be most important when the frequency of the low-mode tide is slightly higher than twice the Coriolis frequency [e.g., *Furuichi et al.*,

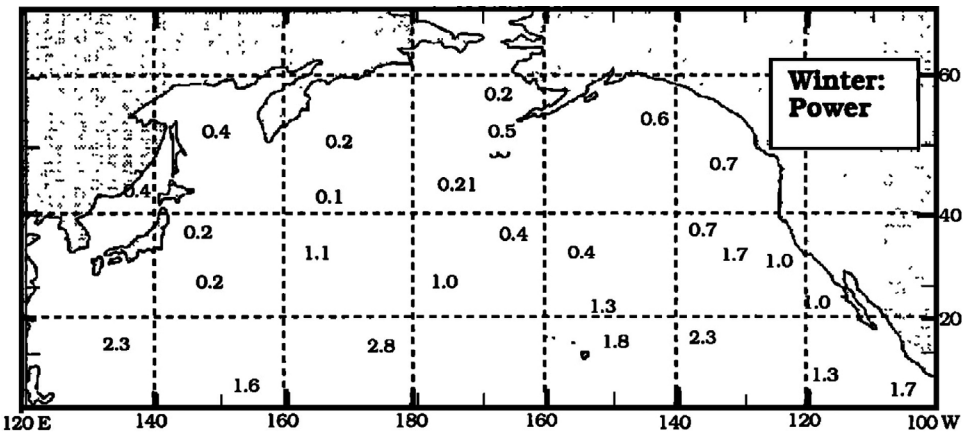

Figure 49. Power lost from the internal wavefield to the surface wavefield in units of 10^{-4} W m^{-2} for winter months [*Watson*, 1994].

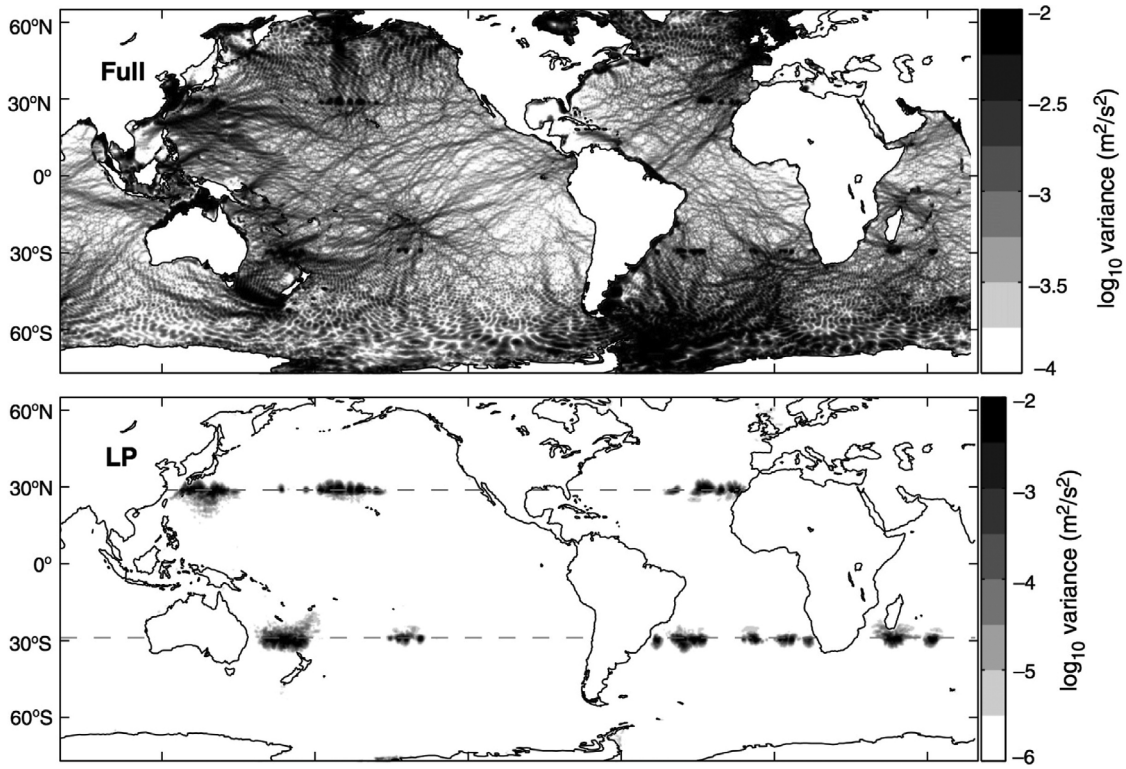

Figure 50. Maps of baroclinic tidal and near-inertial energy [from *Simmons*, 2008].

2005]. For $\sigma = M_2$, this corresponds to latitudes equatorward of 28.9°. Many of the data sets examined here are in the vicinity of this critical latitude, particularly in the western North Atlantic. There, however, estimates suggest a low-mode internal tide with horizontal energy flux of approximately 300 W m^{-1} [*Hendry*, 1977], and analyses of relevant data from the western North Atlantic have not emphasized an interpretation of semidiurnal tidal PSI decay. (Hendry's estimate of 300 W m^{-1} to the southeast represents a short-term estimate from the MODE current meter array centered about 28°N, 70°W. Long-term estimates from single moorings at 31°N, 70°W (LDE), and 34°N, 70°W (LOTUS) [*Alford and Zhao*, 2007], are approximately 150 W m^{-1} to the north-northwest and 200 W m^{-1} to the southeast. It is tempting to interpret energy flux estimates in Figure 1 of *Simmons* [2008] as suggesting that the western boundary is a source of baroclinic tidal energy at these latitudes. The lack of consistency is troubling, and the issue warrants further investigation.) An order of magnitude estimate of source strength as the observed flux distributed over the distance from the assumed source (the Blake Escarpment some 700 km distant) is smaller (300 W m^{-1}/700 km) than the nominal background dissipation rate, O(1 mW m^{-2}) (section 5.4). Moreover, the internal tide likely cannot explain the observed seasonal cycle in high-frequency internal wave energy if the source has been correctly identified. *Baines* [1982] finds that the details of the stratification profile are important in estimating the rate of conversion of barotropic tidal to baroclinic energy, but the Blake Escarpment is a relatively deep feature and extends only to 1000 m water depth, well below seasonal changes in stratification.

[219] Decay of a low-mode tide via resonant interactions poleward of the critical latitude would be through the induced diffusion mechanism. *Olbers and Pomphrey* [1981] argue that decay of a line spectrum with a typical energy density of 100 J m^{-2} would result in loss from the tides at rates between 0.005 and 0.05 mW m^{-2}. Such values will not contribute significantly to the internal wave energy balance, but note that the calculation is based upon GM76, and with $b = 0$ the estimate is biased.

[220] Barotropic tidal velocities in the eastern North Atlantic are typically larger than in the west, and consistently, available estimates of the low-mode internal tide [*Rossby*, 1988; *Siedler and Paul*, 1991; *Alford and Zhao*, 2007] are typically larger. However, such estimates exhibit significant spatial and temporal variability. Preliminary estimates of internal tide parameters from the Subduction array's center mooring assign RMS buoyancy scaled velocities u_o, v_o of (0.02, 0.02) m s^{-1} and 4 m displacement to mode 1, implying an energy flux of approximately 1 kW m^{-1}. This is a surface mooring, and contamination of energy flux estimates by vertical motion in response to ambient currents is a definite concern. *Alford and Zhao* [2007] present energy flux estimates of roughly 750 W m^{-1} for this mooring. This energy flux is directed to the northeast, seemingly at odds with both near-field and far-field sources (a minor seamount that rises to depths of 3000 m immediately to the east, the Great Meteor seamount to the north, and the European continental shelf to the northeast). Energy flux vectors in the work by *Simmons* [2008] are to the west.

[221] An order of magnitude estimate of the flux divergence (Table 1) can be obtained by dividing 1 kW m^{-1} by

the length scale characterizing the spatial variability in the internal tide amplitude, roughly 1000 km.

5.4. Dissipation

[222] Our underlying hypothesis is that the observed variability can be understood as spatially local stationary states of the radiation balance equation (23). In this context, the role of dissipation is possibly twofold. First, in a local stationary balance, forcing balances dissipation. Second, dissipation may play a role in actively shaping high-wavenumber spectra. We take up these issues in turn below.

5.4.1. Budgets

[223] Internal wave energy can be dissipated in the interior through wave breaking and at the boundaries as work done against viscous stresses.

[224] Depth integrated dissipation rates in the open ocean will typically exceed dissipation in the bottom boundary layer [*D'Asaro*, 1982; *Fu*, 1981]. The contribution of the bottom boundary layer is mitigated by buoyancy scaling of internal wave velocity and low stratification in the abyss. Away from regions of topographic generation, dissipation associated with interior wave breaking is dominated by thermocline and upper ocean regions having large stratification rates. One atypical example in which boundary layer dissipation can dominate is under ice cover in the Canadian Basin of the Arctic Ocean. There the internal wavefield is anomalously weak, and buoyancy scaling implies that internal wave velocities are largest near the upper boundary. A second atypical example is in regions of large geostrophic currents in which wave dissipation can be modeled through a linearization of the bottom stress [*Polzin*, 2010].

[225] Interior wave breaking is usually conceived of as a high-wavenumber sink associated with instability mechanisms [e.g., *Polzin*, 1996]. That sink represents a production term $\mathcal{P}$ in a turbulent mechanical energy budget

$$\sigma S_i \equiv \mathcal{P} = \mathcal{B} - \epsilon \tag{73}$$

being balanced by a buoyancy flux $\mathcal{B}$ and dissipation ϵ and a stochastic production-dissipation balance. The correlations inherent in both production and buoyancy flux terms are difficult to measure directly. Rather, specialized instrumentation and platforms are used to estimate the rate of dissipation ϵ. Full-depth estimates of such microstructure data are limited. In its stead, use has been made of fine structure parameterizations based upon (67). These assign a value of

$$\mathcal{P} = 8 \times 10^{-10}\ \mathrm{Wkg}^{-1}$$

and

$$K_\rho = \mathcal{B}/N^2 = 5 \times 10^{-6}\ \mathrm{m^2 s^{-1}}$$

to GM76 at 30° latitude and a buoyancy frequency of 3 cph.

[226] With either the fine structure or microstructure method, a major caveat is that one needs to understand how (not just whether) the sampling of the wavefield is biased. For example, while one might hope to make sense of observations in NATRE as being almost exclusively forced by a PSI decay (Polzin, manuscript in preparation, 2011), analysis of the diapycnal dispersion of an anthropogenic tracer suggests a long-term average of a factor of 2 larger. The difference may actually be related to the spatial variability of the tide. Experience (K. L. Polzin, Internal wave generation and scattering from rough topography, manuscript in preparation, 2011b) suggests that issues of biasing in regions of rough topography are much more problematic than the factor of 2 in NATRE.

5.4.2. Spectral Patterns: Models

[227] In order to reconcile the $O(1)$ high-wavenumber normalized Boltzman rates with the claim that GM76 represents a stationary state, *McComas and Müller* [1981b] invoke a spectral representation which assumes that dissipation events have space and time scales much smaller than the scales of the internal waves and that the turbulence can be parameterized by an eddy viscosity ν, resulting in

$$\sigma S_i(\mathbf{p}) = \frac{\partial E(\mathbf{p})}{\partial t} = -\nu m^2 E(\mathbf{p}). \tag{74}$$

Similar representations are examined in greater detail by *Natarov and Müller* [2005].

[228] Some generalization of this model may be required if it is necessary to invoke dissipation in order to obtain a stationary state. Dissipation events will typically have vertical scales smaller than the nominal 10 m cutoff, gauged either by correlation length scales of turbulent dissipation [*Gregg et al.*, 1993b] or the exclusive contribution of sub–10 m wavelength shear to the occurrence of supercritical Richardson number events [*Polzin*, 1996] (with supercritical Richardson number being indicative of shear instability), so the spatial scale separation between waves and turbulence could be justified. But the application of phenomenological mixing models indicates that dissipation events have lifetimes in excess of a buoyancy period [*Polzin*, 1996] so that a temporal scale separation is problematic. In general, *Polzin* [1996] finds such phenomenological mixing models to be useful diagnostic tools but difficult to develop into prognostic models because of this finite lifetime.

[229] A key point in a generalized model is that the fine structure parameterization (67) weights the contribution of each frequency to dissipation as a product of vertical gradient variance and aspect ratio, and thus, high-frequency waves dominate the total dissipation. The dissipation function (74) weights each frequency only as the vertical gradient variance and so emphasizes the near-inertial waves that dominate the vertical shear. Phenomenological mixing models [*Polzin*, 1996] have been shown to be in agreement with (67). Observations presented by *Alford* [2000] also appear to support the role of high-frequency variability.

[230] A qualitative distinction between (74) and (67) may be drawn by noting that (74) is likely to be appropriate for a system of coupled oscillators. It may not make sense for a description of the internal wavefield as a system of wave packets in which dissipation events are associated with the transport of individual wave packets to breaking scales, as

invoked in the ray tracing models [e.g., *Henyey et al.*, 1986]. The ray tracing model does not need a dissipation function because the wave packets are followed as particles to their annihilation.

[231] We regard the impact of dissipation on the internal wave spectral domain as an open question awaiting rigorous analysis.

5.4.3. Spectral Patterns: The Midfrequency Dip and Bottom Boundary Conditions

[232] Many of the frequency spectra are poorly characterized by a simple power law fit near semidiurnal frequencies (e.g., Figure 13). Apart from the tidal peak, observed spectral levels tend to be smaller than the power law characterization. *Levine* [2002] puts forward the hypothesis that this midfrequency dip is related to nonlinearity in how energy is transferred to higher and lower frequency out of the semidiurnal peak. Here we put forward an additional hypothesis regarding such departures. With a buoyancy profile that decreases toward the bottom boundary, only the low-frequency portion of the wavefield reaches the bottom, where wave energy can be dissipated as work done against viscous stresses and vertical scale transformations associated with reflection or scattering from a nonuniform bathymetry can act. Calculations have already been made to assess the rate at which energy is redistributed by such scale transformations for the GM spectrum [e.g., *Müller and Xu*, 1992; *Eriksen*, 1985b]. With an eye toward explaining spatial variability of the background spectrum, one can also ask the question of how the equilibrated spectrum could be shaped by the cumulative effects of scale transformations acting through the bottom boundary condition and nonlinearity acting through radiation balance equation's source function. This is a topic for future research, which requires a relatively sophisticated treatment of (23).

5.5. Propagation

[233] The ability of low-mode internal waves to propagate long distances from their generation sites is loosely constrained in the observational record and is a serious issue for internal wave energy balance studies. The most significant processes are tidal constituents and near-inertial waves. These internal waves do not play a major role in this regional study of the high-wavenumber and high-frequency spectral variability. They do, however, act as sources for the internal wave continuum, whether it be through extreme-scale separated interactions (section 5.1.1.3) or via a PSI decay process of tidal energy into near-inertial waves that then is linked to the continuum (section 5.1.2.1).

[234] We anticipate that variability in the tidal and inertial peaks is linked to variability in the continuum. *Fu* [1981] documents variability of the inertial peak in the western North Atlantic and obtains the following regional classification scheme: Class 1 spectra have prominent inertial peaks. Such spectra occur in records obtained from the Mid-Atlantic Ridge in the vicinity of 28°N and occur in conjunction with relatively white frequency spectra. We anticipate that the inertial peaks here are related to a PSI decay process (section 5.1.2.1). Class 2 spectra have less prominent peaks and are found (1) in the upper ocean at depths less than 2000 m, (2) in the deep ocean above rough topography off the Mid-Atlantic Ridge axis and away from 28°N, and (3) in the deep ocean under the Gulf Stream. We anticipate issues of internal lee wave generation and wave mean interactions (section 5.2) to be significant. Finally, class 3 spectra have the smallest inertial peaks and are found above smooth topography. *Fu* [1981] argues that class 1 and class 2 inertial peaks are associated with local processes and class 3 inertial peaks are consistent with propagation effects as waves initialized with the GM76 spectrum reflect from their turning latitudes. Such quantitative estimates depend upon the vertical modal distribution of energy, and the regional variability of m_* is not well constrained in that study. *Fu*'s [1981] study included the MODE central mooring instrumented at 500 (class 2a), 1500 (class 2a), and 4000 (class 3) m depths, whose location was the site of moorings during IWEX and FASINEX (section 3.3.2), and PolyMode IIIc mooring 82 (172 (class 2a), 322 (class 2a), 522 (class 2a), 2446 (class 2b), and 3946 (class 2b) m) (section 3.3.3). The vertical profile data sets at these locations in our study are focused upon depths less than 2000 m. *Leaman* [1976], however, comments upon differences between vertical profiles obtained over rough and smooth topography in the vicinity of MODE central.

[235] The last decade has seen the development of general circulation models that include both tidal forcing and wind products with sufficient temporal resolution to force inertial motions [*Simmons*, 2008; *Arbic et al.*, 2010]. The models, however, obey their own dynamics: near-inertial forcing will be influenced by the mixed layer scheme, absence of an eddy field, presence or absence of a realistic internal wavefield, topographic representation, subgrid closures, etc. Unraveling how such model fields relate to the ocean will be a complicated but useful aid in interpreting the oceanic internal wavefield.

[236] The issue of propagation demands careful assessment. As long as the roles of the bottom boundary condition and refraction in the mesoscale eddy field are not appreciated, the dominant balance of terms in an energy budget can be seriously misconstrued. See, for example, the difference of opinion about the Brazil Basin data set by *St. Laurent and Garrett* [2002] and *Polzin* [2004b] that appears to be resolved in favor of a high efficiency of topographic scattering in the work by Polzin (manuscript in preparation, 2011b).

[237] Similarly, *Alford and Zhao* [2007] estimate significant horizontal energy fluxes in the near-inertial band north of the Gulf Stream and regard those flux estimates as symptomatic of the ability of low-mode waves to propagate large distances. The issue of mooring motion contaminating the horizontal energy flux estimates bears further investigation before those flux estimates can be considered to be robust.

6. CONCLUSION

[238] The ingredients that shape the deep ocean energy spectrum have been known for some time. Figure 34, which

is taken from *McComas* [1977], presents one version of how these ingredients can be combined. In that recipe, the primary sources are at high frequency, and a transfer of energy to higher vertical wavenumber is associated with the ID mechanism. Parametric spectral fits summarized in Figure 37 strongly suggest that the ID mechanism plays an active role in determining the observed power laws. However, the details are not consistent with such an interpretation.

[239] We now believe that near-inertial and tidal sources dominate high-frequency sources of internal wave energy, and this poses a real challenge to the induced diffusion mechanism: Energy transports associated with induced diffusion are to higher vertical wavenumber and lower frequency for vertical wavenumber domain power laws $b \geq 0$. That requires a source of high-frequency energy. Possible sources are coupling of internal waves with surface swell, internal wave coupling to mixed layer turbulence, and a weaker version of internal wave coupling to the eddy field. These possible sources are not well constrained, either observationally or theoretically.

[240] A second facet is that transports under the resonant interaction approximation are not completely understood. Hitherto neglected local interactions may play a significant role in determining nonlinear transports.

[241] A third facet is that resonant kinetic equation evaluations in Figure 40 indicate that GM76 is far from being a stationary state, seemingly at odds with GM76 representing an ID no flux state. Self-consistent solutions to a broadened kinetic equation could be much closer to being stationary and exhibit energy transfers appropriate for low-frequency sources. A closely related result is that ray tracing diagnostics imply a transport of action to higher frequency. This transport could provide a pathway to supply energy to the high-wavenumber continuum. A first principles derivation of the spectral transports associated with the ray tracing models would be enlightening.

[242] Despite such uncertainty, nonlinearity is clearly an organizing principle. Power laws associated with parametric spectral representations lie close to the induced diffusion stationary states of the resonant kinetic equation describing the lowest-order nonlinear transfers. The one exception appears to be a wavefield set up by the decay of a semidiurnal internal tide through the parametric subharmonic instability.

[243] While our ideas of the ingredients and their geographic distribution have evolved, our knowledge of how to create the observed spectrum (the recipe) has remained relatively static. We are confident that such recipes are within reach, but it will take a combination of observations, analytic work in the context of a radiation balance equation, and realistic direct numerical simulations. Theoretical studies coupled to observational programs, especially those that would document 2-D spectra, transfer rates, and the spectral character of the forcing functions and seek to define the role of the geostrophic flow field are a high priority. Resonant calculations show strong nonstationary tendencies, and this issue needs to be either resolved or circumvented before addressing the contributions of other ingredients to the recipes.

[244] Variability in the spectral characteristics of the deep ocean internal wavefield documented in section 3 and consideration of regional variability in the forcing fields in section 5 leads us to propose the following straw men for further investigation:

[245] 1. The NATRE region is a minimum for eddy energy in the North Atlantic, and wind work at near-inertial frequencies is small. Equatorward of the critical latitude for M_2 tides, PSI decay of the low-mode internal tide represents the major forcing of the internal wavefield. The NATRE spectrum is an outlier with extremely high bandwidth, steep vertical wavenumber, and shallow frequency spectral slopes. A preliminary recipe for the NATRE region is described in section 5.1.2.1. This recipe invokes a heuristic cascade closure for nonlinearity that has its roots in the ray tracing diagnostics.

[246] 2. The contrasts between the wavefields north and south of the Gulf Stream are distinct and appear to have a parallel with differences between subtropical and subpolar gyres in the North Pacific along its eastern boundary. The latter case deserves further investigation to confirm spectral parameters graphically extracted from the literature. Our leading hypothesis is that the differences can be directly related to the relative roles of near-inertial wind forcing and interactions with the mesocale eddy field via (71) and (72). We have not yet translated this hypothesis into a recipe.

[247] 3. The tentative signature of a phase lag between seasonal cycles in high-frequency and near-inertial frequency waves in the eddy desert of the North Pacific may be a signature of nonlinear transfers in the absence of wave mean coupling.

[248] The future will certainly bring many further exciting developments and the synthesis of theoretical, observational, and numerical results yet to be obtained.

APPENDIX A: METADATA

[249] Metadata for the data sets used in this study can be found in Tables A1 and A2.

APPENDIX B: INSTRUMENTATION

[250] A terse presentation of many of these data was made by *Lvov et al.* [2004], simply summarizing the available power law estimates as points in a frequency-wavenumber domain. That presentation was limited to spectra appearing in published literature. The intent of this work was to present pertinent data in a common framework, limiting the potential pitfalls associated with an irregular analysis. This does not limit uncertainties associated with the use of different instrument systems. Details of an instrumental and technical nature that impact the interpretation of the data are collected herein.

B1. Moored Current Meters

[251] Regarding the interpretation of moored current meter data as internal waves, there are two primary sets of issues. The first set is referred to as fine structure contamination.

TABLE A1. Metadata for Moored Current Meters Used in This Study

Place	Latitude	Longitude	Water Depth (m)	Sensor Depth (m)	Instrument Type	Code	Start	Stop	N (cph)	θ_z (C m^{-1})
Site D	39°17.9′	70°05.6′	2640	106	VACM	WHOI 2203	26 Feb 1967	25 Mar 1967	3.03	
				511		WHOI 2204			1.48	
				1013		WHOI 2205			0.66	
				1950		WHOI 2206			0.58	
Shelf-slope	39°36.6′	70°56.5′	2305	305	VACM	WHOI 5881	10 Feb 1976	8 Aug 1976	2.82	−0.0235
Primer	39°05.2′	69°21.4′	2990	391	VACM	WHOI 9872	8 Dec 1995	4 Dec 1997	2.39	−0.0170
IWEX	27°43.9′	69°50.95′	5453	604	VACM	WHOI 515A4	3 Nov 1973	15 Dec 1973	2.55	−0.0175
				604	VACM	WHOI 515B4	3 Nov 1973	15 Dec 1973	2.55	−0.0177
				633	VACM	WHOI 515C5	3 Nov 1973	15 Dec 1973	2.60	−0.0157
LOTUS	34°1.2′	70°1.45′	5366	328	VACM	WHOI 7666	11 May 1982	12 Apr 1983	1.49	−0.00356
	33°58.55′	70°0.36′	5366	348	VACM	WHOI 7886	14 Apr 1983	1 May 1984	1.49	−0.00356
PolyMode III-c	15°23.40′	53°55.20′		319	VACM	NOVA 80	11 May 1977	1 May 1978	2.78	−0.03096
	15°11.50′	53°12.30′		309	VACM	NOVA 81	12 May 1977	20 Dec 1977		
	15°02.10′	54°12.90′		338	VACM	NOVA 82	13 May 1977	1 May 1978		
FASINEX	27°58.9′	69°58.8′		556	VACM	WHOI 8293	29 Oct 1984	18 Jun 1986	2.48	−0.0178
				631	VACM	WHOI 8294			2.61	−0.0202
Subduction	25°31.90′	28°57.2′		300	VMCM	WHOI	12 Feb 1992	14 Oct 1992	2.44	−0.02244
Subduction	25°31.90′	28°57.2′		300	VMCM	WHOI	15 Oct 1992	16 Jun 1993	2.44	−0.02244
Eastern Boundary Currents	37°6.7′	127°32.1′	4752	598	Aanderaa	rcm02674	9 Aug 1992	19 Aug 1994	2.01	0.00455
Ocean Storms	47°25.4′	139°17.8′	4224	199	VMCM	rcm07420	20 Aug 1987	25 Jun 1988	2.25	0.006
AIWEX	74°	143°–144°	3700	250	SBE-3	–	20 Mar 1985	5 Apr 1985	–	0.02

Here the presumption is that the data record represents signal and that departures from linear internal wave kinematics are associated with either (1) quasi-permanent fine structure (either density or velocity) being advected past the sensor [e.g., *Polzin et al.*, 2003] (section 2.1.4); (2) self-advection within the wavefield [e.g., *Sherman and Pinkel*, 1991] (section 5.1.4); or (3) attempting to estimate density perturbations using temperature data only and invoking a stable relation between density, temperature, and salinity. This latter assumption fails in regions that have significant large-scale gradients of temperature and salinity on isopycnals [e.g., *Ferrari and Polzin*, 2005]. See *Polzin et al.* [2003], *Sherman and Pinkel* [1991], and *Ferrari and Polzin* [2005] for further discussion of these issues. The second set of issues is instrumental in nature: (1) drag associated with flow past a mooring will induce movement [e.g., *Foffonoff*, 1966], (2) typical sampling rates are not sufficient to resolve internal wave spectrum out to the buoyancy frequency in the upper ocean, and (3) there are issues with instrument response.

[252] Regarding the first issue, there are typically three classes of moorings: deep, intermediate, and surface. A deep mooring will utilize glass balls as buoyancy elements distributed along the mooring cable. The primary buoyancy element for an intermediate mooring will be a large syntactic sphere at the upper terminus. This mooring type was utilized at Woods Hole Oceanographic Institution starting in the early 1980s. It has less overall drag and consequently provides a more stable platform. Finally, surface moorings are loosely tethered in order to accommodate the often sizable surface motions associated with surface waves. As a result, the surface buoy inscribes a watch circle roughly equal to the water depth [*Trask et al.*, 1982]. Vertical motion of the instruments can be diagnosed if pressure sensors are included (e.g., Figure B1). Experience suggests that inertial and tidal frequencies suffer greater contamination by mooring motion than supertidal frequencies. Significant discussions are given by *Fu* [1981] and *Ruddick and Joyce* [1979].

[253] Regarding the second issue, insufficient sampling rates will result in the aliasing of high-frequency signals back into the resolved frequency domain. Ordinarily, the frequency spectra will be sufficiently red that the aliased energy is relatively small. However, if there is a substantial bump at the buoyancy frequency associated with turning point dynamics [e.g., *Desaubies*, 1975], the aliased energy may be significant. Ascertaining whether this is the case requires information on the vertical wavenumber content of the wavefield and details of the vertical structure of the buoyancy profile. Without such information and in the absence of pressure records, it is difficult to assert that the departure of the observed high-frequency spectra in Figure 2, for example, is noise rather than signal.

[254] Regarding the third issue, the principle moored current meters used here are the VACM and VMCM. The VACM employs a Savonius rotor, and the VMCM uses sets of propellers. The VMCM [*Weller and Davis*, 1980] was designed to have a cosine response to eliminate "pumping" associated with the motion of a surface mooring. VACMs

TABLE A2. Metadata for the Vertical Profiling Instrumentation Used in This Study[a]

Place	Latitude	Longitude	Water Depth (m)	Instrument Type	Start	Stop
Station W (3)	39°	70°	3000	MMP	20 Jun 2003	5 Aug 2003
Station W (3)	39°	70°	3000	MMP	17 Jan 2004	2 Mar 2004
Mode	28°	69° 40′	5440	EMVP	11 Jun 1973	15 Jun 1973
FASINEX	27°–29°	67°30′–70°30′	≅5200	HRP	17 Feb 1986	5 Mar 1986
NATRE	23°56′–27°32′	26°45′–30°43′	≅5500	HRP	28 Mar 1992	14 Apr 1992
SFTRE2a	14°–16°	50°–57°	≅5400	HRP	14 Nov 2001	24 Nov 2001
PATCHEX[1]	34°	127°	≅700	MSP	17 Oct 1986	24 Oct 1986
PATCHEX[2]	34°	127°	≅4700	*FLIP*	Oct 1986	7.5 days
SWAPP	35°8.2′	126°59.0′	≅4700	*FLIP*	Feb–Mar 1990	18 days
STREX	50°	140°	≅4000	XCP	8 Nov 1980	22 Nov 1980
AIWEX	74°0′–74°12′	144°0′–145°0′	≅3750	XCP	3 Apr 1985	14 Apr 1985

[a]SFTRE2, Salt Finger Tracer Release Experiment, Part 2; STREX, Storm Transfer and Response Experiment; EMVP, electromagnetic velocity profiler; MMP, McClane moored profiler; MSP, multiscale profiler.

are standard for subsurface moorings. VACMs have a finite stall speed of about 2 cm s^{-1} [*Luyten and Stommel*, 1991]. Good directional data are believed to be obtained at speeds smaller than this. The resulting "noise" is not well defined. VMCM data are calibrated assuming no significant stalling. See *Hogg and Frye* [2007] for a more recent discussion of current meter performance.

B2. Doppler Sonars

[255] Doppler sonars do not measure horizontal velocity at a point but determine Doppler shifts as a function of range along multiple acoustic beams. These Doppler shifts are interpreted as slant velocities of suspended acoustic backscattering targets moving with the water relative to the instrument platform. Individual estimates of ocean velocity are highly uncertain: hundreds of pings are typically used to average incoherent noise from the system. Estimates of signal-to-noise ratios are given by *Anderson* [1992] and *Alford* [2000, appendix]. The insidious complication of package motion and beam separation effects are considered by *Polzin et al.* [2002].

B3. Vertical Profiling Instrumentation

[256] Most of the vertical wavenumber domain information considered here was obtained with vertical profiling instrumentation. Estimates of the vertical structure of the velocity field can be obtained by using a number of different sensors, each of which has its own strengths and weaknesses.

[257] Sanford's electromagnetic velocity profiler [*Sanford*, 1975] senses the voltage drop associated with an electrical

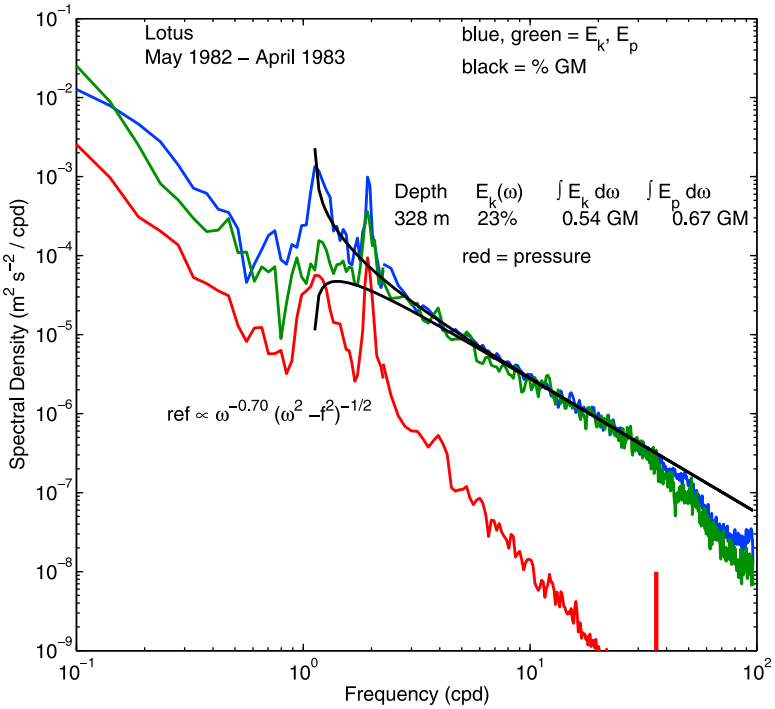

Figure B1. LOTUS frequency spectra of horizontal kinetic energy (blue line), potential energy (green line), and pressure p interpreted as a vertical displacement, $N^2p^2/2$. This interpretation implies that possible contamination by mooring motion is more problematic at inertial and tidal frequencies than within the internal wave continuum.

current (seawater) in a magnetic field (the Earth's, in this case). The measurement is uncertain to within a conductivity weighted mean, so that other sensors need to be incorporated to provide estimates of the absolute velocity field. Noise levels are typically around 0.5 cm s^{-1}, which is sufficient to start resolving vertical wavelengths smaller than 10 m. XCPs operate on the same principle but may have somewhat larger noise levels (1.0 cm s^{-1}).

[258] Data from several acoustically tracked dropsondes have been analyzed but not presented. With this instrument system, the horizontal position is estimated from range information provided by an acoustical net and depth information from an onboard CTD sensor suite. Oceanic velocity estimates assume that the package tracks the flow field as it descends. This method provides estimates of the absolute velocity, but the small-scale noise is relatively high. Acoustic tracking provides positions to within 1 m. A typical descent rate of 1 m s^{-1} implies that the background internal wavefield having vertical wavelengths smaller than several hundred meters will be obscured by noise.

[259] A third method is to utilize an acoustic travel time sensor to estimate relative flow past a freely falling vehicle (e.g., the High resolution Profiler [*Schmit et al.*, 1988] and the Multi-Scale Profiler [*Winkel et al.*, 1996]). Estimates of the oceanic velocity profile are deduced from these relative velocity data and a model of how the vehicle responds to the relative flow. The method is capable of resolving oceanic shear at 1 m scales. The limitations are at larger wavelengths. The offsets (zeros) of the acoustic travel time sensor are typically determined in situ and may even be temperature and pressure dependent. Thus, the resulting profiles are uncertain to a linear trend. Other information, such as that provided by an electric field sensor or matching with a shipboard acoustic Doppler current profiler record, is required to provide the largest-scale information.

[260] Acoustic travel time sensors are used in the McClane moored profiler [*Doherty et al.*, 1999]. This instrument autonomously samples relative velocity, temperature, conductivity, and pressure while transiting a mooring cable. Estimates of relative velocity are thus absolute. Noise levels in the velocity record are nominally estimated at 0.5 cm s^{-1}. Biases related to drifting zeros and mooring oscillations are not presently well defined.

[261] Velocity data obtained with Doppler sonars typically estimate horizontal velocity from back-to-back acoustic beams. In so doing, one assumes that the velocity field is horizontally uniform. This assumption breaks down as the beam separation increases and will preferentially contaminate high-frequency, small vertical scale signals [*Polzin et al.*, 2002].

APPENDIX C: PROCESSING

[262] In the absence of a mean flow, the linear internal wave equation is [e.g., *Gill*, 1982]

$$\left(\partial_t^2 + f^2\right)\partial_z^2 w + \left[N^2(z) + \partial_t^2\right]\left(\partial_x^2 + \partial_y^2\right)w = 0 \qquad \text{(C1)}$$

for arbitrary stratification profile $N^2(z)$ and vertical velocity w. If the stratification profile varies much more slowly than the wave phase, a WKB approximation for vertically propagating waves provides the approximate solution

$$w \propto N(z)^{-1/2} e^{i\int N(z)dz}, \qquad \text{(C2)}$$

and so the effects of a variable buoyancy profile can be accounted for by stretching the depth coordinate by N and scaling the horizontal velocities by $N^{1/2}/N_o^{1/2}$, in which N_o is a reference stratification. The value N_o = 3 cph is often used. The use of the WKB approximation requires $\sigma^2 \ll N^2$. If this relation is not satisfied, solutions can be found by treating (C1) as an eigenvalue problem with appropriate boundary conditions. If $\sigma^2 \ll N^2$ but the wave phase is not slowly varying, the boundary conditions are that $w = 0$ at the top ($z = 0$) and bottom ($z = H$), which then implies that the horizontal velocities $[u(z), v(z)]$ are proportional to

$$N(z)^{1/2}\cos\left(n\pi \int_0^z N(z')dz' \Big/ \int_0^H N(z')dz'\right) \qquad \text{(C3)}$$

for integer values of n. For data sets that document the velocity profile over the entire water column, the first three modes have been estimated by using a linear regression. Vertical wavenumber spectra are calculated by using a cubic spline to interpolate onto a uniform grid having approximately the same resolution as the unstretched data.

[263] Current meter data used here have sampling intervals of 3.75 min to 1 h. Frequency spectra have been calculated using transform intervals of 10 2/3 and 8/3 days. Spectra are displayed using the latter at supertidal frequencies ($\sigma >$ 2.4 cpd^{-1}) and the former at lower frequencies. The intent is to give finer resolution to inertial and tidal peaks and decreased variability at higher frequency.

APPENDIX D: A SARGASSO SEA SPECTRUM

[264] We have characterized the background internal wave spectrum in the Sargasso Sea as

$$E(m,\sigma) = \frac{2A}{\pi m_*}\left[1 + \frac{49f^2}{\left[1764(\sigma - f)^2 + f^2\right]}\right]\frac{1}{\sigma^{1.75}} \cdot \frac{1}{\left[1 + \left(m/m_*\right)^2\right]^{1.125}}, \qquad \text{(D1)}$$

with $m_* = 10\pi/1300\ \mathrm{m}^{-1}$ and normalization constant A chosen to return $E = 0.56 \times 30 \times 10^{-4}\ \mathrm{m^2\ s^{-2}}$. This places the gradient variance at approximately $(3/4)\int_0^{2\pi/10\mathrm{m}} 2m^2E(m)\,dm = (2\pi/10)N^2$. Power laws characteristic of the Sargasso Sea data sets (section 3.3.2) are selected specifically to lie on the induced diffusion constant flux solution (section 5.1.1.3). The inertial peak was selected with the constraint that E_k/E_p = 4.4 on the basis of moored data. We have deferred from invoking nonseparable conditions via $m_* = m_*(\sigma)$ that are a documented part of the observational record [*Müller et al.*,

1978] and appear as $E_k(m = 0.01\ \text{cpm})/E_p(m = 0.01\ \text{cpm})$ in excess of this value [*Polzin et al.*, 2003].

[265] **ACKNOWLEDGMENTS.** The authors gratefully acknowledge the efforts of many talented researchers who were instrumental in collecting, processing, and archiving the data presented here. Special thanks are extended to John Toole for providing as yet unpublished MP data from Site D, Tom Sanford for providing access to a number of his EMVP and AVP data sets, and Carl Wunsch for the PolyMode IIIc current meter data set. We thank Naoto Yokoyama for his patience in revising the numerical code for solving the broadened kinetic equation. We gratefully acknowledge funding provided by a Collaborations in Mathematical Geosciences (CMG) grant from the National Science Foundation. Y.L. additionally acknowledges NSF DMS grant 0807871 and ONR award N00014-09-1-0515. The authors appreciate the efforts of two anonymous reviewers who helped focus the manuscript.

[266] The Editor of this manuscript was Mark Moldwin. He thanks two anonymous reviewers.

REFERENCES

Alford, M. (2000), Observations of overturning in the thermocline: The context of ocean mixing, *J. Phys. Oceanogr.*, *30*, 805–832.

Alford, M. H. (2003), Improved global maps and 54-year history of wind-work on ocean inertial motions, *Geophys. Res. Lett.*, *30*(8), 1424, doi:10.1029/2002GL016614.

Alford, M. H., and M. Whitmont (2007), Seasonal and spatial variability of near-inertial kinetic energy from historical moored velocity records, *J. Phys. Oceanogr.*, *37*, 2022–2037.

Alford, M. H., and Z. Zhao (2007), Global patterns of low-mode internal-wave propagation. Part I: Energy and energy flux, *J. Phys. Oceanogr.*, *37*, 1829–1848.

Anderson, S. P. (1992), Shear, strain and thermohaline fine structure in the upper ocean, Ph.D. thesis, 173 pp., Univ. of Calif., San Diego, La Jolla.

Arbic, B. K., and G. R. Flierl (2004), Effects of mean flow direction on energy, isotropy, and coherence of baroclinically unstable beta-plane geostrophic turbulence, *J. Phys. Oceanogr.*, *34*, 77–93.

Arbic, B. K., A. J. Wallcraft, and E. J. Metzger (2010), Concurrent simulation of the eddying general circulation and tides in a ocean model, *Ocean Modell.*, *32*, 175–187.

Baines, P. G. (1982), On internal tide generation models, *Deep Sea Res.*, *29*, 307–338.

Bell, T. H. (1978), Radiation damping of inertial oscillations in the upper ocean, *J. Fluid Mech.*, *88*, 289–308.

Bender, C. M., and S. A. Orzag (1978), *Advanced Mathematical Methods for Scientists and Engineers*, 593 pp., McGraw-Hill, New York.

Blumsack, S. L. (1993), A model for the growth of mudwaves in the presence of time varying currents, *Deep Sea Res. II*, *40*, 963–974.

Briscoe, M. G. (1975a), Internal waves in the ocean, *Rev. Geophys.*, *13*, 591–598.

Briscoe, M. G. (1975b), Preliminary results from the trimoored internal wave experiment (IWEX), *J. Geophys. Res.*, *80*, 3872–3884.

Briscoe, M. G., and R. A. Weller (1984), Preliminary results from the long-term upper-ocean study (LOTUS), *Dyn. Atmos. Oceans*, *8*, 243–265.

Brown, E. D., and W. B. Owens (1981), Observations of the horizontal interactions between the internal wave field and the mesoscale flow, *J. Phys. Oceanogr.*, *11*, 1474–1480.

Brown, N. L. (1974), A precision CTD microprofiler, in *IEEE International Conference on Engineering in the Ocean Environment, Ocean '74*, vol. 2, pp. 270–278, Inst. of Electr. and Electron. Eng., New York.

Bühler, O., and M. E. McIntyre (2005), Wave capture and wave-vortex duality, *J. Fluid Mech.*, *534*, 67–95.

Caillol, P., and V. Zeitlin (2000), Kinetic equations and stationary energy spectra of weakly nonlinear internal gravity waves, *Dyn. Atmos. Oceans*, *32*, 81–112.

Cairns, J. L. (1975), Internal wave measurements from a midwater float, *J. Geophys. Res.*, *80*, 299–306.

Cairns, J. L., and G. O. Williams (1976), Internal wave observations from a midwater float: 2, *J. Geophys. Res.*, *81*, 1943–1950.

Carnevale, G. F., and J. S. Frederiksen (1983), A statistical dynamical theory of strongly nonlinear internal gravity waves, *Geophys. Atrophys. Fluid Dyn.*, *33*, 175–207.

Chereskin, T. K., M. Y. Mooris, P. P. Niiler, P. M. Kosro, R. L. Smith, S. R. Ramp, C. A. Collins, and D. L. Musgrave (2000), Spatial and temporal characteristics of the mesoscale circulation of the California Current from eddy-resolving moored and shipboard measurements, *J. Geophys. Res.*, *105*, 1245–1269.

Codiga, D. L., and C. C. Eriksen (1997), Observations of low frequency circulation and amplified subinertial currents at Cobb seamount, *J. Geophys. Res.*, *102*, 22,993–23,007.

Crawford, G. B., and W. G. Large (1996), A numerical investigation of resonant inertial response of the ocean to wind forcing, *J. Phys. Oceanogr.*, *26*, 873–891.

D'Asaro, E. A. (1982), Absorption of internal waves by the benthic boundary layer, *J. Phys. Oceanogr.*, *12*, 323–336.

D'Asaro, E. A. (1984), Wind forced internal waves in the North Pacific and Sargasso Sea, *J. Phys. Oceanogr.*, *14*, 781–794.

D'Asaro, E. A. (1985), The energy flux from the wind to near-inertial motions in the surface mixed layer, *J. Phys. Oceanogr.*, *15*, 1043–1059.

D'Asaro, E. A. (1995a), A collection of papers on the Ocean Storms Experiment, *J. Phys. Oceanogr.*, *25*, 2817–2818.

D'Asaro, E. A. (1995b), Upper-ocean inertial currents forced by a strong storm. Part II: Modeling, *J. Phys. Oceanogr.*, *25*, 2937–2952.

D'Asaro, E. A., and M. D. Morehead (1991), Internal waves and velocity finestructure in the Arctic Ocean, *J. Geophys. Res.*, *96*, 12,725–12,738.

D'Asaro, E. A., C. C. Eriksen, M. D. Levine, P. Niiler, C. A. Paulson, and P. Van Meurs (1995), Upper ocean inertial currents forced by a strong storm. Part I: Data and comparisons with linear theory, *J. Phys. Oceanogr.*, *25*, 2909–2936.

Desaubies, Y. J. F. (1975), A linear theory of internal wave spectra and coherences near the Väisälä frequency, *J. Geophys. Res.*, *80*, 895–899.

Desaubies, Y. J. F. (1976), Analytic representation of internal wave spectra, *J. Phys. Oceanogr.*, *6*, 976–981.

DeWitt, R. J., and J. Wright (1982), Self-consistent effective-medium theory of random internal waves, *J. Fluid Mech.*, *115*, 283–302.

DeWitt, R. J., and J. Wright (1984), Self-consistent effective-medium parameters for oceanic internal waves, *J. Fluid Mech.*, *146*, 253–270.

Doherty, K. W., D. E. Frye, S. P. Liberatore, and J. M. Toole (1999), A moored profiling instrument, *J. Atmos. Oceanic Technol.*, *16*, 1816–1829.

Egbert, G. D., and R. D. Ray (2003), Semi-diurnal and diurnal tidal dissipation from TOPEX/Poseidon altimetry, *Geophys. Res. Lett.*, *30*(17), 1907, doi:10.1029/2003GL017676.

Eriksen, C. C. (1985a), Some characteristics of internal gravity waves in the equatorial Pacific, *J. Geophys. Res.*, *90*, 7243–7255.

Eriksen, C. C. (1985b), Implications of ocean bottom reflection for internal wave spectra and mixing, *J. Phys. Oceanogr.*, *15*, 1145–1156.

Eriksen, C. C., R. A. Weller, D. L. Rudnick, R. T. Pollard, and L. A. Regier (1991), Ocean frontal variability in the frontal air-sea interaction experiment, *J. Geophys. Res.*, *96*, 8569–8591.

Ferrari, R., and K. Polzin (2005), Finescale variability of the T-S relation in the eastern North Atlantic, *J. Phys. Oceanogr.*, *35*, 1437–1454.

Flatté, S. M., F. S. Henyey, and J. A. Wright (1985), Eikonal calculations of short-wavelength internal-wave spectra, *J. Geophys. Res*, *90*, 7265–7272.

Foffonoff, N. P. (1966), Oscillation modes of a deep sea mooring, *Geo. Mar. Technol.*, *2*, 13–17.

Foffonoff, N. P. (1969), Spectral characteristics of internal waves in the ocean, *Deep Sea Res.*, *16*, suppl., 58–71.

Fritts, D. C., and M. J. Alexander (2003), Gravity wave dynamics and effects in the middle atmosphere, *Rev. Geophys.*, *41*(1), 1003, doi:10.1029/2001RG000106.

Fu, L. L. (1981), Observations and models of inertial waves in the deep ocean, *Rev. Geophys.*, *19*, 141–170.

Furue, R. (2003), Energy transfer within the small-scale oceanic internal wave spectrum, *J. Phys. Oceanogr.*, *33*, 267–282.

Furuichi, N., T. Hibiya, and Y. Niwa (2005), Bispectral analysis of energy transfer within the two-dimensional oceanic internal wavefield, *J. Phys. Oceanogr.*, *35*, 2104–2109.

Gardiner, C. W. (2004), *Handbook of Stochastic Methods*, 415 pp., Springer, New York.

Garrett, C. J. R., and W. H. Munk (1972), Space-timescales of internal waves, *Geophys. Fluid. Dyn.*, *2*, 225–264.

Garrett, C. J. R., and W. H. Munk (1975), Space-timescales of internal waves. A progress report, *J. Geophys. Res.*, *80*, 291–297.

Gill, A. E. (1982), *Atmosphere-Ocean Dynamics*, Academic, San Diego, Calif.

Gregg, M. C. (1988), The dependence of turbulent dissipation on stratification in a diffusively stable thermocline, *J. Geophys. Res.*, *93*, 12,381–12,392.

Gregg, M. C. (1989), Scaling turbulent dissipation in the thermocline, *J. Geophys. Res.*, *94*, 9686–9698.

Gregg, M. C., D. P. Winkel, and T. B. Sanford (1993a), Varieties of fully resolved spectra of vertical shear, *J. Phys. Oceanogr.*, *23*, 124–141.

Gregg, M. C., H. E. Seim, and D. B. Percival (1993b), Statistics of shear and turbulent dissipation profiles in random internal wavefields, *J. Phys. Oceanogr.*, *23*, 1777–1799.

Gregg, M. C., T. B. Sanford, and D. P. Winkel (2003), Reduced mixing from the breaking of internal waves in equatorial waters, *Nature*, *422*, 513–515.

Hayes, S. P. (1975), Preliminary measurements of the time-lagged coherence of vertical temperature profiles, *J. Geophys. Res.*, *80*, 307–311.

Hendry, R. M. (1977), Observations of the semidiurnal internal tide in the western North Atlantic Ocean, *Philos. Trans. R. Soc. London, Ser. A*, *286*, 1–24.

Henyey, F. S., J. Wright, and S. M. Flatté (1986), Energy and action flow through the internal wave field: An eikonal approach, *J. Geophys. Res.*, *91*, 8487–8495.

Hibiya, T., M. Nagasawa, and Y. Niwa (2002), Nonlinear energy transfer within the oceanic internal wave spectrum at mid and high latitudes, *J. Geophys. Res.*, *107*(C11), 3207, doi:10.1029/2001JC001210.

Hogg, N. G. (1981), Topographic waves along 70W on the Continental Rise, *J. Mar. Res.*, *39*, 627–649.

Hogg, N. G., and D. E. Frye (2007), Performance of a new generation of acoustic current meters, *J. Phys. Oceanogr.*, *37*, 148–161.

Keffer, T. (1983), The baroclinic stability of the Atlantic North Equatorial Current, *J. Phys. Oceanogr.*, *13*, 624–631.

Kunze, E. (1985), Near-inertial wave propagation in geostrophic shear, *J. Phys. Oceanogr.*, *15*, 544–565.

Kunze, E., and T. B. Sanford (1993), Sub-mesoscale dynamics near a seamount. Part I: Measurements of Ertel vorticity, *J. Phys. Oceanogr.*, *23*, 2567–2588.

Kwon, Y.-O., and S. C. Riser (2004), North Atlantic Subtropical Mode Water: A history of ocean-atmosphere interaction 1961–2000, *Geophys. Res. Lett.*, *31*, L19307, doi:10.1029/2004GL021116.

Landau, L. D., and E. M. Lifshitz (1980), *Statistical Physics, Part* 1, *Course of Theor. Phys.*, vol. 5, 3rd ed., Butterworth-Heinemann, Oxford, U. K.

Leaman, K. D. (1976), Observations on the vertical polarization and energy flux of near-inertial waves, *J. Phys. Oceanogr.*, *6*, 894–908.

Leaman, K. D., and T. B. Sanford (1975), Vertical energy propagation of inertial waves: A vector spectral analysis of velocity profiles, *J. Geophys. Res.*, *80*, 1975–1978.

Ledwell, J. R., E. T. Montgomery, K. L. Polzin, L. C. St. Laurent, R. W. Schmitt, and J. M. Toole (2000), Evidence for enhanced mixing over rough topography in the abyssal ocean, *Nature*, *403*(6766), 179–182.

Levine, M. D. (1990), Internal waves under the Arctic ice pack during the Arctic Internal Wave Experiment: The coherence structure, *J. Geophys. Res.*, *95*, 7347–7357.

Levine, M. D., J. D. Irish, T. E. Ewart, and S. A. Reynolds (1986), Simultaneous spatial and temporal measurements of the internal wavefield during MATE, *J. Geophys. Res.*, *91*, 9709–9719.

Levine, M. D., C. A. Paulson, and J. H. Morrison (1987), Observations of internal gravity waves under the Arctic ice pack, *J. Geophys. Res.*, *92*, 779–782.

Levine, M. S. (2002), A modification of the Garrett-Munk internal wave spectrum, *J. Phys. Oceanogr.*, *32*, 3166–3181.

Lueck, R. G., and T. D. Mudge (1997), Topographically induced mixing around a shallow seamount, *Science*, *276*, 1831–1833.

Luyten, J. R., and H. M. Stommel (1991), Comparison of M_2 tidal currents observed by some deep moored current meters with those of the Schwiderski and Laplace tidal models, *Deep Sea Res.*, *38*, suppl. 1, S573–S589.

Lvov, Y. V., and S. Nazarenko (2004), Noisy spectra, long correlations, and intermittency in wave turbulence, *Phys. Rev. E*, *69*, 066608.

Lvov, Y. V., and E. G. Tabak (2001), Hamiltonian formalism and the Garrett and Munk spectrum of internal waves in the ocean, *Phys. Rev. Lett.*, *87*, 169501.

Lvov, Y. V., and E. G. Tabak (2004), A Hamiltonian formulation for long internal waves, *Physica D*, *195*, 106–122.

Lvov, V. S., Y. V. Lvov, A. C. Newell, and V. E. Zakharov (1997), Statistical description of acoustic turbulence, *Phys. Rev. E*, *56*, 390–405.

Lvov, Y. V., S. Nazarenko, and R. West (2003), Wave turbulence in Bose Einstein condensates, *Physica D*, *184*, 333–351.

Lvov, Y. V., K. L Polzin, and E. Tabak (2004), Energy spectra of the ocean's internal wave field: Theory and observations, *Phys. Rev. Lett.*, *92*, 128501.

Lvov, Y. V., K. L. Polzin, E. G. Tabak, and N. Yokoyama (2010), Oceanic internal wavefield: Theory of scale-invariant spectra, *J. Phys. Oceanogr.*, *40*, 2605–2623.

Lvov, Y. V., K. L. Polzin, and N. Yokoyama (2011), Resonant and near-resonant internal wave interactions, *J. Phys. Oceanogr.*, in press.

MacKinnon, J., and K. Winters (2005), Subtropical catastrophe: Significant loss of low-mode tidal energy at 28.9, *Geophys. Res. Lett.*, *32*, L15605, doi:10.1029/2005GL023376.

McComas, C. H. (1975), Nonlinear interaction of internal gravity waves, Ph.D. thesis, Johns Hopkins Univ., Baltimore, Md.

McComas, C. H. (1977), Equilibrium mechanisms within the oceanic internal wavefield, *J. Phys. Oceanogr.*, *7*, 836–845.

McComas, C. H., and F. P. Bretherton (1977), Resonant interaction of oceanic internal waves, *J. Geophys. Res.*, *83*, 1397–1412.

McComas, C. H., and P. Müller (1981a), Timescales of resonant interactions among oceanic internal waves, *J. Phys. Oceanogr.*, *11*, 139–147.

McComas, C. H., and P. Müller (1981b), The dynamic balance of internal waves, *J. Phys. Oceanogr.*, *11*, 970–986.

Millard, R. (1972), Further comments on vertical temperature spectra in the MODE region, *MODE Hot Line News*, *18*, 1.

Mode-I Atlas Group (1977), *Atlas of the Mid-Ocean Dynamics Experiment* (*MODE-I*), 274 pp., Mass. Inst. of Technol., Cambridge.

Molemaker, M. J., J. C. McWilliams, and I. Yavneh (2005), Baroclinic instability and loss of balance, *J. Phys. Oceanogr.*, *35*, 1505–1517.

Müller, P. (1976), On the diffusion of momentum and mass by internal gravity waves, *J. Fluid Mech.*, *77*, 789–823.

Müller, P. (1995), Ertel's potential vorticity theorem in physical oceanography, *Rev. Geophys.*, *33*, 67–97.

Müller, P., and D. J. Olbers (1975), On the dynamics of internal waves in the deep ocean, *J. Geophys. Res.*, *80*, 3848–3860.

Müller, P., and N. Xu (1992), Scattering of oceanic internal gravity waves off random bottom topography, *J. Phys. Oceanogr.*, *22*, 474–488.

Müller, P. G., D. J. Olbers, and J. Willebrand (1978), The IWEX spectrum, *J. Geophys. Res.*, *83*, 479–500.

Müller, P., G. Holloway, F. Henyey, and N. Pomphrey (1986), Nonlinear interactions among internal gravity waves, *Rev. Geophys.*, *24*, 493–536.

Munk, W. (1981), Internal waves and small-scale processes, in *Evolution of Physical Oceanography*, edited by B. A. Warren and C. Wunsch, pp. 264–291, MIT Press, Cambridge, Mass.

Natarov, A., and P. Müller (2005), A dissipation function for the internal wave radiative balance equation, *J. Atmos. Oceanic Technol.*, *22*, 1782–1796.

Niwa, Y., and T. Hibiya (2001), Numerical study of the spatial distribution of the M2 internal tide in the Pacific Ocean, *J. Geophys. Res.*, *106*, 22,441–22,449.

Noble, M. (1975), Observations of mid-ocean tides during IWEX, MS thesis, Mass. Inst. of Technol., Cambridge.

Nowlin, W. D., Jr., J. S. Bottero, and R. D. Pillsbury (1986), Observations of internal and near-inertial oscillations at Drake Passage, *J. Phys. Oceanogr.*, *16*, 87–108.

Olbers, D. J. (1973), On the energy balance of small-scale internal waves in the deep sea, *Hamburg Geophys. Einzelschr.*, *24*, 1–91.

Olbers, D. J. (1976), Nonlinear energy transfer and the energy balance of the internal wavefield in the deep ocean, *J. Fluid Mech.*, *74*, 375–399.

Olbers, D. J., and K. Herterich (1978), The spectral energy transfer from surface waves to internal waves, *J. Fluid Mech.*, *92*, 349–379.

Olbers, D. J., and N. Pomphrey (1981), Disqualifying two candidates for the energy balance of oceanic internal waves, *J. Phys. Oceanogr.*, *11*, 1423–1425.

Padman, L., and T. M. Dillon (1987), Thermal microstructure and internal waves in the Canada Basin diffusive staircase, *Deep Sea Res.*, *36*, 531–542.

Pelinovskii, E. N., and M. A. Raevsky (1977), Weak turbulence of internal ocean waves, *Izv. Akad. Nauk SSSR Fiz. Atmos. Okeana*, *13*, 187–193.

Phillips, O. M. (1960), On the dynamics of unsteady gravity waves of finite amplitude part I. The elementary interactions, *J. Fluid Mech.*, *9*, 193–217.

Pinkel, R. (2005), Near-inertial wave propagation in the western Arctic, *J. Phys. Oceanogr.*, *35*, 645–665.

Pinkel, R. (2008), Advection, phase distortion, and the frequency spectrum of finescale fields in the sea, *J. Phys. Oceanogr.*, *38*, 291–313.

Pitaevskii, L. P., and E. M. Lifshitz (1981), *Physical Kinetics, Course of Theor. Phys.*, vol. 10, Butterworth-Heinemann, Oxford, U. K.

Plueddemann, A. J., and J. T. Farrar (2006), Observations and models of the energy flux from the wind to mixed layer inertial currents, *Deep Sea Res.*, *53*, 5–30.

Pollard, R. T., and R. C. Millard (1970), Comparison between observed and simulated wind-generated inertial oscillations, *Deep Sea Res.*, *17*, 153–175.

Pollard, R. T., and L. A. Regier (1992), Vorticity and vertical circulation at an ocean front, *J. Phys. Oceanogr.*, *22*, 609–625.

Polton, J. A., J. A. Smith, J. A. MacKinnon, and A. E. Tejada-Martinez (2008), Rapid generation of high-frequency internal waves beneath a wind and wave forced oceanic surface mixed layer, *Geophys. Res. Lett.*, *35*, L13602, doi:10.1029/2008GL033856.

Polzin, K. L. (1996), Statistics of the Richardson number: Mixing models and finestructure, *J. Phys. Oceanogr.*, *26*, 1409–1425.

Polzin, K. L. (2004a), A heuristic description of internal wave dynamics, *J. Phys. Oceanogr.*, *34*(1), 214–230.

Polzin, K. L. (2004b), Idealized solutions for the energy balance of the finescale internal wavefield, *J. Phys. Oceanogr.*, *34*(1), 231–246.

Polzin, K. L. (2008), Mesoscale eddy–internal wave coupling. I. Symmetry, wave capture and results from the Mid-Ocean Dynamics Experiment, *J. Phys. Oceanogr.*, *38*, 2556–2574.

Polzin, K. L. (2010), Mesoscale eddy–internal wave coupling. II. Energetics and results from PolyMode, *J. Phys. Oceanogr.*, *40*, 789–801.

Polzin, K. L., and R. Ferrari (2004), Isopycnal dispersion in NATRE, *J. Phys. Oceanogr.*, *34*(1), 247–257.

Polzin, K. L., J. M. Toole, and R. W. Schmitt (1995), Finescale parameterizations of turbulent dissipation, *J. Phys. Oceanogr.*, *25*, 306–328.

Polzin, K. L., N. S. Oakey, J. M. Toole, and R. W. Schmitt (1996), Finestructure and microstructure characteristics across the northwest Atlantic Subtropical Front, *J. Geophys. Res.*, *101*, 14,111–14,121.

Polzin, K. L., J. M. Toole, J. R. Ledwell, and R. W. Schmitt (1997), Spatial variability of turbulent mixing in the abyssal ocean, *Science*, *276*, 93–96.

Polzin, K. L., E. Kunze, J. Hummon, and E. Firing (2002), The finescale response of lowered ADCP velocity profiles, *J. Oceanic Atmos. Technol.*, *19*, 205–224.

Polzin, K. L., E. Kunze, J. M. Toole, and R. W. Schmitt (2003), The partition of fine-scale energy into internal waves and subinertial motions, *J. Phys. Oceanogr.*, *33*, 234–248.

Pomphrey, N., J. D. Meiss, and K. M. Watson (1980), Description of nonlinear internal wave interactions using Langevin methods, *J. Geophys. Res.*, *85*, 1085–1094.

Riley, J. J., and M.-P. Lelong (2000), Fluid motions in the presence of strong stable stratification, *Annu. Rev. Fluid Mech.*, *32*, 613–658.

Rossby, T. (1988), Five drifters in a Mediterranean salt lens, *Deep Sea Res.*, *35*, 1653–1663.

Ruddick, B. R. (1980), Critical layers and the Garrett-Munk spectrum, *J. Mar. Res.*, *38*, 135–145.

Ruddick, B. R., and T. M. Joyce (1979), Observations of interaction between the internal wavefield and low-frequency flows in the North Atlantic, *J. Phys. Oceanogr.*, *9*, 498–516.

Rudnick, D. L., et al. (2003), From tides to mixing along the Hawaiian Ridge, *Science*, *301*, 355–357.

Sanford, T. B. (1975), Observations of the vertical structure of internal waves, *J. Geophys. Res.*, *80*, 3861–3871.

Sanford, T. B., E. A. D'Asaro, E. Kunze, J. H. Dunlap, R. G. Drever, M. A. Kennelly, M. D. Prater, and M. S. Horgan (1993), An XCP user's guide and reference manual, *Tech. Rep., APL-UW TR 9309*, 101 pp., Appl. Phys. Lab., Univ. of Wash., Seattle.

Schmit, R. W., J. M. Toole, R. L. Koehler, E. C. Mellinger, and K. W. Doherty (1988), The development of a fine- and microstructure profiler, *J. Atmos. Oceanic Technol.*, *5*, 484–500.

Schmitt, R. W., J. R. Ledwell, E. T. Montgomery, K. L. Polzin, and J. M. Toole (2005), Enhanced diapycnal mixing by salt fingers in the thermocline of the tropical Atlantic, *Science*, *308*, 685–688.

Sherman, J. T., and R. Pinkel (1991), Estimates of the vertical wavenumber-frequency spectra of vertical shear and strain, *J. Phys. Oceanogr.*, *21*, 292–303.

Siedler, G., and U. Paul (1991), Barotropic and baroclinic tidal currents in the western basins of the North Atlantic, *J. Geophys. Res.*, *96*, 22,259–22,271.

Silverthorne, K. E., and J. M. Toole (2009), Seasonal kinetic energy variability of near-inertial motions, *J. Phys. Oceanogr.*, *39*, 1035–1049.

Simmons, H. L. (2008), Spectral modification and geographic redistribution of the semi-diurnal internal tide, *Ocean Modell.*, *21*, 126–138.

Simmons, H. L., R. W. Hallberg, and B. K. Arbic (2004), Internal wave generation in a global baroclinic tidal model, *Deep Sea Res.*, *51*, 3043–3068.

Skyllingstad, E. D., and D. W. Denbo (1994), The role of internal gravity waves in the equatorial current system, *J. Phys. Oceanogr.*, *24*, 2093–2110.

Skyllingstad, E. D., W. D. Smyth, and G. B. Crawford (2000), Resonant wind-driven mixing in the ocean boundary layer, *J. Phys. Oceanogr.*, *30*, 1866–1890.

St. Laurent, L., and C. Garrett (2002), The role of internal tides in mixing the deep ocean, *J. Phys. Oceanogr.*, *32*, 2882–2899.

Trask, R. P., M. G. Briscoe, and N. J. Pennington (1982), Long term upper ocean study (LOTUS). A summary of the historical and engineering test data, *Tech. Rep., WHOI-82-53*, 108 pp., Woods Hole Oceanogr. Inst., Woods Hole, Mass.

Voronovich, A. G. (1979), Hamiltonian formalism for internal waves in the ocean, *Izv. Atmos. Oceanic Phys.*, *16*, 52–57.

Watanabe, M., and T. Hibiya (2002), Global estimates of the wind-induced energy flux to inertial motions in the surface mixed layer, *Geophys. Res. Lett.*, *29*(8), 1239, doi:10.1029/2001GL014422.

Watson, K. M. (1990), The coupling of surface and internal gravity waves: Revisited, *J. Phys. Oceanogr.*, *20*, 1233–1248.

Watson, K. M. (1994), Energy transfer between surface and internal gravity waves in the North Pacific, *J. Geophys. Res.*, *99*, 12,549–12,560.

Watson, K. M., B. J. West, and B. I. Cohen (1976), Coupling of surface and internal gravity waves: A mode coupling model, *J. Fluid Mech.*, *77*, 185–208.

Webster, F. (1969), Turbulence spectra in the ocean, *Deep Sea Res.*, *16*, suppl., 357–368.

Weller, R. A. (1991), Overview of the Frontal Air-Sea Interaction Experiment (FASINEX): A study of air-sea interaction in a region of strong oceanic gradients, *J. Geophys. Res.*, *96*, 8501–8516.

Weller, R. A., and R. E. Davis (1980), A vector measuring current meter, *Deep Sea Res.*, *27*, 565–581.

Weller, R. A., D. L. Rudnick, C. C. Eriksen, K. L. Polzin, N. S. Oakey, J. M. Toole, R. W. Schmitt, and R. T. Pollard (1991a), Forced ocean response during the Frontal Air-Sea Interaction Experiment, *J. Geophys. Res.*, *96*, 8611–8693.

Weller, R. A., M. A. Donelan, M. G. Briscoe, and N. E. Huang (1991b), Riding the crest: A tale of two wave experiments, *Bull. Am. Meteorol. Soc.*, *72*, 163–183.

Weller, R. A., P. W. Furey, M. A. Spall, and R. E. Davis (2004), The large-scale context for oceanic subduction in the northeast Atlantic, *Deep Sea Res. I*, *51*, 665–699.

Wijesekera, H. W., and T. M. Dillon (1991), Internal waves and mixing in the upper equatorial Pacific Ocean, *J. Geophys. Res.*, *96*, 7115–7125.

Winkel, D. P., M. C. Gregg, and T. B. Sanford (1996), Resolving oceanic shear and velocity with the multi-scale profiler, *J. Atmos. Oceanic Technol.*, *13*, 1046–1072.

Winters, K. B., and E. A. D'Asaro (1997), Direct simulation of internal wave energy transfer, *J. Phys. Oceanogr.*, *27*, 1937–1945.

Witham, G. B. (1974), *Linear and Nonlinear Waves*, 636 pp., Wiley-Interscience, New York.

Wunsch, C. (1975), Internal tides in the ocean, *Rev. Geophys.*, *13*, 167–182.

Wunsch, C. (1997), The vertical partition of oceanic horizontal kinetic energy, *J. Phys. Oceanogr.*, *27*, 1770–1794.

Wunsch, C., and R. Ferrari (2004), Vertical mixing, energy, and the general circulation of the oceans, *Annu. Rev. Fluid Mech.*, *36*, 281–314.

Wunsch, C., and S. Webb (1979), The climatology of deep ocean internal waves, *J. Phys. Oceanogr.*, *9*, 235–243.

Zakharov, V. E., V. S. Lvov, and G. Falkovich (1992), *Kolmogorov Spectra of Turbulence*, Springer, Berlin.

Y. V. Lvov, Department of Mathematical Sciences, Rensselaer Polytechnic Institute, Troy, NY 12180, USA. (lvovy@rpi.edu)

K. L. Polzin, Woods Hole Oceanographic Institution, MS#21, Woods Hole, MA 02543, USA. (kpolzin@whoi.edu)